Forschungszentrum Karlsruhe
Technik und Umwelt

Wissenschaftliche Berichte
FZKA 5991

Investigations on Physics and Dynamics of Matter with the Karlsruhe Light Ion Facility KALIF

B. Goel, K. Baumung, W. Höbel, G. I. Kanel, H. Marten, V. B. Mintsev, S. V. Razorenov, D. Rusch, A. V. Shutov, J. Singer, A. V. Utkin, O. Yu. Vorobiev

Institut für Neutronenphysik und Reaktortechnik

März 1998

Forschungszentrum Karlsruhe

Technik und Umwelt

Wissenschaftliche Berichte

FZKA 5991

Investigations on physics and dynamics of matter with the Karlsruhe Light Ion Facility KALIF

B. Goel, K. Baumung, W. Höbel, G.I. Kanel*, H. Marten, V.B. Mintsev*, S.V. Razorenov*, D. Rusch, A.V. Shutov*, J. Singer, A.V. Utkin*, O.Yu. Vorobiev*

Institut für Neutronenphysik und Reaktortechnik

*Institute of Chemical Physics, Laboratory of Physical Gasdynamics
Chernogolovka, Russia

Forschungszentrum Karlsruhe GmbH, Karlsruhe
1998

Als Manuskript gedruckt

Forschungszentrum Karlsruhe GmbH
Postfach 3640, 76021 Karlsruhe

Mitglied der Hermann von Helmholtz-Gemeinschaft
Deutscher Forschungszentren (HGF)

ISSN 0947-8620

Investigations on physics and dynamics of matter with the Karlsruhe Light Ion Facility KALIF

Abstract

In this report we present investigation on the dense plasma performed in the last few years at our Light Ion Facility KALIF. Equation of state of matter in the region of strongly coupled plasma is investigated. The zone directly heated by the KALIF beam gets about 5 MJ/g of energy within first few 10's of ns. This launches a strong shock wave in the adjacent cold material. By suitably designing the target thin foils could be accelerated to velocities > 12 km/s. The acceleration of flyer plate is not monotonic and shows several steps caused by shock wave reverberation within the flyer. Detailed analysis of this process gives clues about the equation of state of the matter. We have developed a Mie-Grüneisen type of equation of state that describe states of matter better than the previously available equation of states. Precise measurement of shock melting for a few materials is also presented. Further, spall strengths for some single- and polycrystalline materials have been measured at high strain rates in excess of $10^6 s^{-1}$. Spall strength of single crystals exceed that of polycrystalline material by a factor of 2 to 3.

Untersuchungen zur Physik und zum dynamischen Verhalten von Materie an der Karlsruhe Light Ion Facility KALIF

Zusammenfassung:

Der vorliegende Bericht gibt einen Überblick über experimentelle Untersuchungen an dichten Plasmen, die an der KALIF-Anlage durchgeführt werden, sowie über die begleitenden theoretischen Analysen. Schwerpunkt der Arbeiten ist die thermodynamische Zustandsgleichung der Materie im Bereich der stark gekoppelten Plasmen. In kondensierter Materie wird durch den KALIF-Ionenstrahl innerhalb weniger 10 Nanosekunden eine spezifische Energie von etwa 5 MJ/g deponiert. Dadurch wird im angrenzenden kalten Material eine Stoßwelle erzeugt. Dünne Targets werden durch Stoßwellen und Verdünnungswellen, die zwischen der unter Druck stehenden Energiedepositionszone und der drucklosen Rückseite hin- und herlaufen stufenweise auf Geschwindigkeiten bis >12 km/s beschleunigt. Anhand der detaillierten Analyse dieses Prozesses konnten verfügbare Zustands-gleichungen mittels eines Mie-Grüneisen-Ansatzes deutlich verbessert werden. Außerdem werden Ergebnisse von Messungen des Stoßwellendrucks, der bei Druckentlastung zum Aufschmelzen des Materials führt, sowie der dynamischen Zugfestigkeit von metallischen Einkristallen bzw. polykristallinen Proben vorgestellt.

Contents

1. Introduction

Pulsed high-power ion beams are subject of research and development in a number of laboratories all over the world. The driving motivation for this work is the potential application in inertial confinement fusion (ICF). High beam energies that can be provided at low cost and good efficiency and the effective energy deposition in the target are considered to be the main advantage of this technique. A total beam power of >100 TW and a total energy of 5-10 MJ is considered necessary to ignite an ICF-pellet and to achieve a reasonable energy gain. The performance of the devices operated today is by one to two orders of magnitude lower. However, with specific power densities of 10-1000 TW/g and total energy depositions of several MJ/g these facilities open new possibilities for matter research at high energy densities.

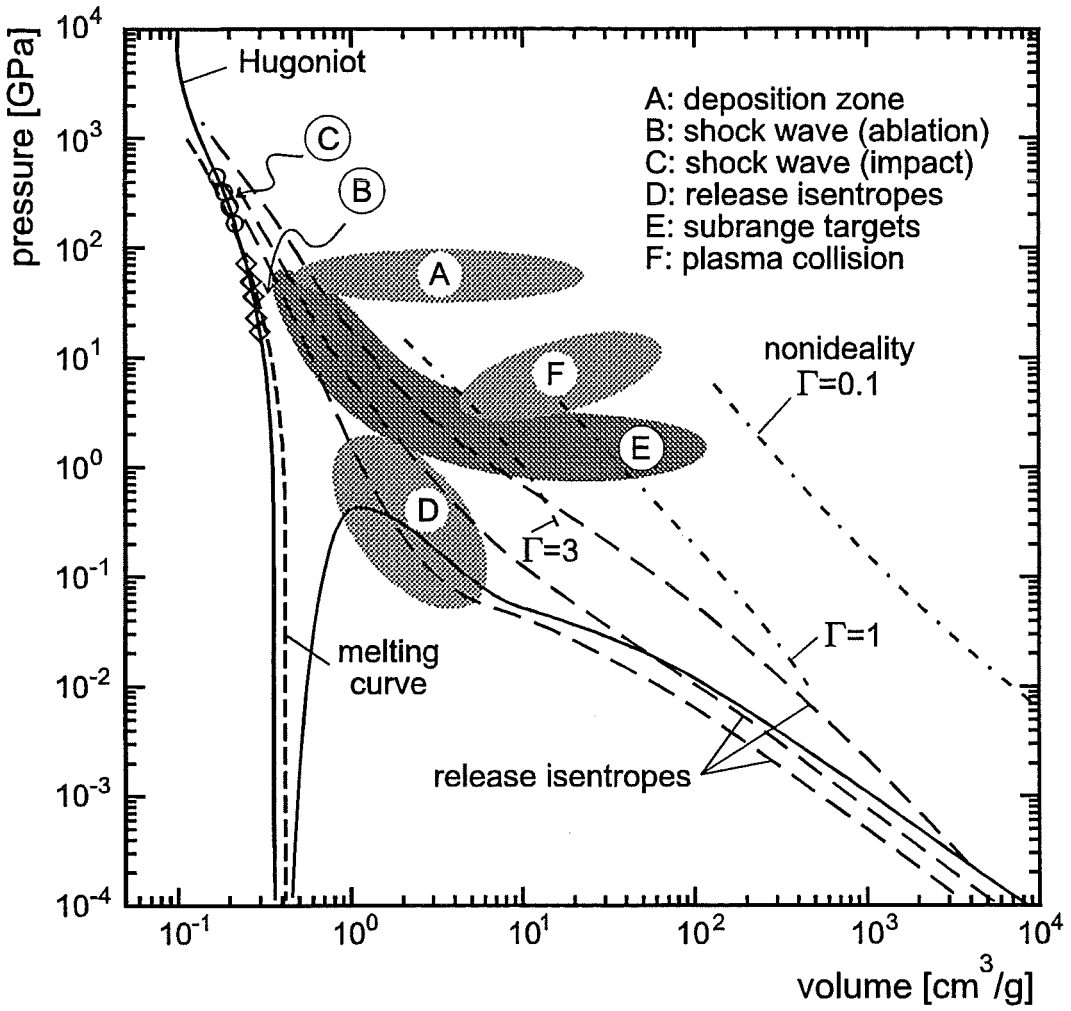

Fig.1.1. The phase diagram for aluminum.

Shock waves can be generated by ion beams in two ways. The massive energy deposition in a zone of 5-10 mg/cm^2 leads to fast vaporization and ablation of the material and causes intense (>100 GPa) compression waves to propagate into the residual part of the target. In this way thin condensed targets with thicknesses of several tens of micrometers can be accelerated to velocities much larger than 10 km/s. Impacting these flyers on stationary solid targets generates shock waves of about 10 ns duration and pressures up to several 100 GPa. The states of matter that can be produced in aluminum by the high-power proton beam of the Karlsruhe Light Ion Facility "KALIF" are depicted in figure 1.1. Experimental data obtained in traditional explosion experiments are concentrated mainly along the Hugoniot curve (C & B). Region A corresponds to matter states produced in the energy deposition zone of a thick target. A state near the critical point (D) is produced adjacent to the boundary of the energy deposition zone during the unloading of these highly compressed states later in the process. Region E corresponds to plasma states obtained with subrange foils heated by a beam with 0.1 TW/cm^2. The collision of such a plasma with a hard wall will produce a hotter plasma (region F). The dashed curves present plasma states with different degrees of nonideality calculated by a model of ionization equilibrium for dense plasma (Ebeling *et al.* 1991). Release isentropes for the shock pressure of 6, 10 and 20 Mbar are also shown in this figure. Most of the plasma that is generated by the action of the ion beam is in the region of moderate to strong nonideality.

During the ion beam deposition high pressure builds up and propagates into the residual part of the target. As the particle energy rises the ion range increases from 10 to 30 µm depending on the target material. In KALIF-experiments proton flux starts at about 0.8 MeV (the range of 0.8 MeV protons in cold aluminum is ~ 10 µm) the peak proton energy is 1.5 MeV (this corresponds to a range of 25 µm in cold aluminum). The duration of the ion beam of larger than 40 ns is considerably greater than the sound reverberation period of a few nanoseconds in the energy deposition zone so that the energy deposition is not instantaneous. During the late phase of the pulse, the energy deposition zone decouples hydrodynamically from the residual condensed part of the target, at first due to range shortening effects (Goel & Bluhm 1988), later eventually due to the decrease of the accelerating voltage i.e. due to lower proton energy. As a consequence, pressure, density, and temperature show strong spatial and temporal variation in both the energy deposition zone and the residual condensed part of the target. Therefore, the selection of shock wave physics tasks that can be solved practically by employing ion beams requires, first of all, the detailed understanding of the beam-target interaction. This is a complex problem and needs, besides experimental investigation, elaborate theoretical considerations and strong support by computer simulations. We have used shock wave physics methods to investigate the beam target interaction process and to determine the beam parameters like power density and ion range. On this basis, we are able to identify the most efficient application of the specific capabilities of the method, and to determine the appropriate experimental approach.

The specific characteristics of the state of matter generated by high-power ion beams is its high pressure and temperature as well as high gradients in pressure, temperature, and density. Therefore, priority issues that should be addressed are problems in physics of strongly coupled plasmas, heat transfer and EOS of matter in the domain where empirical data is scarce. In addition, hypervelocity launching of

flyer plates and impact opens a way to study the equation of state (EOS) in the 100 - 1000 GPa pressure range, melting, vaporization and optical properties of material at high pressures and temperatures, and to simulate impacts of micrometeorites. As compared with load durations in the range of 0.1 - 10 μs, and steady conditions over distances of several millimeters in conventional shock-wave experiments, nanosecond pressure pulses as generated in ion beam experiments decay over comparatively short distances. The question whether equilibrium establishes in the shock-compressed state on this time scale has to be scrutinized in each particular case. The small load duration, that makes some of the measurements difficult, can be advantageous for the investigation of a measuring technique of time-dependent processes such as rate-dependent inelastic deformations and fracture, kinetics of phase and polymorphic transformations, and chemical reactions. The small dimensions of the test area, erratic nature of pulse power, and the complex dynamics pose some challenges to the experimental technique and require:

- the measurement to provide high time and space resolution,
- as many parameters of state as possible to be measured simultaneously in order to provide a maximum of information per single test,
- experiments to be assisted by extensive computer simulation of the phenomena under investigation.

The objective of this report is to present the results obtained so far and to discuss future possibilities of ion beam driven high energy density and shock wave physics experiments.

2. The experimental facility, set-up, and measurements

Experiments are performed at the Karlsruhe Light Ion Facility (KALIF). This is a pulse power generator that can couple several 10's of kJ of electrical energy to diodes. Basically two types, B_Θ-diodes and applied-B diodes are used to produce intense proton beams with focused ion power density of 0.15 and 1 TW/cm^2, respectively.

2.1. The proton beam generator

A vertical section of KALIF is depicted in figure 2.1. KALIF is a water-dielectric 2.25 Ω coaxial-line pulse power generator that delivers a 50 ns fwhm pulse of 1.7 MV peak voltage and 600 kA peak current into a matched load. The potential of several extractor-type ion sources, the so-called "diodes", to produce intense proton beams has been investigated in detail. Actually, two different types of diodes are operated regularly on KALIF. The basic requirements for the efficient conversion of electrical energy into beam energy are:

- magnetic insulation of the diode to avoid a predominant contribution of electrons to the total diode current, and
- an anode plasma source providing the required ion species with high purity and homogeneity over a suitable surface at the current density needed, in a well-defined geometry, and at the right time with regard to the generator pulse.

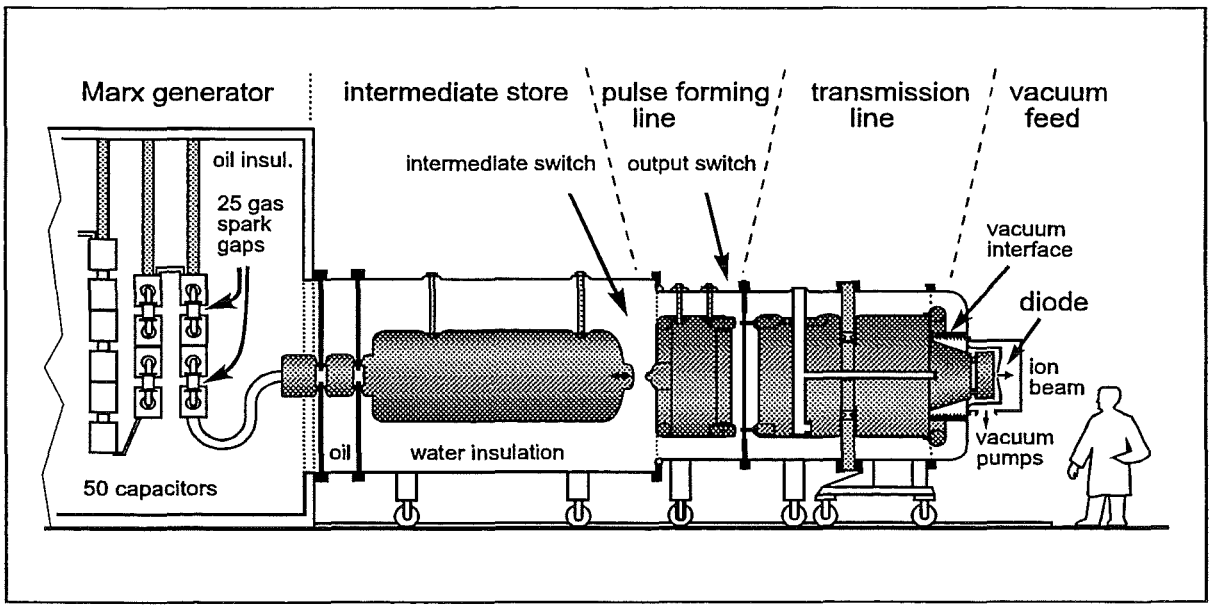

Figure 2.1: Vertical section of the Karlsruhe Light Ion Facility KALIF

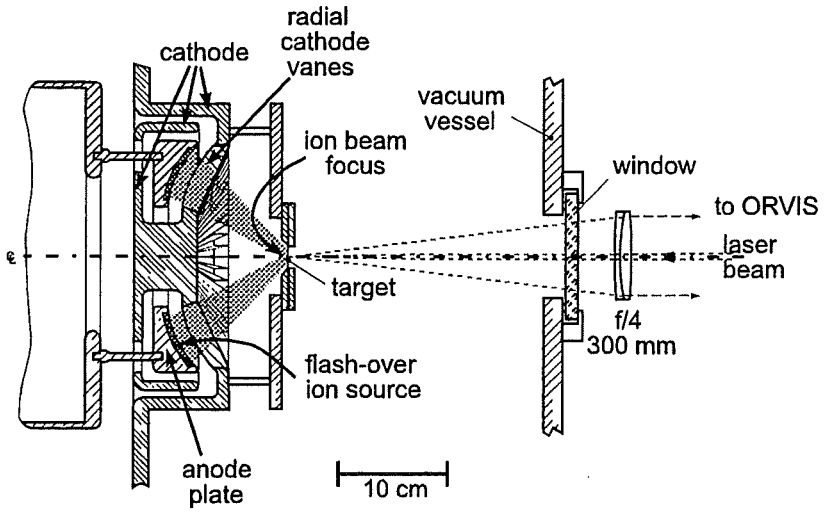

Figure 2.2: Close-up view of the B_Θ-diode and the target.

For most of the experiments reported here, the self-magnetically insulated so-called "B_Θ-diode" (fig. 2.2) was used (Schimassek *et al.* 1991). In this diode, a flash-over across an annular PMMA inlay in the anode plate generates the plasma from which essentially protons are extracted. Electrons emitted from the radial cathode vanes are much more mobile than ions and must be prevented from directly crossing and shortening the anode-cathode gap. This is achieved by "self-magnetical insulation": the diode current induces an azimuthal (B_Θ) magnetic field that makes electrons drift radially and, close to the anode surface, surround the inner anode edge, and impinge on the anode at the rear side mainly. This extension of the electron trajectory increases the fraction of the proton current. The shape of the electrical field given by the geometry is designed to bring the protons on trajectories on which they will drift in the field-free space outside the cathode front to a focal spot on the axis at a distance of ~15 cm from the anode. Since ion currents exceeding 100 kA are involved strong self-induced magnetic and electrical forces must be neutralized in order to ensure proper focusing. This is achieved by current and space-charge neutralization of the beam which is provided by electrons picked up by the ions while passing between the cathode vanes. This process takes place in vacuum which facilitates experimenting with this diode and makes it a repetitive type of diode. About 10 shots can be performed without replacing any diode hardware. The peak power density in the 8 - 10 mm fwhm diameter focal spot is 0.15±0.05 TW/cm^2. The rise time of the voltage of about 20 ns and the distance to the target are such that ions starting later in the pulse at a higher acceleration voltage can overtake ions which started earlier at lower energies. As a result of this time-of-flight compression or bunching of the ion pulse the power density at the beginning of the interaction is high and even may exceed the power density at peak voltage. With proton ranges in condensed matter of 10 to 20 µm energy densities in the range of 1 MJ/g at specific power densities of 10 to 20 TW/g can be achieved with the B_Θ-diode.

Considerable progress in ion beam production and focusing has been made in the past few years with the so-called "applied B" (appl-B) diode (Bluhm *et al.* 1992a, 1992b, 1994). In this diode the insulating radial magnetic field is produced by two externally powered coils. The magnetic field strength amounts to ~3 T close to the anode and prevents electrons from reaching the anode for voltages up to three times the KALIF peak voltage. Electrons emitted from the cathode edge facing the anode drift perpendicular to *E* and *B* in azimuthal direction. At the same time they oscillate

radially. Due to instabilities of the initially thin electron layer, electrons rapidly fill the diode accelerating gap, and enhance the ion current. The position of zero electric field within the electron cloud is called the virtual cathode. Ion acceleration takes place between the anode plasma surface and this virtual cathode.
A pure hydrogen anode plasma is formed by a fast current pulse applied in radial direction across a 0.07-µm-thick, hydrogen-loaded Ti-Pd double-layer which is deposited on an insulating substrate on the anode surface (Laqua *et al.*1995). Within a few nanoseconds, the metal-hydride film is resistively heated beyond the melting temperature and starts desorbing hydrogen. The temperature rise results in an increasing resistance and therefore in an increasing voltage drop across the film which finally leads to a sliding discharge in the hydrogen, completely switching the current from the metal film to the plasma. The discharge occurs very homogeneously and provides a total proton density of ~5×10^{16} cm^{-2} this is sufficient to supply current densities of several kA/cm^2 during the 50 ns KALIF pulse. The Ti-Pd-film has to be replaced after each shot. Current and space charge neutralization are achieved by causing the beam to propagate through a low-pressure (several hPa) gas atmosphere that is separated from the vacuum in the anode-cathode gap by a 1.5-µm-thick mylar foil. The plasma generated in this drift space provides free electrons which travel together with the protons to the focus and provide the neutralization. The maximum power density in the ~6 mm fwhm focal spot is 1.05 TW/cm^2. The total beam energy amounts to ~40 kJ, representing 20% of the primary energy stored in the Marx capacitors. However, since this diode is still under development it could be used only for a few target experiments.

2.2. Recording method

Beam-target interaction experiments performed at KALIF in the past investigated the enhancement of the ion stopping power in ionized matter (Goel & Bluhm 1988), filamentation of the ion beam in the focus (Karow *et al.* 1990), and the peak ablation pressure (Bachmann *et al.* 1988). For the shock wave experiments, an ORVIS-type Laser-Doppler-Velocimeter (Bloomquist & Sheffield 1983) was set up enabling us to measure the velocity of the rear surface of thin (10 µm - 1 mm) targets with a 200 ps temporal resolution. It employs a 1 W single frequency argon ion laser and permits the velocity-per-fringe constant to be varied in multiple steps between 180 m/s and ~11 km/s. An important aspect of the experimental arrangement is the possibility to exactly synchronize the velocimeter record with the KALIF pulse. The trigger signal for the streak camera picked up from the pulse line shows a jitter relative to the ion beam impact on target of < ±7 ns and allows to fully utilize the high time resolution. The uncertainty of the velocity measurements does not exceed a few percent.

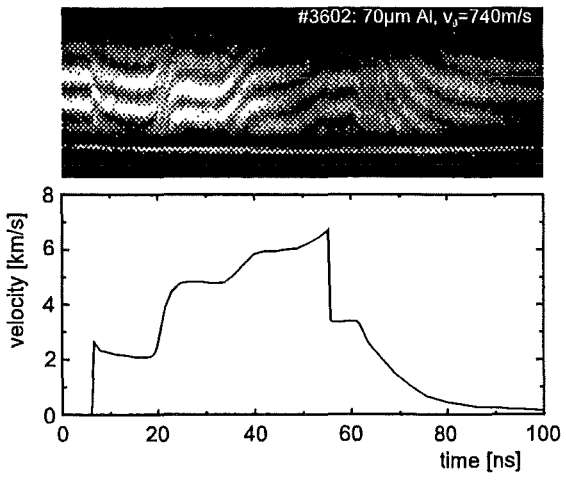

Figure 2.3: Ablative acceleration of a 70µm thick aluminum foil and impact on a LiF window. ORVIS interferogram and evaluated velocity profile

Figure 2.3 shows an example of an interferogram recorded with the ORVIS and the corresponding velocity history. In this shot, an initially 70 µm thick aluminum foil was ablatively launched and then impacted on a transparent LiF barrier. The interferogram is easily interpreted since the shift of the interference fringes is linearly proportional to the velocity increment. The acceleration of the flyer is not monotonic and shows several clearly visible steps caused by wave reverberations inside the foil between its rear surface and the boundary to the ablation plasma. The first jump followed by a short spike is due to the compression wave created by fast heating of the matter in the energy deposition zone. Its shape is determined by the energy and power distributions in the beam front. The sharp velocity decrease at 55 ns results from the impact of the foil on the barrier. After that, a small velocity plateau is recorded whose duration is determined by the reverberation time of the shock wave inside the foil. The following slow velocity decrease corresponds to the deceleration of the matter, i.e. the condensed part and the ablation plasma plume, behind the foil. Thus, even the velocity history of this single shot contains information about many aspects of the beam-target interaction: the structure of the bunched beam front, the residual (not ablated) foil thickness which determines the wave reverberation time, the parameters of the shock wave generated by the collision of the foil with the barrier, and some information about state of the material plume at the beam side of the foil. In the following, all these aspects are analyzed in more detail.

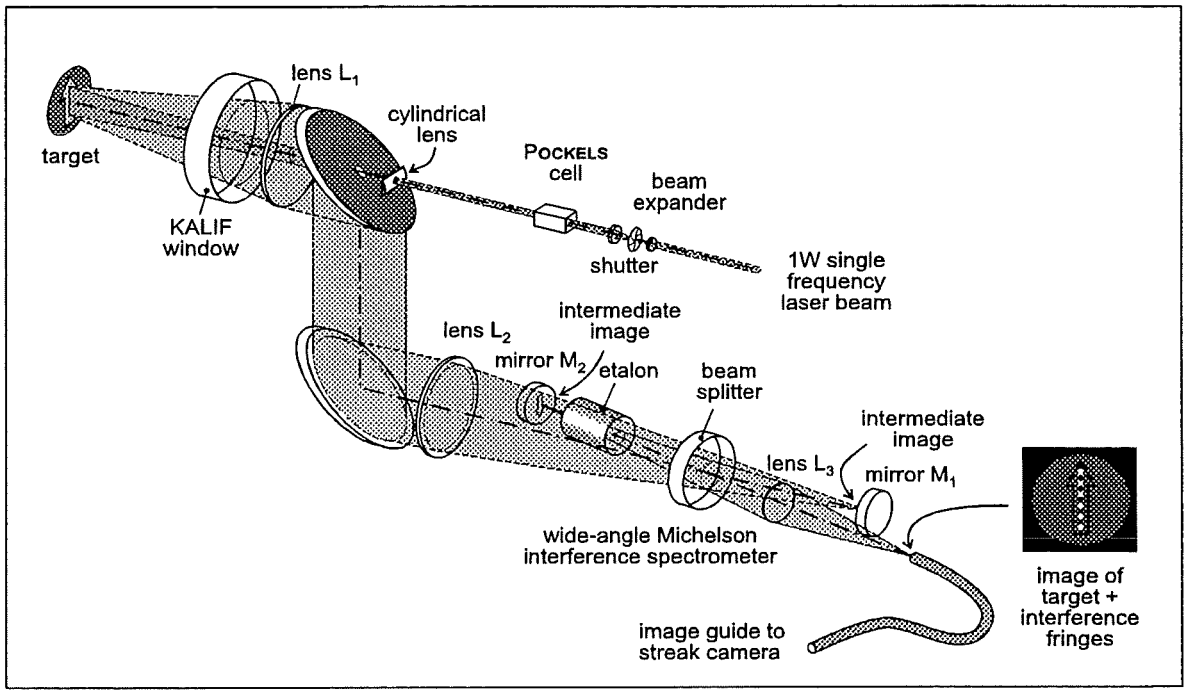

Figure 2.4: The improved high-resolution line-imaging laser Doppler velocimeter

For many applications, it seemed desirable to extend the velocimeter to 1-dim spatial resolution. The line-imaging VISAR described by Hemsing (1990) uses a slow collecting lens to directly image the target across the interferometer onto the slit of the streak camera. The big *f*-number provides a large depth of field but collects a very small part of the reflected light only. In addition, changing the imaging scale in practice strongly affects the effective *f*-number. Figure 2.4 shows our version of a high-resolution line-imaging laser-Doppler velocimeter (Baumung *et al.* 1995). Taking into account that the interference fringes in a Michelson interferometer are

localized in mirror planes M_1 and M_2, respectively, we make an intermediate imaging into these planes. For a maximum field of view of ~8 mm, the intermediate image is generated with lenses L_1 and L_2. For fields of view of 1-2 mm, L_1 alone is used. A fast projection lens L_3 is used to project the intermediate image on the input of an 4.5-m-long image guide. For optimum overall resolution, i.e. taking into account the limited performance of the streak camera, high magnification is needed. In this case, a telescope instead of L_3 is used. In this configuration, a spatial resolution of <10 µm with a total field of view of ~200 µm has been realized. A cylindrical lens is used to expand the laser beam vertically which then is focused by L_1 to illuminate a ≤10-mm-long and ~200-µm-wide line on the target.

With the first spatially resolving experiments we investigated the ablative acceleration of thin aluminum foils. Figure 2.5a depicts the interferogram obtained with a 50-µm-thick target in the VISAR (Barker & Hollenbach 1972) mode: the fringes indicate curves of equal velocity, the fringe constant being 608 m/s. Figure 2.5b shows the evaluated velocity profile for a 50 ns period. Since the ablation pressure p scales with power density I as $p \sim I^{0.7}$(Goel1990), the velocity across the 8 mm fwhm of the focus varies much less than a factor of two. However, it leads to an increasing curvature of the foil such that light reflected from off-axis regions gets progressively vignetted. This explains the early loss of intensity in off-axis positions. From figure 2.5a also follows that the position of peak intensity is slightly shifting during the pulse.

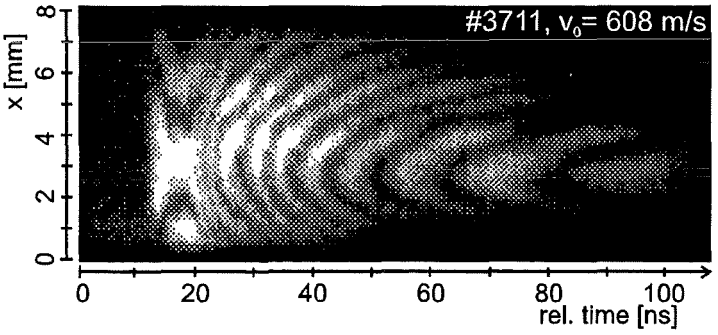

Figure 2.5a:
Line-imaging VISAR interferogram of the ablative acceleration of a 50µm thick Al foil. The bright fringes are curves of equal velocity, the velocity increment between two successive fringes being 608 m/s

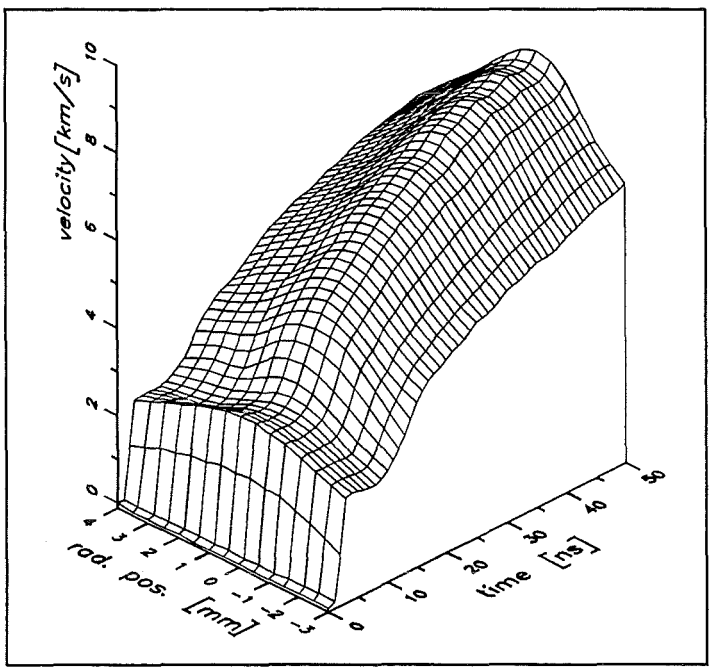

Figure 2.5b:
Ablative acceleration of a 50µm thick Al foil as a function of the radial distance from the beam axis vs. time. Evaluation of the raw data shown in fig. 6a for a 50 ns period.

2.3. Foil acceleration experiments

2.3.1. Hydrodynamics of the ion beam interaction with solid targets

Figure 2.6 shows the ablation pressure histories in aluminum targets deduced from particle velocity measurements performed with 33-µm-thick foils backed by LiF windows. Pressures were recalculated from the measured mass velocity history using the Hugoniot of LiF. Due to coincidence of the dynamic impedances of aluminum and LiF, the velocity profiles are practically not distorted by the wave reverberation inside the aluminum. Measurements have been done with both the B_Θ-diode and appl-B diode. The energy deposition of the steep bunched beam front of the B_Θ-diode causes the pressure to rise rapidly up to 25 GPa. After that, since the energy deposition rate continues to rise, the ablation pressure is approximately maintained during the rise time of the power pulse. After ~25 ns the power increase stops, and the expansion of the ablation plasma begins to outweigh the further energy input. As a result, the pressure starts falling. The appl-B diode needs some more time to establish nominal operating conditions. During this period, the ion current and, correspondingly, the beam power are relatively low. This is the reason for the "preshock" in the ablation pressure profile.

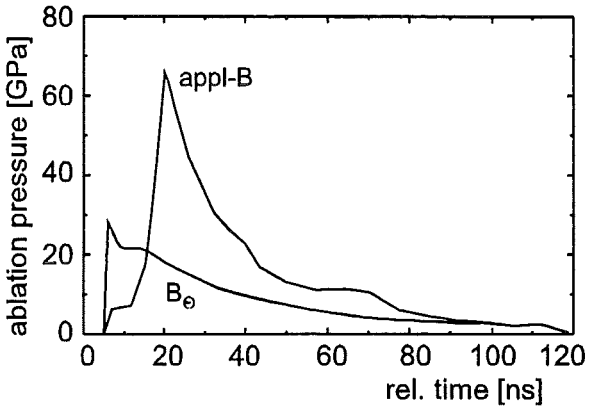

Figure 2.6: Ablation pressure generated in aluminum by the 0.15 TW/cm^2 B_Θ-diode and the 1 TW/cm^2 appl-B diode

Figure 2.7 shows the early phase of the free-surface velocity histories of three aluminum foils with 22, 33, and 50 µm initial thickness. There is a fast velocity increase to ~2 km/s with all three targets followed by a period of approximately constant velocity. Then, a second, less steep velocity rise appears. Finally, the slope of the curves becomes smooth. Figure 2.9 shows the first jump for two different experiments, both using 33-µm-thick aluminum foils, at a higher temporal resolution. To understand the different rise times of the first jump and the stepwise increase of the velocity, an analytical theory based on an acoustic approximation has been developed (Baumung *et al.* 1994). A discussion of figures 2.8 and 2.9 illuminates the main aspects of this theory. In figure 2.8, the processes during the first 5 to 10 ns in the flyer are shown in a *h,t*-diagram together with characteristic rear-free-surface velocity profiles. The B_Θ-diode needs some time for turn-on of the anode plasma and for reaching the electric working point. As a consequence, there is only little ion current as long as the diode voltage

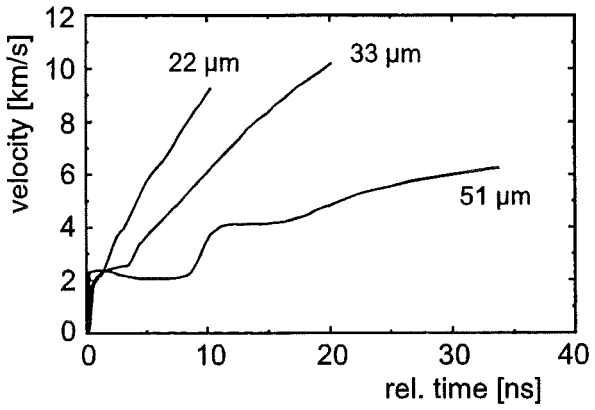

Figure 2.7: Measured velocity profiles of Al foils of different thickness

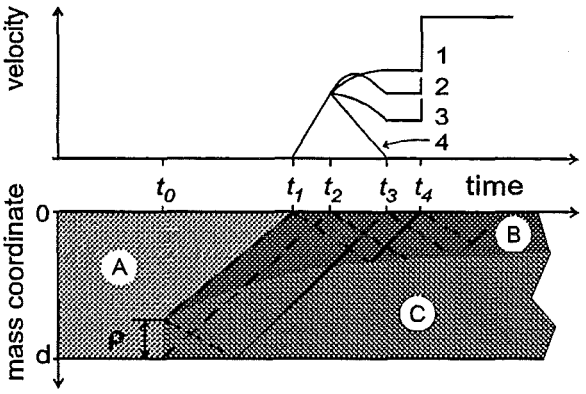

Figure 2.8: *h,t*-diagram of the initial phase of the beam-target interaction. The hydrodynamic response of the rear target surface (upper diagram) results from the reverberation of compression (solid lines) and release (dashed) waves between the energy deposition zone C and the free surface (A: unperturbed material, B: compressed material).

does not exceed about 500 kV. In normal KALIF shots voltage rise time is ~20 ns. In this case ions starting later with energies of 1 MeV or higher, catch up with ions which started a few nanoseconds earlier at lower energies of 500 keV on their 15 cm trajectory to the focus. This phenomenon of time-of-flight compression is called "bunching" in particle accelerators. Depending on the respective voltage pulse shape, which can vary considerably even in consecutive shots, the ion beam front on target may just show a steeper slope, or it may consist of a bunch in which ions with energies between 0.5 or less and 1 MeV reach the focus nearly simultaneously.

Let us now consider the resulting hydrodynamic response of the flyer in the early phase of the interaction by means of figure 2.8. At t_0, protons of a certain energy and thus a certain penetration depth or range ρ hit the target of thickness d. As a result of fast heating at constant volume, pressure increases in the energy deposition zone C, and a compression wave (solid line) starts into the unperturbed material A, and reaches the rear free surface at t_1. A release wave (dashed) starts from the front surface of the target and reaches the rear surface at t_2. The rise time t_2-t_1 of the velocity depends on ρ and thus on the proton energy. Strong bunching means higher energies of the incident protons and thus longer rise times (shot 3329 in figure 2.9) if compared to the finite slope of the beam front (shot 3334). After t_2, the velocity histories (curves 1-4 in the upper diagram fig. 2.8) depend on the power histories. Only a sufficiently fast power rise can maintain a constant pressure or velocity level (shot 3334), respectively. Constant beam power means that the velocity drops to zero at the arrival, at t_3, of the reflected release wave. In our case, we have a power shape which consists of a more (shot 3329) or less (shot 3334) marked jump due to bunching and an increase due to the KALIF power rise. Since the voltage rises in this phase, the ion range increases. The release wave which starts at t_1 from the rear surface is reflected from the boundary of the energy deposition zone c and causes the next jump in velocity at t_4. The reverberation time t_4–t_1 depends on the residual thickness of the foil and

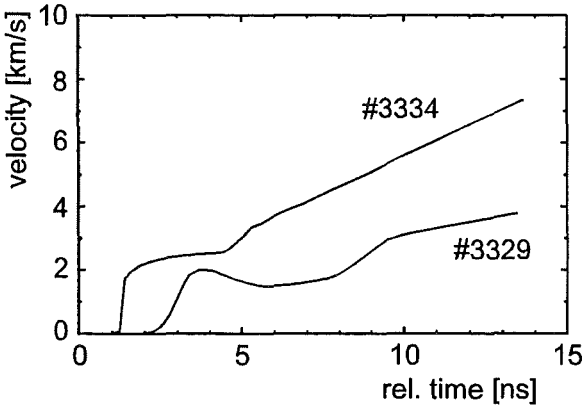

Figure 2.9: Measured velocity histories of two 33 µm thick aluminum foils for different power histories.

the sound velocity as can be seen in figure 2.7.
From the velocity rise times and reverberation periods in foils of different thickness we can deduced the propagation history of the ablation front into the target displayed in figure 2.10. Additional information is supplied by the period during which the rear surface of the flyer is still solid and thus maintains its reflectivity (Baumung *et al.* 1994). The total recording time for thin flyers is limited by the loss of intensity of the reflected laser light. This may be caused by vaporization of the target material when the ion range exceeds the foil thickness, or when a heat wave reaches the rear surface, or when the pressure wave reaching this surface exceeds the melt pressure, or by hydrodynamic instabilities developed during the acceleration process. Much longer recording times are realized in similar experiments with foils backed by LiF windows. In this latter case the reflectivity disappears only due to material evaporation. So, measuring the time elapsed up to the loss of reflectivity for foils of different thickness backed by solid windows also yields the evolution in time of the ablated or evaporated zone.

Up to the peak accelerating voltage the thickness of the vaporized layer is an upper estimate of the proton penetration range. The results obtained by the different methods are in reasonable agreement with range data in literature (Ziegler 1980). However, the maximum value of 26 µm found in some shots for aluminum exceeds the range of 1.5 MeV protons. This could be due to the accidental presence of higher energy protons or due to thermal effects. The role of thermal conduction is investigated theoretically and in experiments. To investigate the role of thermal conductivity from the ablation zone into the adjacent cold matter

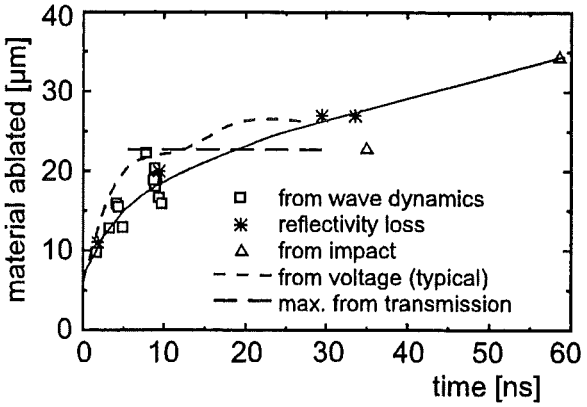

Figure 2.10: Evolution of the thickness of the ablated material layer as a function of time. Different points were obtained in different experiments by different methods.

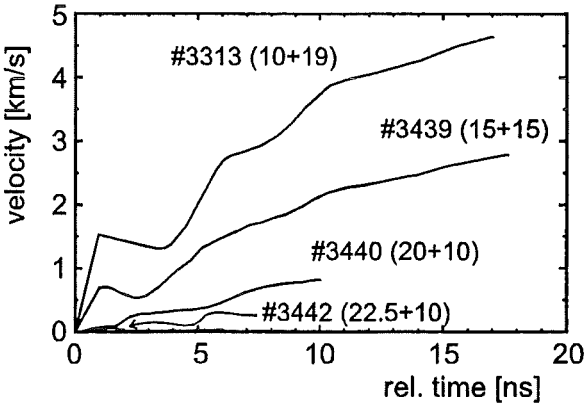

Figure 2.11: Velocity histories measured with different filter/flyer combinations. The gap between the two foils was ~2 mm to avoid any hydrodynamic interaction during the KALIF pulse.

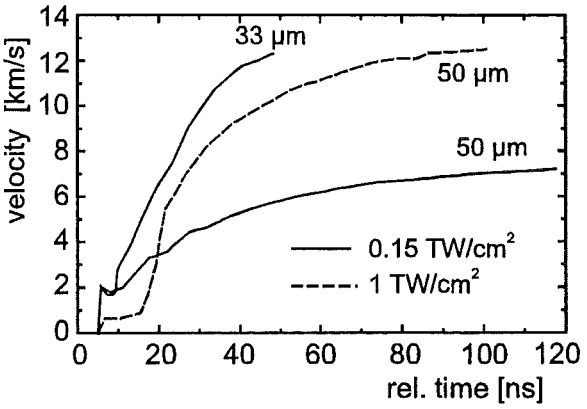

Figure 2.12: Ablative acceleration of aluminum foils by the $B_\odot$ (0.15 TW/cm^2) and the appl-.-B diode (1 TW/cm^2).

experimentally, two foils separated by a gap were irradiated with proton beams. In this case, the first foil is a filter which reduces the power density. The 2 mm wide gap is to hydrodynamically and thermally separate the second foil during the KALIF pulse. As can be seen in figure 2.11, the power transmitted by a 22.5-µm-thick filter is negligible. This confirms that the evaporation zone markedly expands beyond the proton range within a few tens of nanoseconds.

2.3.2. Flyer materials and velocity

The acceleration histories of aluminum flyers driven by the two ion-diodes available on KALIF is compared in figure 2.12. A maximum velocity of 12.5 km/s was reached with a 50 µm foil using the applied-B diode, and for a 33 µm thick foil with the B_θ-diode. As a result of material ablation, the residual thickness of the foils at the moment of peak velocity was ~25 µm and ~8 µm, respectively. For the different behavior in the beginning cf. fig. 2.6. Figure 2.13 shows flyer velocities over the whole acceleration process for an aluminum foil of 33 µm thickness, a 25-µm-thick tantalum foil, a 67-µm-thick polyethylene film, and a sandwiched arrangement of 60 µm polyethylene and 11 µm aluminum. In comparison with aluminum, the composite flyer accelerates faster in the beginning but reaches a smaller final velocity despite the similar areal density. The final velocity of the heavy tantalum flyer is much smaller than the velocity of light flyers. This is in agreement to theoretical predictions (Vorobiev *et al.* 1994). It is important to mention that the final kinetic energy density of the residual part of the flyers is about $(1.3\text{-}1.8)\times10^6$ J/m^2 independently of the flyer material. This means that the total energy of the flyer is about 30 to 50 J.

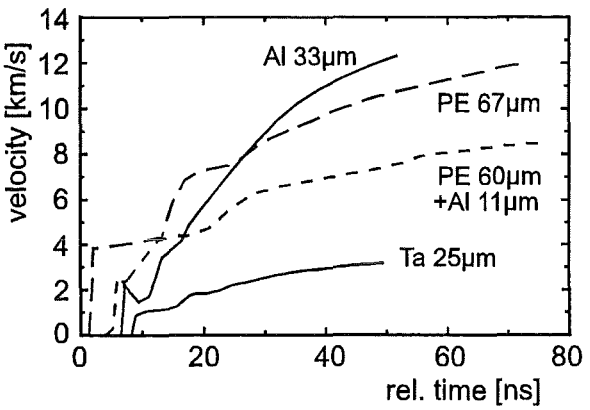

Figure 2.13: Ablative acceleration of thin foils of different materials and a polyethylene ablator and aluminum pay-load combination.

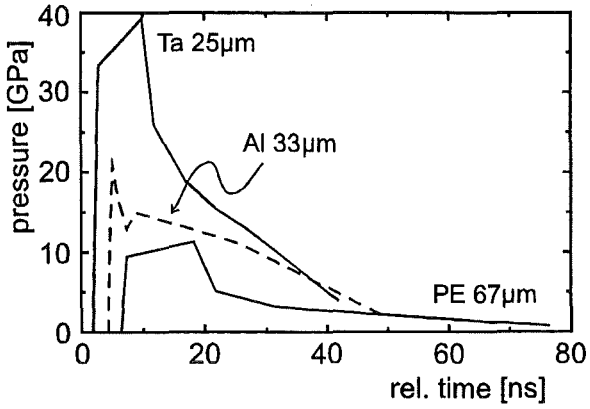

Figure 2.14: Ablation pressure in different materials deduced from the gradients of the velocity histories displayed in fig. 2.13.

It was expected (Ng 1989), that like in gas guns, a low-Z ablator should yield the highest flyer velocities due to the higher sound speed and, as a consequence, higher flow velocity in the ablation plasma at the same pressure. Figure 2.14 shows the pressure histories in the ablation plasma behind the condensed residual part of the flyers. During the initial phase of the

acceleration, the pressure histories were determined from the jumps in the free-surface velocity profiles. The subsequent pressure histories were calculated using the measured acceleration and an estimated thickness of the residual condensed part of the flyer. One can see that the pressure is higher for metal flyers. The specific energy deposition within the ion range is approximately the same for all cases, but the resulting thermal pressure depends also on the matter density. For example, under the conditions of heating at constant volume the thermal pressure is

$$P = (\Gamma/V)E_{th}$$

where Γ is the Grüneisen parameter, V is the specific volume, and E_{th} is the specific energy deposited. The ion range usually decreases with increasing density, thus the specific energy deposition is approximately the same for different materials. The Grüneisen parameter Γ does not vary by more than a factor of two for different materials, but the specific volume V may change by one order of magnitude. As a result, the ion beam generates a much higher pressure in denser materials. It seems that the bulk energy density deposition is very important to obtain large accelerations. In this sense, a low-Z material of high density and high sound velocity such as beryllium or diamond would be optimum ablator materials. A heavy (e.g. gold) tamper of submicron thickness should improve the acceleration efficiency (Ng 1989). Experiments on this problem are under way.

2.3.3. The state of the flyer

Figure 2.15 shows the velocity history of the interface after the impact of a 75-µm-thick aluminum flyer on a thick PMMA plate, and of the impact of a 71-µm-thick aluminum flyer on a LiF plate. The time interval between the beginning of the foil movement and impact was ~33 ns, and ~50 ns, respectively. For comparison, interface velocity profiles obtained by computer simulation using a 1-D hydrocode, are also presented in this figure. For the computer simulation, a range of 22.5 µm was used, thus the residual impactor thickness was 52.5 µm and 48.5 µm, respectively. The calculated duration of the velocity plateau agrees well with the measured value if the impact occurs not much later than the maximum proton energy is reached, and it exceeds the measured value if the impact occurs distinctly later. This is due to the fact that during the voltage rise there is a fast advance of the energy deposition zone into the cold

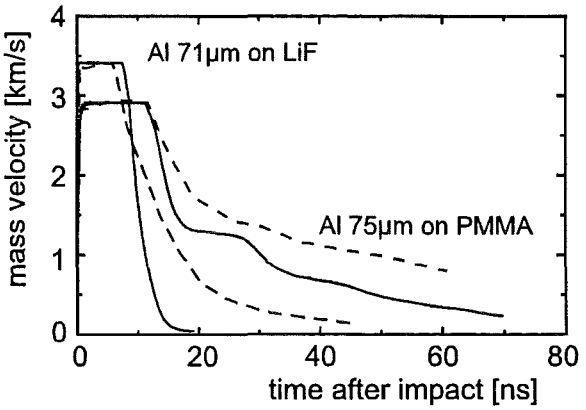

Figure 2.15: Velocity histories of the interface between flyer and transparent window after impact. Experimental data (dashed curves) are compared with simulation results for impactors of same thickness but without a plasma plume behind.

target matter due to the range increase. The thermal conductivity becomes essential after the range has reached its maximum. The measured velocity histories show an essential contribution of the ablating matter behind the residual condensed part of the flyer to the compression pulses generated on impact. The same result has been obtained with a polyethylene flyer and a LiF barrier. This additional component of the shock pulse does not create any problems for shock-wave experiments, especially with relatively thick flyers, but it has to be taken into account in experiments where just the ablation pressure pulse is used instead of a pressure pulse induced by a flyer impact. Experiments will be continued with the goal to find the melting boundary inside the flyer and to estimate the state and dynamic impedance of the ablated matter.

The typical increase rate of the power density in a target irradiated by the B_θ-diode is ~0.005 TW/ns/cm^2. Assuming the range of ions to be equal to 20 μm a specific energy of ~50 kJ/g is deposited during the first 10 ns. If the material heated by the beam remained at normal density a pressure of ~3 Mbar would be generated in the energy deposition zone. Actually, the pressure level is one to two orders of magnitude lower. This is because of two reasons: firstly, the pressure is reduced due to the expansion of matter, and secondly, the pressure generation parameter $\Gamma = P/E$ decreases with heating and expansion of the material from its initial value of ~2 (solid state) to 0.3 (plasma state). If in the beginning of the deposition all the beam energy is transformed into kinetic energy we have an expansion velocity of ~7 km/s for 50 kJ/g energy deposited. This means that the extent of the energy deposition zone after 10 ns will be 10 times larger (the density 10 times smaller) than its initial value. For such an expanded material the parameter Γ reaches a minimum value for strongly coupled plasma of about 0.3 ±0.05 (Ebeling *et al.* 1991). When the energy deposition zone becomes so large that the wave transit time is much larger than the characteristic time of pressure growth due to the energy deposition, the assumption of uniform distribution of parameters throughout the plasma zone is no longer valid.

2.4. Investigation of the spatial variation of the dynamic strength in metals

The ability to create very short compression pulses in samples, and to do measurements with high temporal resolution provide an unique possibility to study the strength of materials under nanosecond load duration. The dynamic tensile strength is studied by the analysis of so-called "spall phenomena" under shock pulse action. Spalling is the process of internal failure or rupture of a body due to tensile stresses generated as a result of reflection of a compression pulse from the surface. The fracturing stress, the so called "spall strength", can be unambiguously determined from the free-surface velocity profiles at spalling (Bushman *et al.*, 1992).

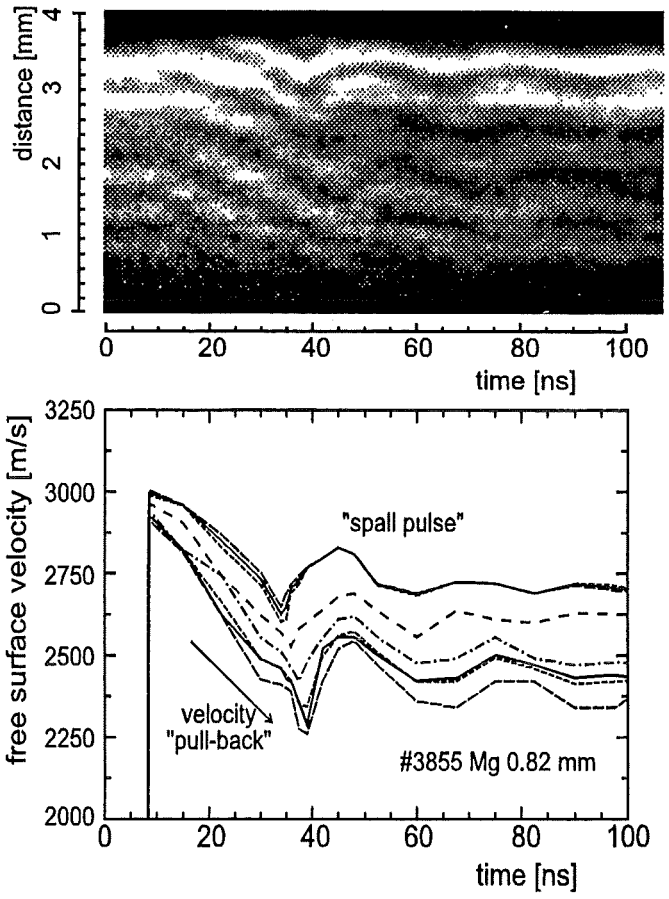

Figure 2.16: (a) Line-imaging ORVIS interferogram across a grain boundary (at ~2.7 mm). Experiment with a 0.82 mm thick cast magnesium Mg95 sample.
(b) corresponding velocity histories at different sample positions showing the velocity "pull-back" and the "spall pulse" typical for mechanical disruption under impulsive loading.

As has been shown earlier (Kanel *et al.* 1996a, 1996b), a spall pulse can be observed only if the damage rate is in some certain proportion to the expansion rate at unloading in the incident compression pulse. The slope of spall pulse front indicates the acceleration of the fracture process: a very fast fracture leads to a jump-like spall pulse front while a decreasing fracture rate is accompanied by a decrease in the slope. The dynamic fracture nucleates at imperfections in the material, such as inclusions, triple points between grains, etc.. With the line imaging velocimeter technique, we can hope to construct a strength map and to see some details of the dynamics of fracture initiation and growth. With the goal to estimate the potential of this kind of measurements for the investigations of the dynamic fracture of metals, experiments with polycrystalline and monocrystalline samples of magnesium and molybdenum have been performed.
The metals selected for testing in the present study are magnesium Mg95 and molybdenum single crystals.

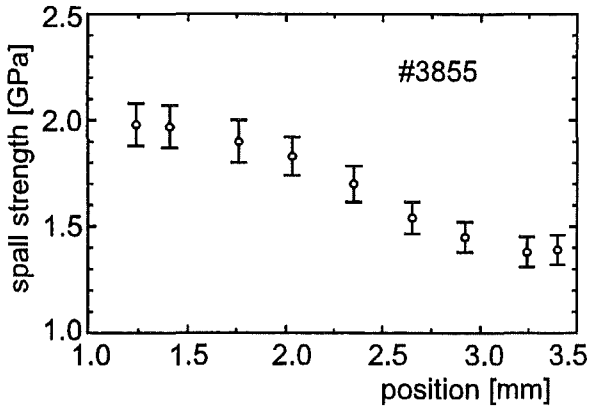

Figure 2.17: Spall strength distribution in magnesium calculated from free-surface velocity profiles presented in fig. 2.16b.

Magnesium. The magnesium Mg95 is "original" cast magnesium which contains 99,95 wt. % of Mg. Other constituents are (wt. %): Fe: 0.0004; Si: 0.005; Ni: 0.0007; Cu: 0.003, Al: 0.007; Mn: 0.01; Cl: 0.005. The grain size of this cast magnesium of a few millimeters should provide the capability to make measurements on separate grains. Figure 2.16a presents the line imaging ORVIS interferogram of an experiment with a 0.82 mm thick magnesium sample. Each point of vertical sections in the interferogram corresponds to a separate point of the measuring line on the sample surface. A vertical displacement of the interference fringes is proportional to velocity increments, so the interferogram indicates directly the velocity histories along the measuring line. A shift by one fringe period corresponds to a velocity increment of 269 m/s. The amplitude of the initial velocity jump in the shock front is not resolved on the time scale used but is known approximately from other experiments with other fringe constants. On the other hand, an exact knowledge of the velocity peak is not important for spall strength measurements, because only the velocity "pull-back" is needed. The evaluation of velocities shown in figure 2.16b was done with a computer code using two intensity histories (horizontal sections of the interferogram) staggered by 1/4 of the fringe period.

The original cast magnesium Mg95 has a grain size on the of order of 1-2 mm. The field of view of the velocimeter included two large grains that are visible on the interferogram at ~2.7 mm due to the difference in reflectivity. Figure 2.17 indicates that the spall strength changes from one position to the other in the sample. Despite of the grain boundary in the ORVIS field of view, there is no sharp jump in the strength distribution. It should be mentioned that, under conditions of one-dimensional shock loading of metals with low yield strength, the stress tensor is nearly spherical. In other words, there is no large anisotropy of the loading and as a result, there is no jump in strength between the grains of different orientation of their crystal structure. Of course, the inter-granular boundary in the ORVIS field of view has to be a site of easier nucleation of fracture, but it seems such fine details can be observed only at a much larger magnifications than that in our present experiments.

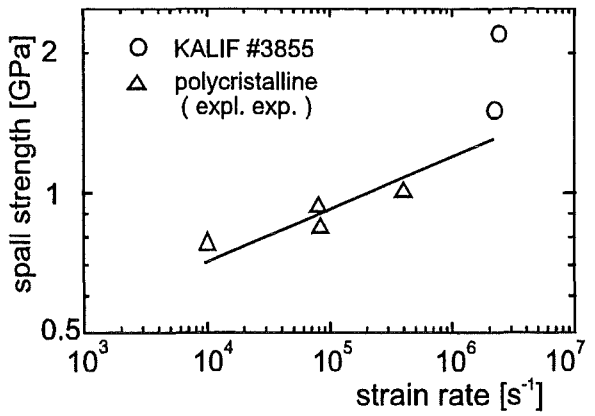

Figure 2.18: Spall strength of magnesium as a function of strain rate at unloading in the incident compression pulse. Triangles are results of explosives driven experiments (Kanel *et al.* 1996c), circles display the scatter of results of the present measurements.

Figure 2.18 shows result of experiment #3855 in comparison with our previous

data (Kanel *et al.*, 1996c) for the resistance to spall fracture of magnesium at lower strain rates. In many previous investigations such dependences are well approximated by a power function over a wide range of strain rate. The new data at highest strain rate are deflected from the power dependence to larger values of the spall strength.

The spall thickness in this shot varied between ~60 and ~80μm. This variation is much smaller than the grain size. This means that the spall crack crossed the grains and the measured spall strength corresponds to that of crystals. It has been found earlier (Kanel *et al.*, 1993, 1994) that the spall strength of copper and molybdenum single crystals exceeds that of polycrystalline samples by a factor of ~2 for molybdenum of ~3 for copper. Since the deviation of the new data from the extrapolated dependence is not large we may suppose that in this experiment, the main spall crack at least partly coincides with the inter-granular boundary below the sample surface which is probably not perpendicular to the surface. Thus, both intra-granular and inter-granular strength are observed, and the intra-granular strength is as much as twice the strength at the inter-granular boundaries.

Molybdenum single crystals. Molybdenum single crystal specimens were cut from a 14-mm-diam bar, polished, and then electrochemically etched to remove surface defects. Deformed single crystals were prepared by rolling in the <110> direction of the growth axis along the (001) plane. It has been shown (Pronin and Aristova, 1990) that molybdenum single crystals retain a single-crystalline structure at all stages of plastic deformation as well as under subsequent long-term high-temperature annealing. Figure 2.19 displays the interferogram and free-surface velocity profiles of an experiment with a 0.55 mm thick molybdenum single crystal. The measurement was performed in the VISAR mode at a velocity-per-fringe constant of 268m/s. Brighter horizontal lines are the scale marks on the sample surface. In this case, to obtain the velocity profiles we have to analyze oscillations of the intensity between its maxima and minima along a horizontal section of the interferogram. Measurements in the VISAR mode do not provide the same accuracy as ORVIS. On the other hand, VISAR interferograms directly display the velocity isolines, that permits, for example, to find out immediately non-uniformities in the spalling process. Thus, a region of relatively increased spall strength was observed in the central part of a sample late into the streak record #3666 displayed in figure 2.19 as a bright spot due to larger velocity decrease in the incident unloading wave. A certain scatter of the spall strength data of metal single

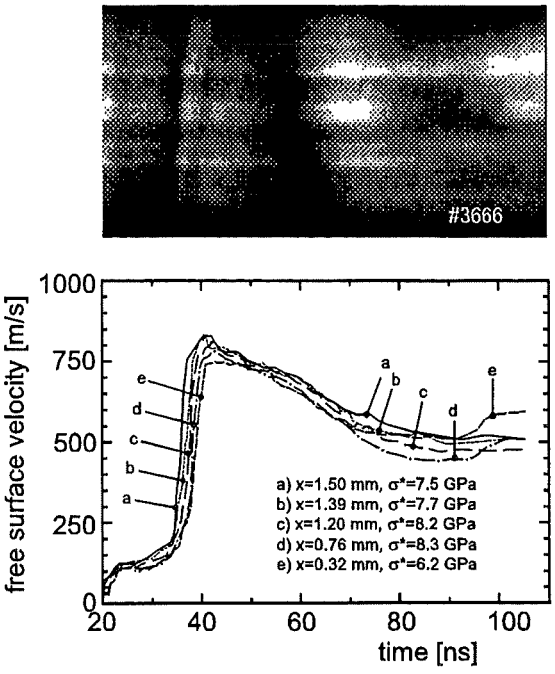

Figure 2.19: Line-imaging VISAR interferogram and free-surface velocity profiles at spalling of a 0.55 mm thick molybdenum single crystal.

crystals was noted in previous investigations. The present experiment shows that the strength can vary from point to point even within the same single crystal. The other essential observation is that the spall signal has a small slope or even, in fact, is not showing up at all in points with smaller spall strengths. The interferogram in fig. 2.19 also displays the peak velocity gradient caused by the radial power density distribution of the beam, and, as a result of different velocities in different parts of the plastic shock wave, a variation of the delay time between elastic and plastic waves emergence at the sample surface.

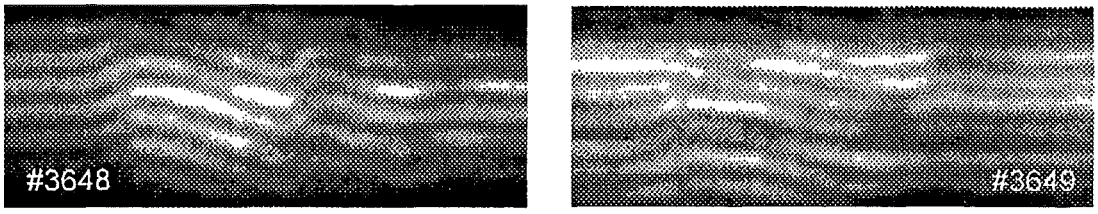

Figure 2.20: Line imaging ORVIS interferograms of spall experiments with deformed 0.28 mm thick molybdenum single crystals. Both samples were cut of the same piece of material. The measuring line was oriented parallel to the rolling direction (#3648) and perpendicular to it (#3649).

Figure 2.20 presents two ORVIS interferograms of spall experiments with deformed molybdenum single crystals. Both samples were cut out from the same piece of deformed single crystal. At insignificant variations of the spall strength, the interferograms shows quite different form of the spall signal. And again, the spall signal has a small slope that even disappears at smaller spall strengths. Figure 2.21 shows the scatter of the spall strength for molybdenum single crystals.

Fracture is a heterogeneous process which nucleates on defects of the material structure. Dimensions of the potential damage nucleation sites vary, ranging in size from inclusions to dislocations and point defects, and, probably, even to thermal fluctuations of the material density. Larger defects are activated at smaller stresses but they are less numerous than smaller defects in the material. The experiment with magnesium shows that a wide spectrum of spall strengths can be realized when the load wave length is less than the grain size of the material. In this experiment, the damage did not nucleate while the reflected tensile wave passed through grains because the tensile stress was not sufficient to activate smaller internal defects. Then the damage obviously is easily nucleated when the tensile wave reaches a grain boundary below the sample surface that is a large nonuniformity where most weak sites of the material are concentrated. When the peak tensile stress reaches a sufficiently large magnitude, initiation of fracture starts inside the grains. This is why we observe saturation of the spall strength in fig. 2.17. The contribution of a visible grain boundary that is nearly perpendicular to the sample surface can probably be observed on a smaller geometrical scale.

Experiments with both deformed and undeformed molybdenum single crystals show that even these materials are not quite homogeneous. In undeformed molybdenum, the range of the spall strength variations along the sample surface is of the order of hundreds of micrometers; for deformed single crystals this value is even higher. Obviously, relatively larger nucleation sites are occasionally distributed in these materials such that they may or may not be in the field of view near the future spall plane. When these are activated, stresses are relaxed and as a result smaller defects in the subsequent layer are not activated. This means that the total amount of damage sites is not large. The general fracture rate is approximately the product of the concentration of damage nucleation sites times their average growth rate. The velocity of crack growth is limited by the sound velocity. The growth velocity of voids is also limited. As a result, in the case of activation of scarce larger defects we have a damage rate which is sufficient to form a minimum in the free-surface velocity profile, but is not sufficient to form a spall pulse front.

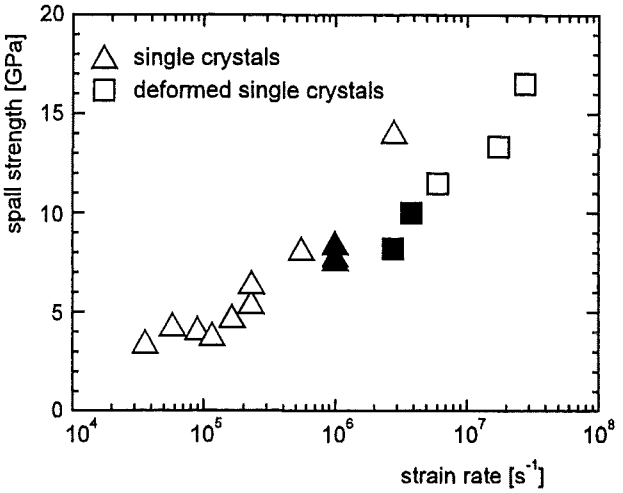

Figure 2.21: Spall strength of molybdenum single crystals as a function of the strain rate at unloading in the incident compression pulse. Triangles and squares present data for undeformed and deformed molybdenum correspondingly. Solid symbols show data from spatially resolved experiments

The volume growth rate of cracks or voids increases with increasing volume. The other process that accelerates the fracture is coalescence of flaws which occurs fast when the distance between them is small. In the case of single crystals, small distances between the damage nucleation sites are present, when uniformly distributed numerous smaller defects are activated. In the case of polycrystalline magnesium, coalescence can occur between larger defects concentrated on the grain boundaries. This can give just a local effect on a scale smaller than the spall thickness when the grain boundary is oriented nearly perpendicular to the wave plane. Much more inter-granular damage nucleation sites are involved in coalescence if the grain boundary is parallel to the wave plane and has a larger effect on the general damage rate. In a next step, we plan similar measurements with an increased spatial resolution to see the fracture initiation on visible grain boundaries. Line-imaging measurements of the dynamic strength can especially be useful for laminated materials after surface treatment. In some sense, spatially resolved spall strength measurements are similar to microhardness mapping routinely performed for materials characterization.

2.5. Melting of metals at unloading after shock-wave compression

Shock compression is accompanied by heating of the material. In case of solids, the temperature increase can cause melting or even vaporization of the material. In figure 2.22, the Hugoniot H, isentropes S, and phase boundaries of matter are displayed in the p,V-plane of the phase diagram (p: pressure, V: specific volume). From the melting curve M in the diagram follows that the melting temperature increases with pressure. Actually, because of the volume and energy increments, there is a melting region with two boundaries separating solid and liquid states, and a mixture of solid and liquid between them. The melt curve is steeper than the isentropes but it is usually flatter than the Hugoniot. There are two possibilities to reach melting in a shock loading pulse. At a certain shock pressure, the Hugoniot crosses the melting curve. At a lower pressure indicated by the point M_u, the irreversible component of temperature increase in the shock-compressed solid results in an isentropic melting of the material.

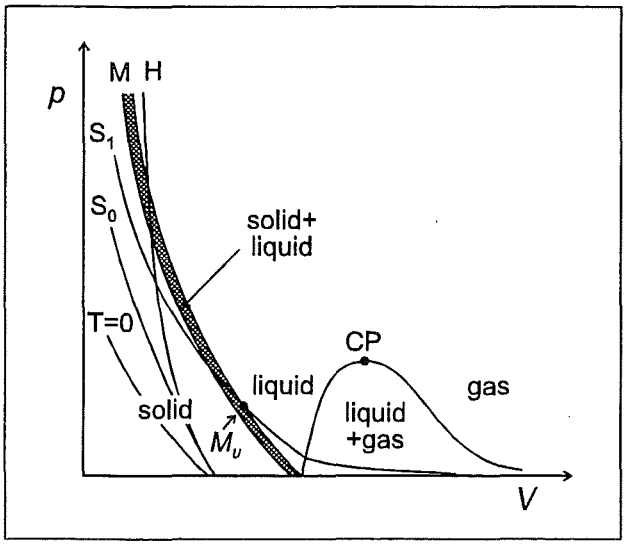

Figure 2.22: Schematic phase diagram of mater in the pressure-volume plane. The relative positions of the Hugoniot H, the isentropes S, the isotherm T=0 K, the melting zone (M), and the vaporization-condensation boundaries are shown.

One of the limitations in the use of shock-wave data is the uncertainty in temperatures reached both during the passage of the shock wave through the material and after unloading. The shock pressure leading to the material melting in the release wave is of a general interest for the verification of equations of state (EOS) but also for practical applications like, for example, the design of spacecraft shields (Alme and Rhoades, 1995). For shock-wave experiments themselves it is often important to know the state of matter. Shock temperatures for metals are calculated using Hugoniot data and the Mie-Grüneisen theory assuming a fluid-like behavior of the matter. Calculated Hugoniot temperatures can then be used to obtain post-shock temperatures assuming isentropic release. Several measurements of the post-shock temperatures of metals were performed earlier (Taylor 1963, King *et al.* 1968, von Holle & Trimble 1976, Raikes & Ahrens 1979). Taylor's results for copper shocked to pressures in the range of 90 to 170 GPa, that includes post-shock melting, are in good agreement with the values calculated by McQueen and Marsh (1960). However, King et al., and von Holle and Trimble found large discrepancies at lower shock pressures. The post-shock temperatures of aluminum alloy and stainless steel 304 measured by Raikes and Ahrens at low and moderate shock pressures are much higher than the calculated values. The difference at low

pressures is explained by the contribution of elastic-plastic work. The discrepancies between the calculated and measured post-shock temperatures decrease with increasing shock pressures while the yield strength rises with increasing peak shock pressure. A change of the state of the sample surface is another possible reason for an overestimation of the temperature. Roughening of the surface by the passage of the shock wave, and by processes such as jetting, can cause an increase in emissivity. Surface roughening decreases with increasing peak shock pressure and the accompanying reduction in the shock front thickness, while jetting becomes more effective with increasing peak pressure. It is known that the reflection of strong shock waves from the surface of a solid body can lead to an ejection of material (Asay *et al.* 1976, Andriot *et al.* 1984, Chapron *et al.* 1988). The effect is sharply intensified when approaching the post-shock melting at release. The development of surface instabilities at melting was also observed with X-ray shadowgraphy of samples after shock compression and release (Belyakov *et al.* 1966, Werdiger *et al.* 1996). As a result, for optically polished surfaces, when a solid-liquid transition occurs on the release isentrope, the reflectivity drops drastically. This phenomenon can be used to detect melting in release of shock-loaded materials (Andriot *et al.* 1984, Chapron *et al.* 1988).

The bell-shaped radial velocity distribution of an ablatively accelerated flyer foil (see fig. 2.5a) inspired us with the idea to employ the nonuniformity of the flyer velocity, and the line-imaging velocimeter capabilities to measure the shock melt pressure. Using a target foil to obstruct a part of the flyer plate up to the vicinity of the ion beam axis we measure the linear velocity profile along a 4-mm line of both the flyer and the target simultaneously. With an appropriate velocity interval chosen the shock melt pressure threshold can be contained in the observed pressure interval. The loss of intensity of the reflected laser light is considered indicative of material spraying and instabilities that occur at the free surface upon the shock-wave release into a melting state. The impact velocity interval and the resulting pressure, interval can be adjusted by the total flyer thickness (mass) and-or the distance of the target. Measurements with the line-imaging velocimeter were done in the VISAR and in ORVIS modes. To demonstrate the features of recording a velocity field in the ORVIS mode, the interferogram of the ablative launching of an aluminum foil is shown in Figure 2.23.

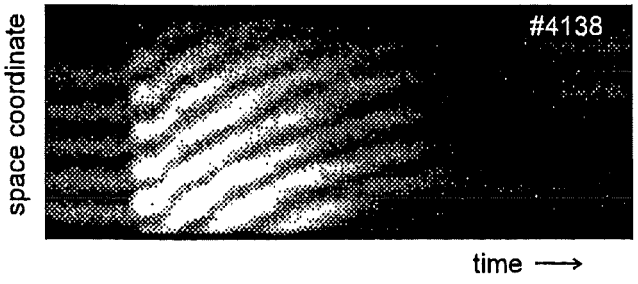

Figure 2.23: Line-imaging ORVIS interferogram of the ablative acceleration of an initially 40-μm-thick aluminum foil. The velocity-per-fringe constant was 2185 m/s. The first velocity jump to ~2.5-3 km/s within ~1 ns is not resolved. The vertical displacement of the interference fringes is proportional to the velocity increment.

Of course, only the 1D velocity field along the measuring line is considered. For the analysis of these interferograms, it is necessary to remember that the velocity varies as a function of time as well as a function of a space coordinate. The interferogram #4138 has been recorded with a 2 mm field of view around the central axis and shows nearly uniform motion of the surface. Under these conditions, the fringes look nearly parallel. In the case of a notable velocity gradient along the measuring line,

the picture changes: the fringes can be parallel only at zero acceleration in all points. That means, they have a zero slope when they are parallel. However, the number of fringes along a vertical section of the interferogram is not maintained. The spacing between fringes increases when the direction of deflection of fringes with increasing velocity coincides with the direction of the velocity gradient. If the velocity points into the opposite direction, the spacing between fringes reduces. At non-zero acceleration, the interference fringes have a slope that is determined both by the acceleration and by the velocity gradient. Again, if the direction of the fringe deflection coincides with the velocity gradient, the fringe slope increases, if not - it decreases. The fringe slope *dy/dx* in the interferogram can be described by formula

$$\frac{dy}{dx} = \frac{\Delta y \cdot \left[\frac{\partial(v/v_0)}{\partial t} \Big/ \frac{dx}{dt} \right]}{1 - \Delta y \cdot \left[\frac{\partial(v/v_0)}{\partial r} \Big/ \frac{dy}{dr} \right]},$$

where x and y are horizontal and vertical coordinates of some point in the interferogram, v_0 and Δy are the velocity-per-fringe constant and the spacing between fringes respectively, r is the coordinate of the same point on the sample surface. The formula shows that the slope of fringes can even become vertical or change the sign.

The ORVIS mode provides a more precise velocity measurement. The uncertainty of the velocity measurements in the VISAR mode is a result of the phase uncertainty of the interference fringes at zero velocity as well as in the moment of impact, but this mode gives directly a clear view of the time dependence of the velocity field.

As usual in velocimeter measurements, the fast acceleration (up to 3 km/s within ~1ns) in the beginning, which is due to the massive energy deposition by the bunched beam front, is not resolved on this time scale. The number of lost fringes has to be recovered from other experiments with greater velocity-per-fringe constants. It is important to note that, after ~10 ns, the velocity distribution is smooth and symmetric to the beam axis. The analysis of interferograms shows that the initial velocity variation across a 8-mm-diameter spot around the axis is about 20% of the peak value. As the flier accelerates, the velocity variation increases to 40%. However, the progressing curvature of the flier causes a delay of the impact on a planar target that increases with the distance from the axis. As a result, the impact velocity interval reduces to 20%, limiting the pressure interval to ≤30%. These figures apply to the diameter of the useful field of view of the velocimeter. The metals chosen for this study are: aluminum, copper, titanium, and molybdenum. According to equation of state data (McQueen and Marsh, 1960, 1970), the peak shock pressure that leads to melting in the release wave is in the vicinity of 65 GPa for aluminum (the melting temperature is T_m= 933.5 K), 137 GPa for copper (T_m=1356 K), 120 GPa for titanium (T_m=1881 K), and 230 GPa for molybdenum (T_m=2893 K). For aluminum impactors, the range of impact velocities necessary to reach these pressures extends from 5 to 9 km/s. All samples were 20 to 70 μm thick foils with the main material content of 99.9 wt. %. The sample thickness was chosen depending on the impact conditions to avoid decay of the shock wave. Figure 2.24 shows the arrangement of the targets used for the shock melt experiments. The axial

dimensions are blown up for clarity. The upper edge of the target is positioned ~1 mm below the beam axis in order to allow a proper extrapolation of the flyer velocity distribution measured in the upper part of the field of view into the region hidden by the target. In the experiments performed so far, aluminum foils of 40 to 75 μm initial thickness were used as flyers. Given the material ablation of 25-30μm up to the impact, the flyer thickness was ~10 to 50 μm, respectively. To ensure planarity the flyer foil was stretched radially while gluing it onto a 40-mm outer and 10 mm inner diameter PMMA support ring.

The impact velocity is virtually the decisive parameter. It can be adjusted by the initial gap width between the flyer and target and by the flyer mass (thickness). Because the preparation of small gaps is difficult, another possibility to control the impact velocity consists in reducing the power density of the proton beam by placing a thin (<10 μm) absorber foil in front of the flyer foil. The gap size was varied between 50 and 130 μm by means of polymer foil spacers of appropriate thickness.

The target consisted of a 8-mm wide strip of a mechanically polished foil that was flattened to remove the ridges formed while cutting. Using adhesive tape on both ends and applying a slight longitudinal tension turned out to be a practicable method to obtain the flattest target surface possible. It is clear that the gap size is an important parameter, and that the target should be plane and normal to the beam axis. However, because the arrival of the shock-wave at the rear free surface of the target is recorded for each position, the moment of the impact and thus the impact velocity is known even if the gap is not parallel.

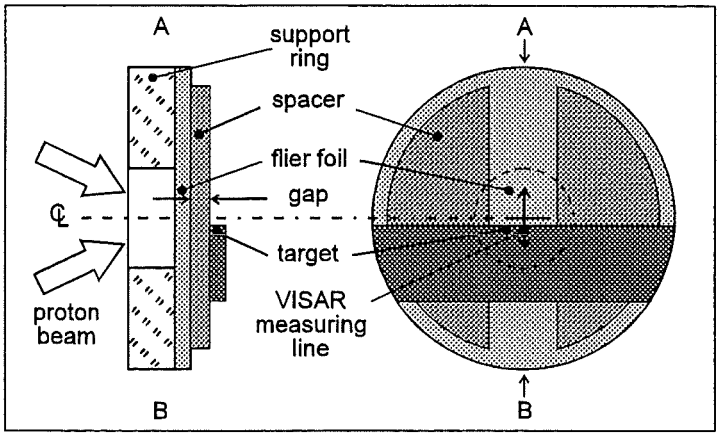

Figure 2.24: Target arrangement. The foil to be launched is glued to a support ring. Spacers allow to adjust defined gap widths and assure the proper orientation of the target. Radial and axial dimensions are not at the same scale. The total diameter is 40 mm, the flier foils were 50-75 μm thick, the gaps were varied between 50 and 130 μm, and the targets were 50-70 μm thick.

Aluminum. Given the scatter of the peak power density of 0.15±0.05 TW/cm^2 and uncertainties in adjusting of the gap sizes in the 50-μm range a series of experiments is needed for determining the shock melt pressure. Figure 2.25 displays streak records of experiments leading to different states of the target rear free surface. In all cases, the fringe constant was v_0 = 0.773 km/s and the initial jump corresponds to ~3.5 lost fringes. The fringe counts and the space-time curve of the impact (solid line) - taking into account the shock-wave transit time through the target of ~6 ns - are added for clarity.

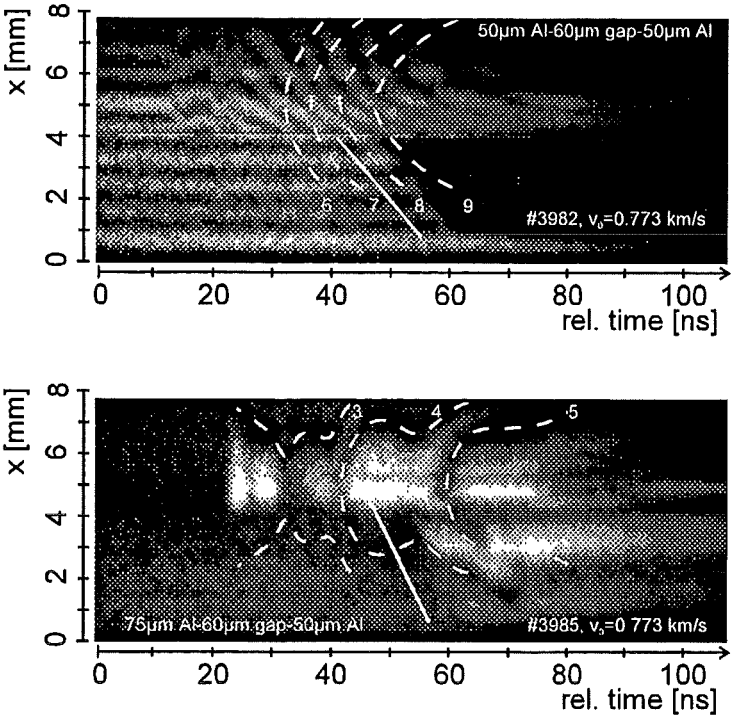

Figure 2.25: Line-imaging ORVIS (top) and VISAR (bottom) interferograms showing the flier acceleration (upper part) and the effect of the impact. The dashed lines indicate curves of constant fringe shift for the ORVIS recording, and the locations of the dark fringes for VISAR, the numbers give the fringe count. The solid line indicates the space-time-curve of the impact at the opposite side of the target. The VISAR record starts with a dark fringe. The results demonstrate the loss of reflectivity on the target rear free surface at the impact velocity of 5.4 to 6 km/s and maintained reflectivity at the impact velocity of 3 to 3.5 km/s.

Figure 2.25 shows a line-imaging record in the ORVIS and VISAR mode, respectively, of experiments with impact velocity above and below the melting conditions. Lines of equal fringe shift and velocity (dashed curves), respectively, and the corresponding fringe counts have been added for clearness. The solid curve depicts the space-time curve of the flyer impact on the opposite side of the target. The impact velocity was varied by changing thickness of the flyer foil between 50 and 75 µm. Besides this, the beam power was unexpectedly low in the shot #3985. In the first case, the impact velocity drops from the peak value of 6.0 km/s down to an estimated velocity of 5.4 km/s at the lower edge, corresponding to a pressure interval of 65-76 GPa. The velocimeter signal at the target rear surface disappears along an approximately straight line. At lower shock pressure near the edge of the interferogram, shifted fringes are recorded for a very short period. The continuous fringe at the bottom of the record does not indicate any velocity variation at this level. Most probably, this is an artifact due to the rim of the support ring screening the ion beam at this position.

The VISAR record of the low-pressure experiment started with zero intensity, the dark fringes are indicated by the dashed curves together with the fringe count. The impact velocity in this experiment was 3-3.5 km/s, corresponding to a 30 to 36-GPa pressure interval. The reflectivity is clearly maintained. Horizontal fringes in the interferogram display the target velocity distribution after impact. As a result of momentum exchange, the flyer velocity drops to zero after collision, and the flyer does not interact anymore with the target foil but it is continuing to screen the target foil from the beam. Therefore, the target surface maintains a constant velocity after a short oscillation. This velocity oscillation is a result of wave interactions in the target. Since the flyer thickness is less than the target thickness in the moment of collision, part of the unloading wave originating from the irradiated surface of the flyer have reached the target rear surface and cause the velocity decrease. The velocity decrement is limited by the portion of the release wave that passed through the interface

and also by the dynamic tensile strength of the target material. Since there is radial velocity distribution, the velocity oscillation appears as vertical oscillation of fringes in the interferogram. It has been shown earlier (Kanel *et al.* 1996) that the spall strength drops almost to zero when the temperature approaches the melting point. Thus, notable tensile strength is also an indicator of the solid state of matter.

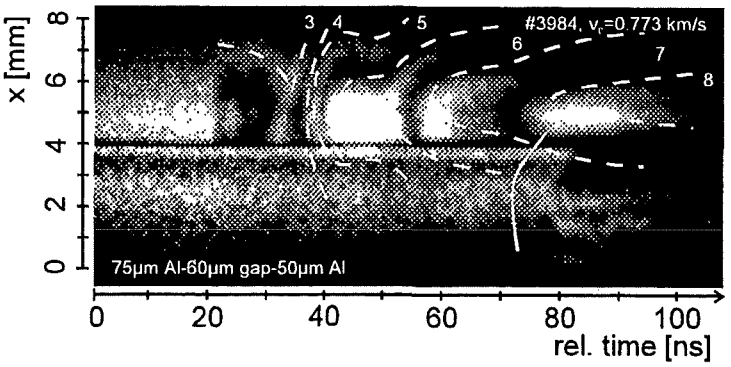

Figure 2.26: Line-imaging VISAR records of impact experiments with melting. The lower half shows the target. In its upper part (2.5 to 4 mm) the impact causes a loss of reflectivity whereas in the adjacent section (1 to 2.5 mm) two fringes appear indicating a velocity gradient. The shape of the space-time curve of the impact (solid line) indicates that the edge of the target was hit latest. Obviously, the target foil is not planar close to the edge. In the lower line-imaging VISAR record the reflectivity of the target is just maintained. The peak impact velocity of 5.3 km/s is close to the threshold at which reflectivity is lost.

Figure 2.26 shows the line-imaging VISAR records of an experiments where the boundary between melted and non-melted states of the target is covered. The records start with a bright fringe. Because the impact occurs fairly late the flyer is already significantly deformed so that the field of view is vignetted at the borders. This makes it difficult to establish an accurate velocity distribution during impact. Obviously, the target foil was rather deformed at the upper edge when it was cut. As a result, the impact starts ~1.5 mm below the border. Nevertheless, this interferogram shows a clear separating line between the upper dark zone where the reflectivity is lost, and the section below, where the emergence of two fringes indicates a vertical velocity gradient. Taking into account the initial phase of the fringe, the threshold velocity is 5.1±0.2 km/s corresponding to a pressure of 62±3 GPa. Another VISAR record covers the impact velocity and pressure intervals of 3.9-5.3 km/s and 42-64 GPa, respectively, and shows two fringes indicating that the reflectivity is maintained, and that there is a vertical velocity profile. Thus, we observed the loss of reflectivity in the impact velocity range between 5.1 and 5.3 km/s. Using the principal Hugoniot and presuming the loss of reflectivity to be characteristic of material melting with the arrival of the release wave at the free surface, we find a threshold pressure for melting in the range of 62 to 65 GPa for aluminum.

Titanium. Four shots with 52 µm thick titanium targets were done using aluminum flyers of 50 µm initial thickness. The impact velocity was varied by varying the gap width. The line-imaging ORVIS interferograms of these four experiments are depicted in Figure 2.26.

The impact velocity in shot #4140 varied between 7.8 and 8.2 km/s because of a small field of view. In this range the lost of reflectivity is surely recorded. In shot # 4142, the impact velocity was between 5.5 and 6.05 km/s. The reflectivity is partly lost near the upper border of the target, that means between impact velocities of 5.7 and 6.05 km/s. In shot #4144, both lower and upper boundaries of the impact

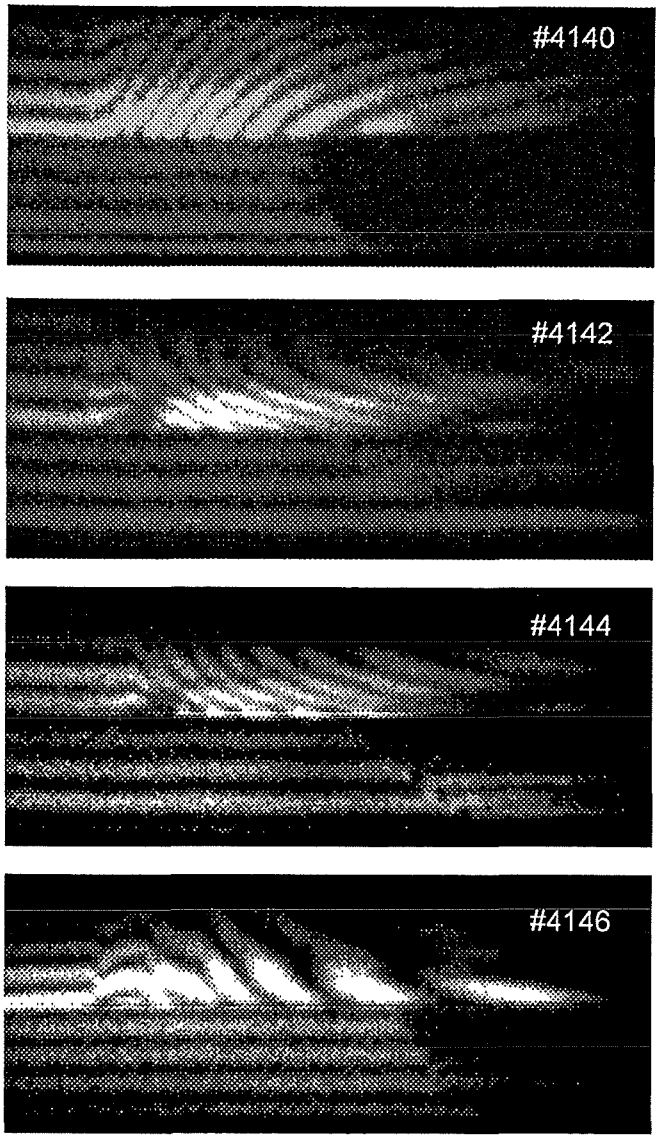

Figure 2.27: ORVIS interferograms of experiments with titanium. The velocity increase corresponds to the positive slope of fringes in shot #4140, and to the negative slopes in the other shots.

velocity range were expanded, reaching from ~5.2 to ~6.3 km/s. At impact velocities of 5.6 km/s and less, both reflectivity and interference contrast are maintained during the whole recording time. This permits to measure the target free surface velocity at the shock front and to recover closed parts of the flyer velocity isolines. Between ~5.6 and 6.3 km/s the partly maintained reflectivity and interference contrast is continuously decreasing to zero. The clearly recorded velocity pullback in the impact velocity range < 5.6 km/s indicates that the material maintains a high dynamic tensile strength even after the high-pressure shock-wave loading. In shot #4146, the impact velocity range was 5.8 to 6.9 km/s. 6 km/s is estimated to be an upper boundary of the impact velocity where some interference fringes were still recorded in this shot. Thus, in the case of titanium the reflectivity and interference contrast are certainly maintained up to an impact velocity of 5.6 km/s, and smoothly disappear in the impact velocity range of 5.6 to 6 km/s this corresponds to shock pressures of 82.5 to 90.8 GPa.

Molybdenum. Molybdenum was investigated as a representative of refractory materials. Figure 2.28 displays interferograms of five experiments using 20 µm and 50 µm thick samples, and aluminum impactors of 40µm and 50µm initial thickness. At impact velocities between 4.7 and 6.9 km/s (shots #4145 and #4149), molybdenum definitely keeps its reflectivity. High contrast of the interference fringes indicates high uniformity of the surface movement. In the range of 7.6 to 8 km/s (shot #4143) a decrease of the reflectivity and interference contrast appears, but fringes remain observable for a relatively long period. In shot #4163, with an initial flyer thickness of 40 µm and a target thickness of 20µm, the impact velocity varies from 8.8 km/s near the bottom of the interferogram to 9.8 km/s at upper border of the

target foil. In this range, a continuous reduction of the reflectivity and interference contrast is recorded. Nevertheless, some weak fringes can be observed for a short time after shock break-out over the whole range. The intense luminosity of the flyer in the last third of the interferogram is caused by the burn-through of the ablation plasma. The slight intensity increase in the lower part is probably due to optical cross-talk. In shot #4161, the impact velocity near the upper target border is 9.4 km/s and then seems to pass through a not well defined maximum in the lower half of the visible part of the target. For a short period, a weak fringe is recorded near the upper border. Therefore, 9.4±0.4 km/s is a best estimate of the critical impact velocity for molybdenum, corresponding to a pressure of 252±16 GPa.

Copper. Two shots were done using 45 µm thick copper foils and aluminum flyers of 50 µm initial thickness as impactors. The interferograms are displayed in figure 2.29. In shot #4166, weak fringes are maintained clearly visible for >10 ns in the lower part of the interferogram up to impact velocities of 6.6 km/s. Their initially negative slope indicates that there is still some notable tensile strength. In shot #4167, the impact velocity exceeded 8 km/s. As a result, the reflectivity is lost very rapidly. The impact velocity of 6.6 km/s corresponds to a shock pressure of 136 GPa.

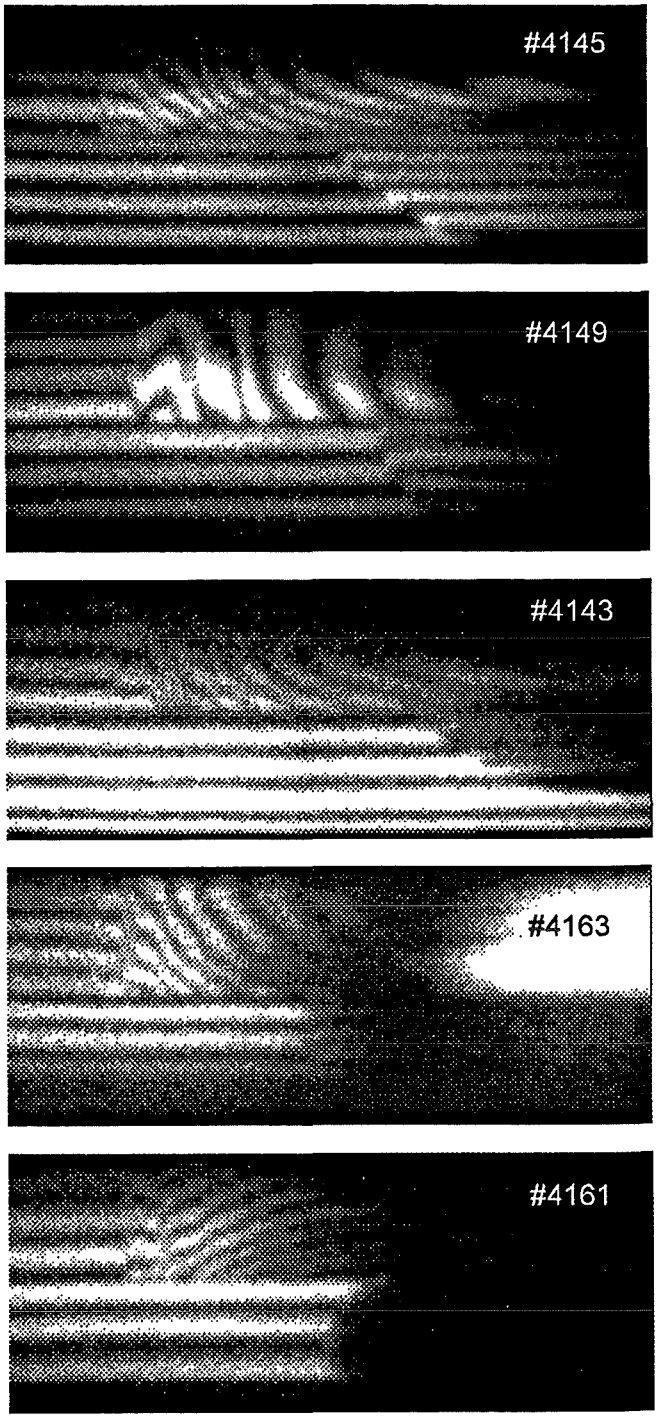

Figure 2.28: Interferograms of experiments with molybdenum. In shots #4145, #4149, and #4143, the target and flyer thickness was 50 µm, and the velocity-per-fringe constant was 780 m/s. In shots #4163 and #4161, the flyer was 20 µm and the target 40 µm thick, and the velocity-per-fringe constant was 1261 m/s.

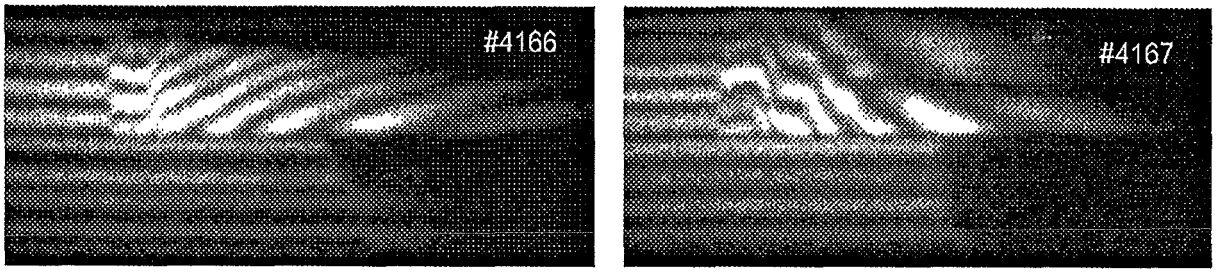

Figure 2.29: ORVIS interferograms of impact experiments with the copper foil targets 45 μm thick. Impactors were aluminum foils of 50 μm initial thickness.

Table 2.1 summarizes results of the experiments performed. There is good agreement between the threshold pressure of maintained reflectivity and the calculated (McQueen & Marsh 1960 and 1970) shock pressure of melting at release for aluminum, copper, and molybdenum, and a discrepancy in the case of titanium. The good agreement means that, unlike low-pressure experiments, the release process of shock-compressed metals is isentropical or nearly isentropical in our conditions. Obviously, the α-ω phase transition in shock-compressed titanium (Razorenov *et al.* 1995 and references therein) is a reason of the discrepancy with the equation of state data.

Table 2.1: Comparison of EOS calculations of shock pressures for melting in the release wave with our experimental data

Material	Calculated shock pressure for melting at release [GPa]	Measured shock pressure causing fast lost of reflectivity [GPa]
Aluminum	65	64±2
Copper	137	136
Titanium	120	86.5±4
Molybdenum	230	252±16

The results we obtained are related to melting onset. As an example, for aluminum, according to calculated melt fraction curve (Henis and Eliezer, 1993), the pressure threshold for melting onset in the release wave is 61 GPa, while the pressure leading to 100% melt fraction is 79 GPa. The interferograms show that there is no sharp drop of reflectivity at melting. Some progressive reduction of the reflectivity and the interference contrast were observed at lower shock pressures, and a small short-time residual reflectivity with lost interference contrast was observed when the shock pressure exceeded the threshold of melting at release. The state of metals after shock compression and release is not absolutely homogeneous. Since under shock-wave conditions the matter is heated as a result of mechanical work, any imperfection in the material creates conditions for the localization of the energy deposition. Thus, hot spots can appear in the matter at pressures somewhat lower than the melting threshold, as was demonstrated by recordings of micro-ejections reference. The volume increment at melting in the hot spots creates conditions for nucleation of surface instabilities and formation of micro-jets.

3. Mathematical model and numerical algorithm

A theoretical analysis of foil acceleration phenomena as described in the previous section requires the knowledge of thermodynamical and optical properties of matter in a wide range of parameters covering, besides the solid and liquid states of matter, domains of nonideal plasma. The main aim of this analysis is to find the optimal design of such launching systems (materials, dimensions and optimal beam parameters) to get the highest possible launching velocity. We solve this problem with the help of numerical simulation based on realistic physical models. Even the presence of reliable physical models (EOS, opacity models and so on) does not guaranty the success of such analysis because of numerous computational difficulties. For example, to analyze the state of the solid part of accelerated foils one needs to solve hyperbolic (hydrodynamics) and parabolic (heat conduction) equations simultaneously. They have different stability criteria $\tau \leq 0.5h^2$ for heat conduction and $\tau \leq 0.5h$ for hydrodynamics (where τ is the time step and h is the size of the cells). To overcome time step restrictions one uses time-consuming implicit schemes for heat conduction problems. Another difficulty is the existence of domains in the flow with different physical properties (compressibility, density, opacity, conductivity) and dimensions (plasma cloud and solid part of the foil, for example). Therefore the numerical schemes should treat compressible flow as well as incompressible flow while resolving accurately plasma-solid and solid-liquid interfaces.

In the present work we apply an ALE (Arbitrary Lagrangian Eulerian) approach using a Godunov code on the moving grids. The grid boundaries can fit flow singularities (shock fronts, contact discontinuities) so ensure the required accuracy for beam-target interaction analysis. Special attention is paid to the state of condensed part of the foil accelerated by the beam.

3.1. Governing equations

The motion of a continuous medium is described by the integral laws of conservation of mass, momentum, energy and porous volume.

$$\frac{\partial \rho}{\partial t} + \nabla \rho u = 0, \tag{1}$$

$$\frac{\partial\, \rho \mathrm{u}}{\partial\, t} + \nabla(\rho \mathrm{u} \times \mathrm{u} + p) = 0, \tag{2}$$

$$\frac{\partial\, \rho \mathrm{h}}{\partial\, t} + \nabla(\rho \mathrm{h u} + \mathrm{pu} - \lambda \nabla \mathrm{T} + S_r) = \mathrm{Q}, \tag{3}$$

$$\frac{\partial\, \rho\, \mathrm{v_p}}{\partial\, t} + \nabla \rho \mathrm{u v_p} = \rho \phi, \tag{4}$$

Here r is the density, **u** is the mass velocity, h is the total specific energy, p is the pressure, V_p is the pore volume per unit volume (porosity), f is the pore growth rate, λ is the heat conduction coefficient, S_r is the radiation energy flux and Q is the

deposited power density. Note that in the present work we account for the heat and radiative transfer only in 1D calculations.

Wide-rage equations of states are required to calculate pressure and sound velocity as functions of specific internal energy and density of the solid component ρ_s (expressed as $\rho_s = \rho/(1-V_p)$). When the porosity of matter becomes greater than some value, the substance does not resist expansion. In this case the volume occupied by the solid component does not change anymore and the porosity grows proportionally to the increase of specific volume of matter.

For the numerical simulation of foil acceleration by ion beam it is necessary to use an equation of state (EOS) that describes with reasonable accuracy the shock compression of matter and the plasma thermodynamics in the energy deposition region. We use wide-range EOS tables (Bushman *et al.* 1989, Ebeling *et al.* 1991, SESAME 1982) and an EOS in the form of a generalized Mie-Grueneisen equation of state, which well describes the experimental data on shock compression of the solid and porous samples in the pressure range up to 1-2 Mbar (Vorobiev *et al.*

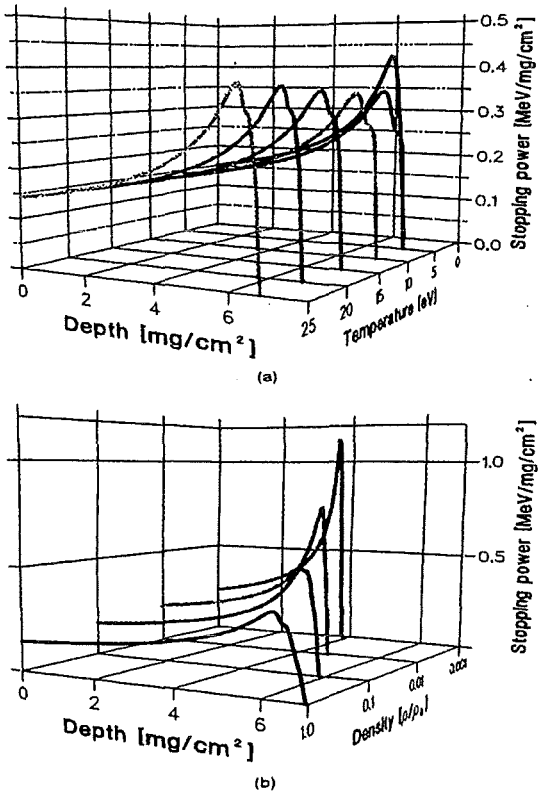

Figure 3.1: The stopping power of 1.5 MeV protons in aluminum for (a) different temperatures and (b) for different densities.

1996). Temperature and heat capacity were calculated using SESAME-EOS tables.

The energy deposition of protons in the target is calculated in the single particle approximation and depends upon the particle energy, plasma temperature and plasma density.

$$S = -\frac{1}{\rho}\frac{dE}{dx} = S_{be} + S_{fe} + S_i + S_{nuc} \quad (5)$$

This is based on the assumption that the total stopping power, *S*, can be represented as the sum of terms describing the contributions by the bound and the free electrons, ions and nuclei. For these calculations the stopping power was calculated by using semi-empirical formulas developed by Polyshchuk *et al.* (1991) (see also Ebeling (1991)). These formulas describe the enhancement of the stopping power as a function of heating and expansion of matter. Results of these formulas are comparable to those of a more detailed model described previously and used to interpret energy deposition experiments at KALIF (Goel & Bluhm 1988). In figure 3.1 we show the variation of the stopping power of 1.5 MeV protons in temperature and density for conditions relevant to plasma generated by the KALIF beam.

3.1.1. One-dimensional code for simulation of beam-target experiments at KALIF

In one dimensional (1D) calculations a Lagrangian grid was used. The meshes in the energy deposition region were refined during the computations when their geometrical size became more than a specified length (2-3 original mesh size).

Radiation heat conduction approximation

Eq.3 can be split into two independent equations describing energy evolution due to hydrodynamic motion and heat conduction.

$$\frac{\partial\ \rho\,\mathrm{h}}{\partial\ t} + \nabla\,(\,\rho\,\mathrm{h}\,\mathrm{u}\ + \mathrm{pu}) = 0, \tag{6}$$

$$\rho\frac{\partial\ \mathrm{e}}{\partial\ t} - \nabla\,(\ \lambda\,\nabla\,\mathrm{T} - S_r\,) = \mathrm{Q}, \tag{7}$$

where e is specific internal energy, S_r is the radiation flux and Q is deposited beam energy. n the case of the radiation heat conduction approximation, the energy flow is proportional to the temperature gradient, the proportionality coefficient is expressed by the Rosseland mean free path, *l*

$$S_r = -\frac{16\sigma T^3}{3} l.\nabla\,\mathrm{T} \tag{8}$$

Thus Eq.7 can be reduced to nonlinear conduction equation

$$\mathrm{C_v}\rho\frac{\partial\ \mathrm{T}}{\partial\ t} - \nabla\,(\ \ \Lambda\,(\rho,T)\nabla\,\mathrm{T}) = \mathrm{Q(x)}, \tag{9}$$

where C_v is the heat capacity and $\Lambda(\rho,\tau)$ ($=\lambda+\frac{16\rho}{3}\mathrm{l}\mathrm{T}^3$)includes both electron and radiative conductivity. Eq.9 is solved using an implicit scheme. We use in our calculations the temperature and density dependence of the electron conductivity coefficient as given by Polyshchuk *et al.* (1991), and for the Rosseland mean free path *l* as given by Tsakiris & Eidmann (1987).

3.1.2. Multigroup diffusion approximation

A more accurate method to calculate radiative heat transfer is by using a multifrequency radiation transport. In this method radiation with different frequency can be transported individually and then coupled to the matter. In the present work we describe the radiation transport in diffusion approximation. This requires that the radiation is isotropic and that the matter is in local thermodynamic equilibrium. This is the case in most part of our system. In case of isotropic distribution of radiation the transfer equations can be reduced to a system of diffusion equations for the spectral density of radiation. Taking into account that the characteristic time of the medium parameter variation is larger than the time of the radiation passing through the region under study, the radiation transfer is described as a quasi-stationary phenomenon. The whole spectrum of radiation is split into a finite number N of frequency intervals (groups). Within each group the absorption coefficient k_i is assumed to be independent of frequency. Thus we have to solve the following system of N equations:

$$\frac{\partial W_i}{\partial x} + ck_iU_i = ck_iU_{eq} \tag{10}$$

$$\frac{c}{3}\frac{\partial U_i}{\partial x} + k_iW_i = 0 \tag{11}$$

where U_i is the spectral energy density of the radiation in the group i.

$$U_{eq} = \frac{8\pi h\nu^3}{c^3\left(e^{\frac{h\nu}{kT}} - 1\right)}$$

is the spectral density of the equilibrium radiation, W_i is the radiation energy flux in group i.

The total radiation flux S_r in eq.3 is calculated as a sum of the spectral fluxes. The system of equations (10-11) can be reduced to a system of elliptic equations:

$$-\frac{c}{3k_i}\frac{\partial^2 U_i}{\partial x} + ck_iU_i = 4k_iU_i\sigma(T, \nu_i, \nu_{i+1})T^4 \tag{12}$$

where $$\sigma = \frac{2\pi k^4}{c^2h^3}\left[\mu\left(\frac{h\nu_{i+1}}{kT}\right) - \mu\left(\frac{h\nu_i}{kT}\right)\right]$$

To determine function $\mu(x)$, the integral expression (Mazhukin *et al.* 1994)

$\mu(x) = \int_0^x \frac{y^3}{\exp(y)-1} dy$ is approximated by the relations

$$\mu(x) = \begin{cases} 1.3799x^3(1/3 - x/8 + x^2/62.4, & x \le 2 \\ 1.3799[6.4939 - e^{-x}(x^3 + 3x^2 + 6x + 7.28)], & x \ge 2 \end{cases}$$

The solution of the system of elliptic equations (12) gives the spectral energy densities and allows to calculate the spectral fluxes from equation (10). $k_i(\rho, T)$ were calculated using the code system ATBASE-EOSPC (MacFarlane & Wang 1994).

3. 2. Two dimensional high resolution Godunov code on moving adaptive grids

One of the most important problems in computational fluid dynamics is the numerical treatment of interfaces between different materials and that of flow discontinuities. Lagrangian methods seem to be the best strategy for solving multimaterial problems because they resolve interfaces crisply, in contrast to Eulerian methods. The drawbacks of Lagrangian methods in turn are that they suffer from mesh tangling and an extreme form of mesh distortion, which leads to time step limitation for explicit numerical schemes. To prevent this, a "near-Lagrangian" mesh rezoning algorithm is used e.g., in CAVEAT code (Addessio *et al.* 1986), which enhance mesh regularity. It has been also proposed to increase the robustness and accuracy of Lagrangian method by moving grid nodes along the streamlines (Lion 1993).

Most Lagrangian schemes require some artificial viscosity to simulate flows with shock discontinuities. This often leads either to a strong shock-front smoothing (if the viscosity is large) or to oscillations of the flow parameters in the vicinity of the shocks. In the present work we use an effective method of numerical integration of Euler equations on a time dependent (so called moving) grid (Godunov 1976). In the framework of this approach the boundaries of numerical grids are moved either in Lagrangian fashion (contact boundaries) or according to the type of boundary (for example, shock front). The locations of interior grid nodes are determined during the grid generation procedure by using coordinates of boundary nodes. As the material flows through the grid cells there is some diffusion error as well as in any Eulerian the above mentioned method. Nevertheless, there exist several possibilities to reduce such errors. One of them is the generation of "near-Lagrangian" grids.

In the present version of our 2D hydrocode we decompose numerical region into subregions with Lagrangian boundaries. Grids are then generated independently in each region using a conformal mapping procedure. This decomposition is provided automatically during the computations. When every subregion consist of only one cell, this approach resembles a Lagrangian method on an unstructured quadrilateral mesh. On the other hand, such a grid provides all advantages of a regular grid.

It is known that the numerical approximation of solutions on an orthogonal grid is as a rule better than on an arbitrary disturbed grids (Godunov 1976). The grid generation procedure can be governed by moving the boundary nodes along the

boundary. Orthogonal grids can be generated in subregions by using such a redistribution of the boundary nodes. We call this procedure as the grid adaptation to the region's form. An important advantage of orthogonal grids is the possibility to simplify the second order extension of Godunov's scheme when we can neglect the mixed derivatives. We have also modified the grid generation procedure to adapt the grid to the solution. Using this modification we can generate finer grids in the vicinity of strong gradients of the flow parameters.

3.2.1. Computational algorithm of Godunov scheme in moving grids

We describe here the algorithm of the 2D computations only briefly. A more detailed description can be found, for example, in Vorobiev *et al.* (1995) and Fortov *et al.* (1996)

The first step of the algorithm is the calculation of the beam energy deposited during the time step. To simplify the algorithm we recalculate the density and the temperature fields onto a fine rectangular grid. Then the energy loss of the ions is calculated along the rows of this grid (which are chosen to be parallel to the beam direction) and recalculated back to the original curvilinear grid. Note that the rectangular grid for the energy deposition calculation covers all curvilinear subregions, so the deposited energy found on this grid is redistributed to all subregions of the curvilinear grid. Let us consider the following steps of computational algorithm only for one subregion.

The next step of the computation is the displacement of the boundary of the subregion. After shifting the boundary to a new position some segments of the boundary can change their type due to interaction with boundaries of the other subregions. The boundary type determines the boundary condition (that is necessary for Riemann problem initial data) and the law of motion of the boundary. For example, a shock-front boundary moves according to Huygens' principle, a rigid wall boundary does not move, and so on.

The third step is an iterative procedure of orthogonal grid generation inside the subregion. The grid generation algorithm is based on a univalent mapping of a rectangular region (ξ,η) in a parametric plane onto a subregion under consideration of physical plane (x,y). If the boundary node distribution is known, the inner grid nodes can be found by solving the following system of equations.

$$\begin{aligned} &\alpha X_{\xi\xi} - 2\beta X_{\xi\eta} + \gamma X_{\eta\eta} = 0,\ \alpha Y_{\xi\xi} - 2\beta Y_{\xi\eta} + \gamma Y_{\eta\eta} = 0; \\ &\beta = X_\xi X_\eta + Y_\xi Y_\eta;\ \ \alpha = X_\eta^2 + Y_\eta^2\ ;\ \gamma = X_\xi^2 + Y_\xi^2; \end{aligned} \tag{13}$$

Coefficients α, β and γ calculated by using node coordinates at the previous time level are used in iterations. To ensure the grid adaptation to the solution we modify the discretization of derivatives ($X_{\xi\xi}, X_{\eta\eta}, Y_{\eta\eta}, Y_{\xi\xi}$) in the following manner.

$$\begin{aligned} &X^i{}_{\xi\xi} = C_1(X^{i+1} - X^i) + C_2(X^{i-1} - X^i), \\ &\text{where } C_1 + C_2 = 1;\ C_1 / C_2 = F_x{}^i / F_x^{i-1}; \end{aligned} \tag{14}$$

Function F depends on flow parameters and their gradients. The case F=const corresponds to orthogonal grids without adaptation to the solution.

The fourth step is the solution of Riemann problems for inner zones and the calculation of fluxes between the neighboring zones. For an arbitrary equation of state, the Riemann problem can be solved only numerically. Nevertheless, we employ an exact solver of this problem only in the vicinity of flow discontinuity. Most of the Riemann problem computations are done either in isentropic or in acoustic approximation.

Second order extension of Godunov's scheme can be obtained if we assume a piecemeal linear distribution of flow parameters inside of the grid cells. To conserve the monotonicity property of Godunov's scheme we use the "minimum derivative principle" proposed by Kolgan *et al.* (1972) and Kopchenov (1983). The main idea of this principle is to choose the minimum possible derivative when interpolating the values from the zone center to the boundary with the neighboring zone, where the Riemann problem is solved. If the grid is orthogonal, derivatives only in one direction (either along the grid rows, or along the grid columns) only are important for interpolating cell-centered values to the boundaries of the cells. This simplifies the realization of the "minimum derivative principle".

3.2.2. Test calculations:

To demonstrate capabilities of the 2D code we consider the problem in which a sphere is impacting on a slab. One of the most difficult tasks for any 2D Lagrangian code is to compute the hypervelocity penetration of a projectile into a thick target. We consider two different approaches to the numerical simulation of the hypervelocity impact of an iron projectile moving with a velocity of 10 km/s on a thick aluminum target: The first one is to use a "near-Eulerian" grid, which covers the region of the target where the shock wave propagates. The second method is the fitting of the shock wave by moving the boundary of the grid with the shock-front velocity obtained by a Riemann solver. The second method in fact, is more accurate to resolve the shock front and is computationally more economical, because it does not require a grid in undisturbed regions. On the other hand the shape of the numerical region is more complicated and, as a consequence, the grid generated is not as orthogonal as in the first case. The results of computations corresponding to these cases are shown in Fig. 3.2. There are two subregions used in the case of shock-fitting grid. One corresponds to the projectile, the other covers the disturbed region in the target. In the other case (near-Eulerian grid) three subregions are used in computations.
As it has been shown by (Vorobiev *et al.* 1995) for the case of steady gas flow, the second order extension of Godunov's scheme is not so sensitive to distortions of numerical grid as is its first order counterpart. We demonstrate below (Fig. 3.3 and 3.4) the results of simulation of hypervelocity impact obtained using the first and the second order Godunov scheme both on the shock fitting grid and on the near-Eulerian grid. Our results generally confirm the conclusions obtained in (Kopchenov *et al.* 1983). For the second order scheme (Fig. 3.4) the difference between the results obtained on different grids is negligible, while for the first order scheme there is a big difference in the amplitude of the shock wave calculated on the shock fitting and on near-Eulerian grid. It is natural, that the shock front dissipation is more pronounced in the case of the first order scheme than in the case of the second order.

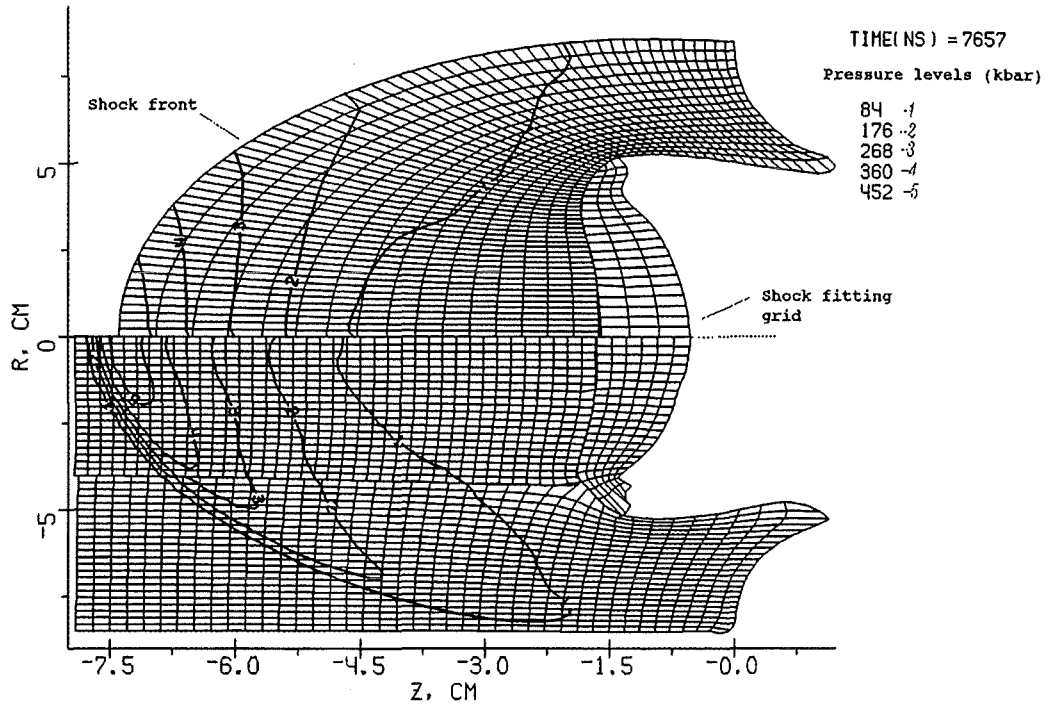

Figure 3.2: Numerical grid and pressure levels for a hypervelocity impact problem. The result obtained using the shock fitting grid is shown above the axis and that one using the "near-Eulerian" grid is shown below the axis.

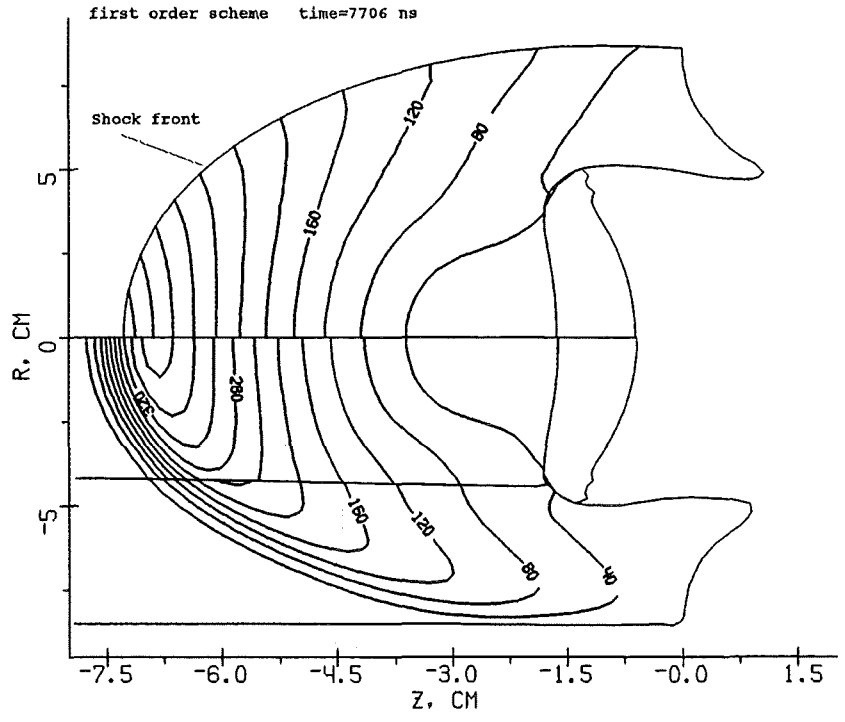

Figure 3.3: Grid boundaries and pressure levels (in kbars) for the shock fitting grid and the "near-Eulerian" grid. First order scheme.

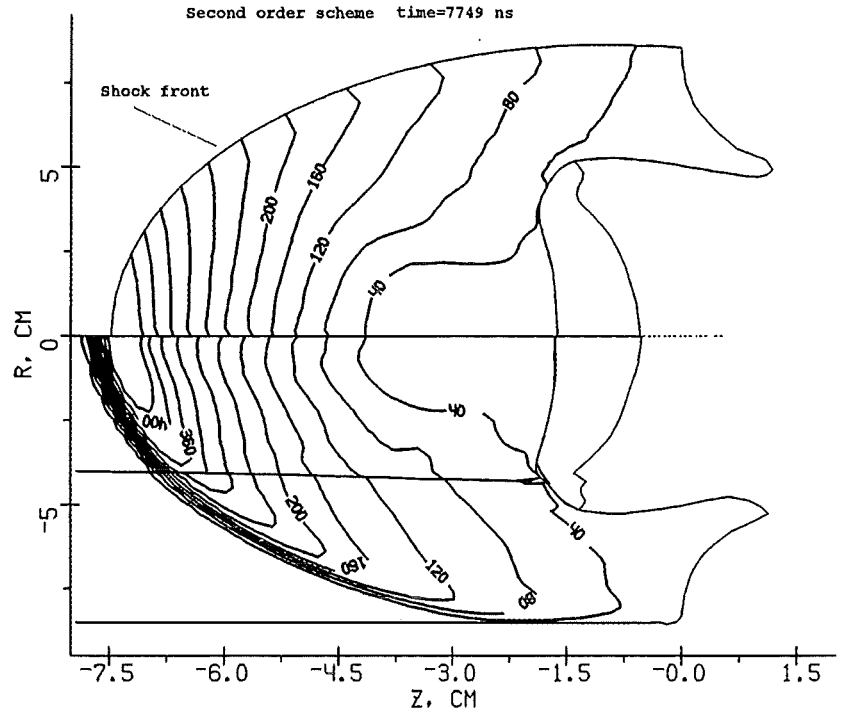

Figure 3.4: Grid boundaries and pressure levels (in kbars) for the shock fitting grid and the near-Eulerian grid. Second order scheme.

The results considered above were obtained on the moving grids without any adaptation to the solution. We examine the influence of this grid adaptation on the results of computations for 10 km/s impact of spherical iron projectile on an aluminum target. As it is seen in Fig. 3.5, the grid adaptation to flow parameter gradients gives better resolution of the shock wave generated at the same computer resources.

We see that Godunov's scheme on moving grids and it's second order extension (Kolgan scheme) coupled with the algorithm for partitioning a numerical region into subregions shows a good robustness and flexibility for multimaterial problems of computational fluid dynamics with large distortions. The other advantage of partitioning a numerical region of complicated shape is the possibility to generate orthogonal grids in subregions.

We have developed a second order Godunov's scheme applying Kolgan's algorithm of "minimal derivative". We found that Kolgan's scheme is not very sensitive to the form of the moving grid as the original Godunov's scheme. In the framework of the Godunov's scheme on moving grids shock fronts can be fitted in a rather simple manner by moving the grid boundary with shock front velocity obtained by the Riemann problem solver. The application of shock fitting grids reduces the computational time by a factor of 2-3 at a level of accuracy comparable with results obtained with near-Eulerian grid.

An additional possibility to increase the resolution of computations inside the numerical subregions is the grid adaptation to the solution. Such grids can be very effective for problems with multishock interactions.

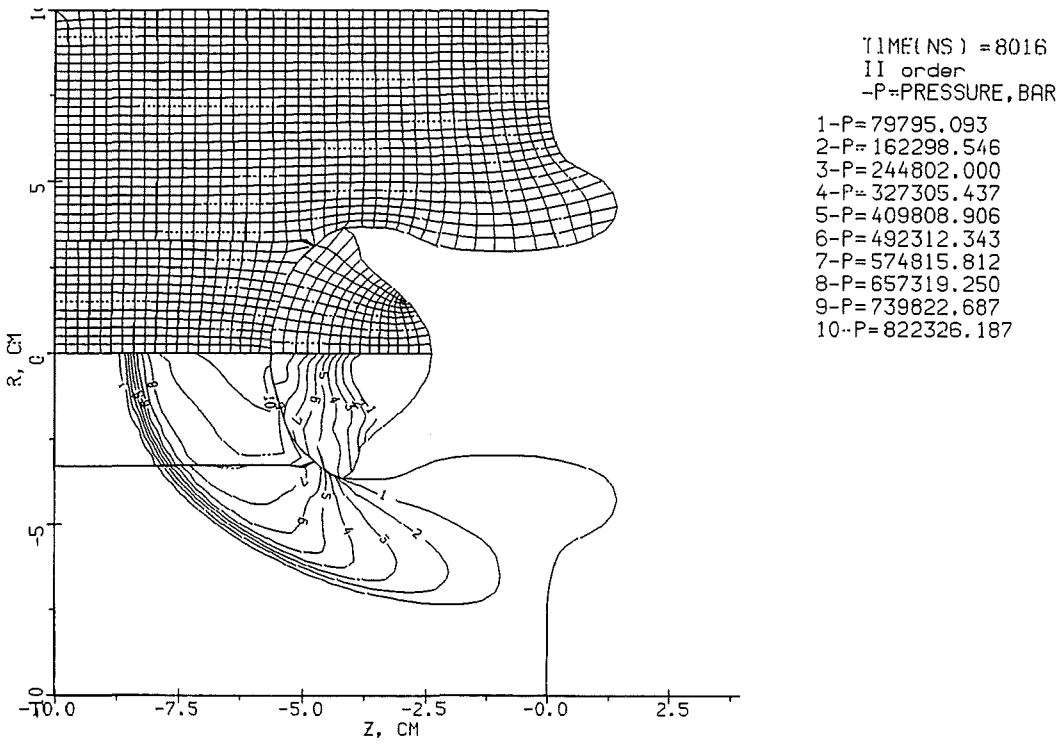

Figure 3.5 (a): Grid and pressure levels for a 10 km/s impact of an iron ball on an aluminum plate (without grid adaptation to the solution).

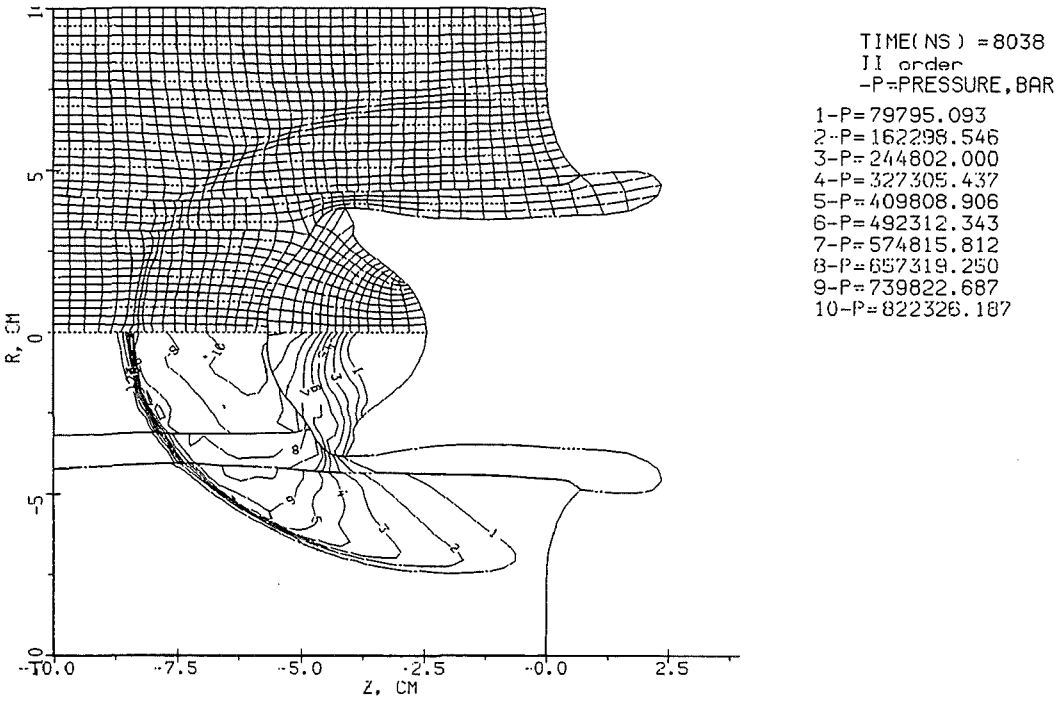

Figure 3.5 (b): Grid and pressure levels for a 10 km/s impact of an iron ball on an aluminum plate (with grid adaptation to the solution).

4. Simulation results

4.1. 2D simulation of the beam-target interaction

Comparison of one-dimensional and two-dimensional code results

As we use different codes for 1D and 2D simulations it is interesting to compare the results obtained with both codes for a 1D plane problem of an aluminum-foil acceleration with the KALIF beam. In Fig. 4.1 both results are presented. It is seen that the difference in both calculations is small except at the extrema, which is mainly due to the different number of cells used in the codes. We have also plotted experimental data into the figure. The length of the reverberation plateau is well replicated by both codes. Both codes predict higher final velocities than the measured ones. The difference can be attributed to the equation of state and other physical models which are the same in both codes and not optimized to obtain agreement with experiments.

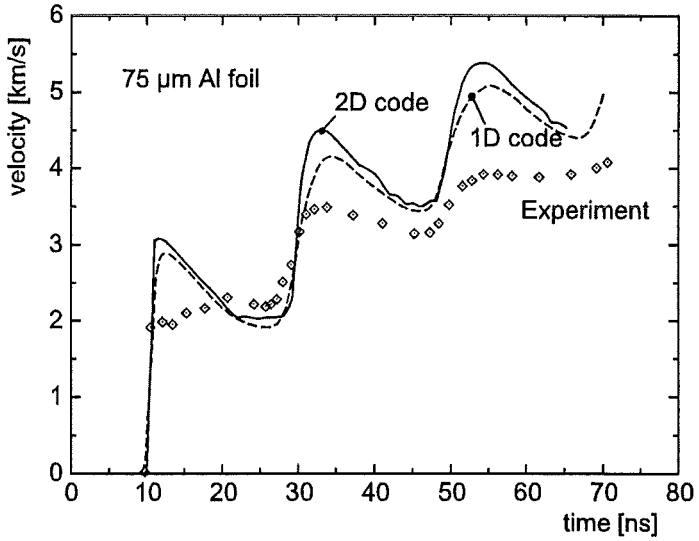

Figure 4.1: Comparison of simulation results obtained with 1D Lagrangian and 2D moving grid Godunov code.

4.1.1. Beam-target interactions in the case of nonuniform irradiation

One dimensional simulations in slab geometry assume that the target has a definite thickness in the computational direction and a unit surface. Consequently, 1D simulations assume a specially homogeneous irradiation of the target. On the other hand, the experimentally determined spatial beam front is more like a two-dimensional Gaussian with a flat top and, accordingly, the maximum acceleration of the targets have always been found in the beam center (Baumung *et al.*, 1995).

Radial gradients of the deposited power density in the beam spot are expected to produce radial pressure gradients so that the plasma generated in the beam center may not only expand normal but also tangential to the target surface, thereby reducing the maximum available target acceleration (as measured in the beam center). Since one-dimensional computations cannot account for tangential forces (pressure gradients) this could be an important limitation of these models.

In order to check the influence of tangential forces we performed the following computations in two spatial dimensions: A 33 - 75 µm thick aluminum foil is irradiated by a KALIF proton beam, once with a homogeneous beam front and once with a power-density distribution having a two-dimensional Gaussian shape with a fwhm of 8 mm and with the same the maximum power density as for the homogeneous beam front. The back-surface velocity in the beam center is compared for both simulations in Fig. 4.3.

In figure 4.2. the spatially resolved back-surface velocity (as a function of the radial position from the beam center) is shown as a function of time for the 33 µm aluminum foil. From this figure it becomes obvious that the original Gaussian power-density distribution is almost recovered in the velocity signal. Fig. 4.3 shows a comparison of the velocities in the beam center for the homogenous and the Gaussian shaped beam profile. Both velocities agree quite well, i.e. pressure gradients tangential to the target surface are not important for the target dynamics.

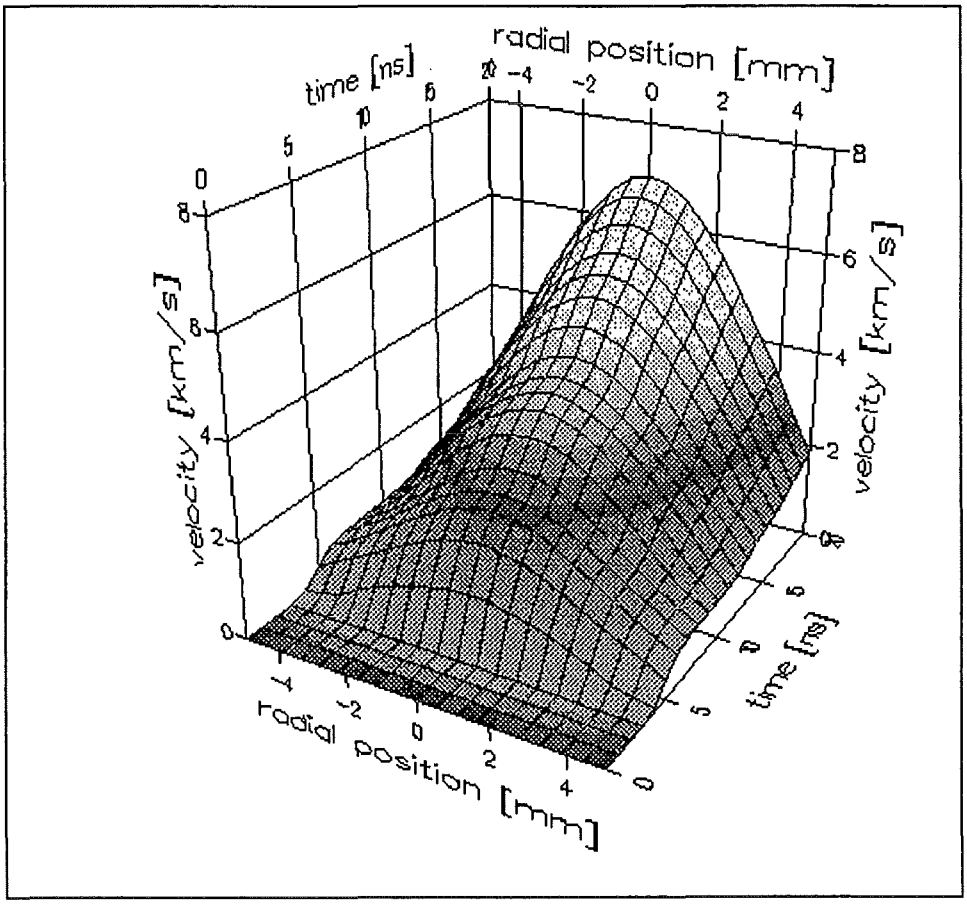

Figure 4.2: Computed back-surface velocity as a function of radial position and time for a 33 µm thick aluminum target.

These results have a number of interesting consequences:

a) an approximate spatial power-density distribution of the KALIF-beam can directly be determined from the measured velocity distribution on the targets on the targets back surface.

b) since nearby surface elements of the target expand almost independently of each other, the full target dynamics can be estimated to a first approximation from a sequel of one-dimensional computations at different radial beam positions. This has already been done e.g. (by McFarlane *et al.* 1996) for the temperature diagnositcs of thin targets, but without any justification of the method used. Finally, velocities measured in the center of the KALIF-beams may be compared with 1D-computations which have been performed for the beam center only, thus saving computational time.

However, it should be noted that any dissipation mechanism not included in the two-dimensional computations (like e.g. thermal conduction or radiative transfer) may modify these results. Thermal conduction or radiative transfer may reduce the temperature and therefore the pressure in the beam center by transport of energy tangential to the target surface. However, one-dimensional calculations have already shown that these physical mechanisms are only of minor importance, at least for the less powerful B_θ-diode. Furthermore, the 2D-calculations do not include the mechanical viscosity of the material which would demand a solution of the full Navier-Stokes equations and is beyond the scope of the present study.

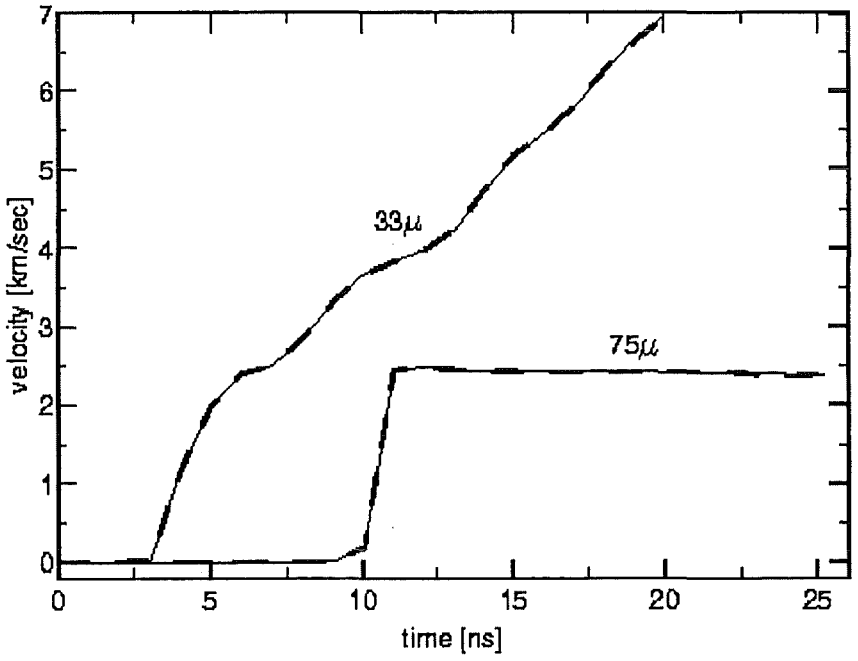

Figure 4.3: Comparison of computed back-surface velocities in the beam center for a spatially homogeneous beam-power distribution (dashed and a Gaussian shaped beam power distribution (straight lines).

4.1.2. Nonuniform irradiation on small scales

To investigate the possible consequences of nonuniform irradiation on small scales (a few μm) we considered a 2D problem in plane geometry. Calculated results in comparison with the uniform case are shown in Fig. 4.4. The thickness of the aluminum foil was 33 μm. As the beam radius is much larger than the foil thickness, we considered one segment of the foil of 10 μm length for both the uniform and nonuniform case (shown in Fig.4.4). In the case of the nonuniform beam, half of the segment was irradiated by a power density of 1.1 W (where W is the power density of the uniform beam), while the other segment was irradiated with 0.9 W. The total amount of energy deposited in both the uniform and nonuniform case, was the same. Such a nonuniformity of irradiance makes the material to flow from the hotter region, where the pressure is higher, to the colder region. As the mass of the absorbing layer is reduced in the "hot" domain, the beam penetrates deeper. When the difference in density between the "cold" and the "hot " part becomes the same order as the difference in power density (20% in the present case) the pressures generated in both parts are about the same, because the thermal pressure can be roughly expressed as $P=\Gamma\rho E$, where Γ is the Grüneisen parameter and E is the specific internal energy. According to this formula, if the Grüneisen parameter is constant corresponding to its plasma value, the higher specific energy of the "hot" matter is compensated by its lower density.

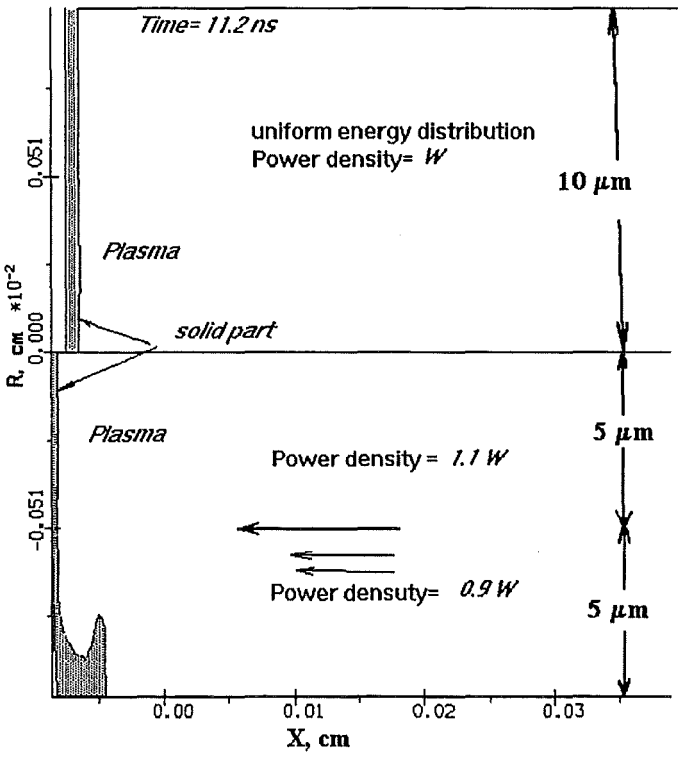

Figure 4.4: Comparison of calculation results for uniform and nonuniform (below zero) irradiation at the same average beam power density W=0.1 TW/cm^2.

It is noted, that the considered problem is not trivial from the computational point of view. The size of the plasma cloud is two orders of magnitude larger than the solid part of the foil. Results shown in Fig. 4.5 and 4.6 demonstrate the advantages of adaptive grid generation (Fig. 4.5) in comparison with the regular grid. In the case of adaptation, the grid is more detailed in the domains with the strong density gradient. This allows to resolve of the plasma-solid interface with higher accuracy.

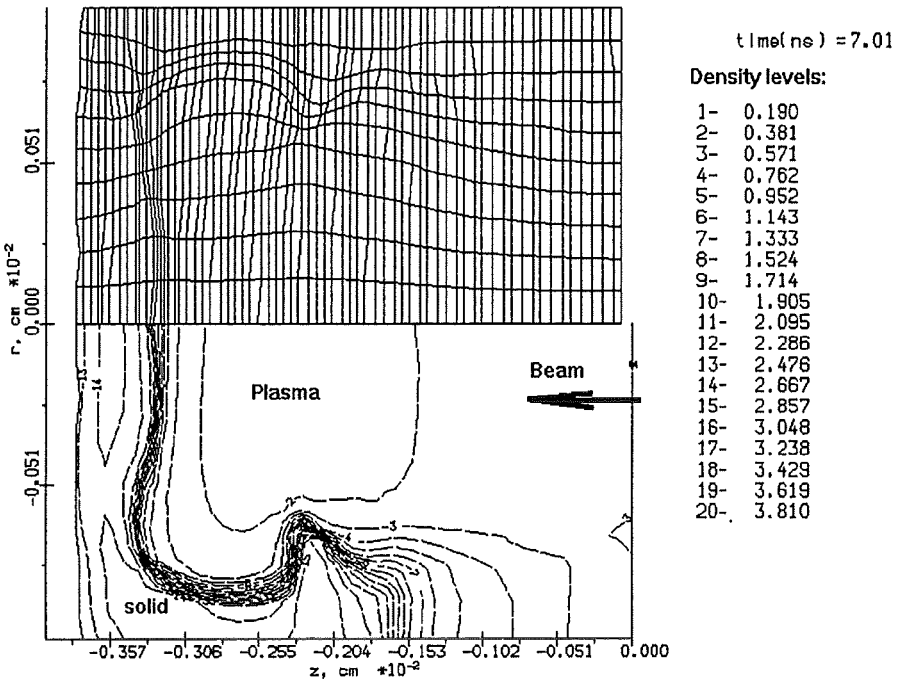

Fig. 4.5: The grid and density levels for a 33 μm Al foil irradiated by a nonuniform beam. The result was obtained with grid adaptation.

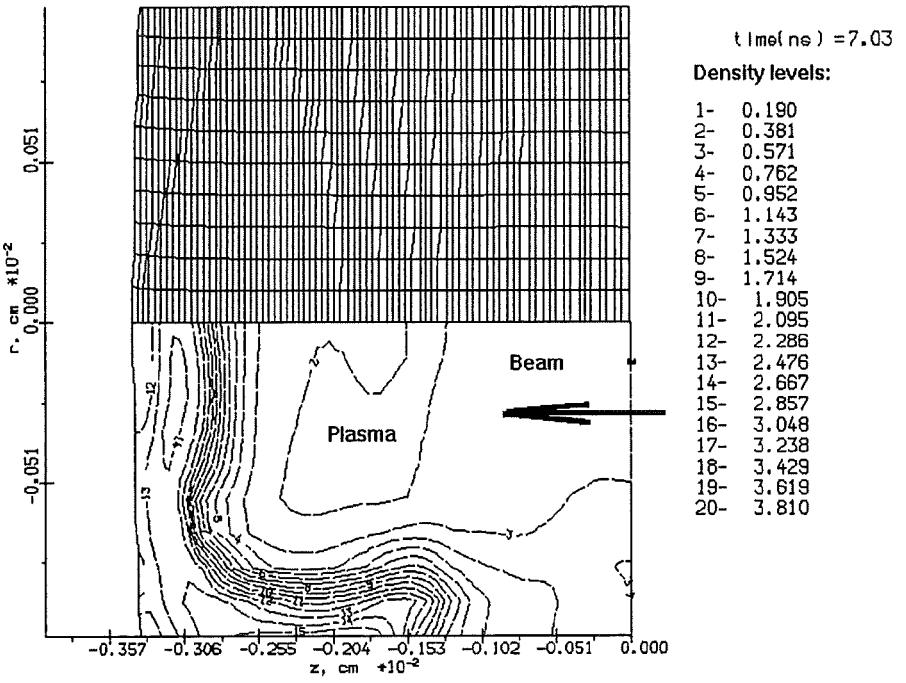

Fig. 4.6: The grid and density levels for a 33 μm Al foil irradiated by a nonuniform beam (without adaptation).

Nonuniform irradiation leads to an additional beam penetration into the target because of the hydrodynamic motion. This leads to a more intensive melting of the payload, than it follows from 1D simulations. This effect should be taken into account especially for thin foils.

4.2. Simulation of foil acceleration experiments at KALIF

Beam energy deposition leads to heating and ionization of solid material in a few nanoseconds. By that time pressures of the order of several hundred kbars are generated in the energy deposition zone. The total beam duration is about 100 ns, while the maximum beam power (about 0.15 TW/cm^2) is reached after 30 ns. A schematic description of the processes during the beam-target interaction is depicted in Fig. 4.7. The motion of the back surface of the foil has been recorded with a high-resolution laser-Doppler velocimeter (ORVIS).

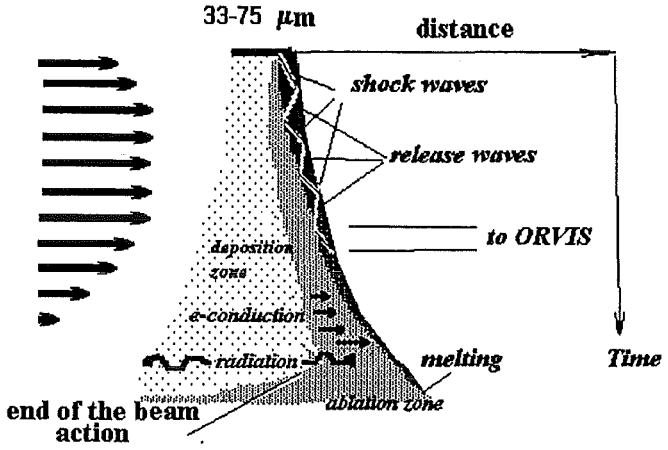

Figure 4.7: Schematic of the beam-target interaction

Wave reverberations between the back surface of the foil and the plasma-solid boundary cause jumps in acceleration. When the shock wave arriving at the back surface has a triangular form the material can even be damaged in release waves by negative pressures (spall damage). The foil is heated by the running waves. Besides that, due to electron conduction, the energy transmitted by radiation from the deposition zone is delivered farther into the solid part of the foil. When all condensed part is melted the rear surface looses its reflectivity and it is no longer possible to use the ORVIS system for velocity registration.

Because of experimental constraints the power and voltage beam profiles varied from shot to shot, we use for our simulations some representative averaged profiles in the simulations. This can explain some differences between calculated and measured velocity profiles. Figure 4.8 shows the pressure profiles in an aluminum foil of 75 μm thickness. When the first shock wave reaches the back surface a negative pressure of the order of 10 - 20 kbar is generated in the release wave. This is less than the spall strength at the strain rates 10^4-10^6 s^{-1} attained in experiments with explosives. If we account for the spall damage in the calculations, negative pressures will relax to zero value with the pore growth. This will lead to an increase of the wave reverberation period (as it is seen in Fig. 4.10), because the pressure gradient in the compression phase becomes smaller. The first shock heats the solid part of the foil from 300 K to 450 K (Fig. 4.9). The heating of the rear surface caused by heat conduction is not significant for a 75 μm-foil during the first 80 ns. For thinner foils (which can be accelerated to higher velocity) this effect is more pronounced. Figure 13 shows the calculated depth of the ablated material as a function of time. Experimental points obtained by different methods (loss of reflectivity and impact measurements on LiF screens) are also depicted in Fig. 4.11.

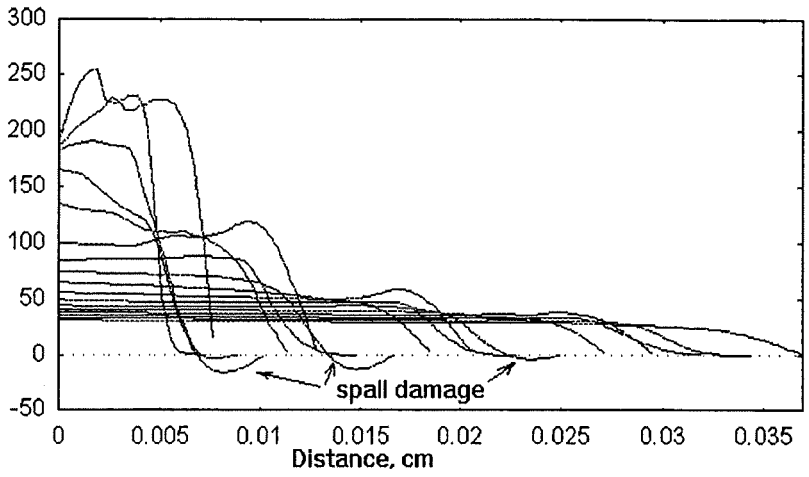

Figure 4.8: Pressure evolution in a 75 μm Al foil. The time interval between profiles is 5 ns.

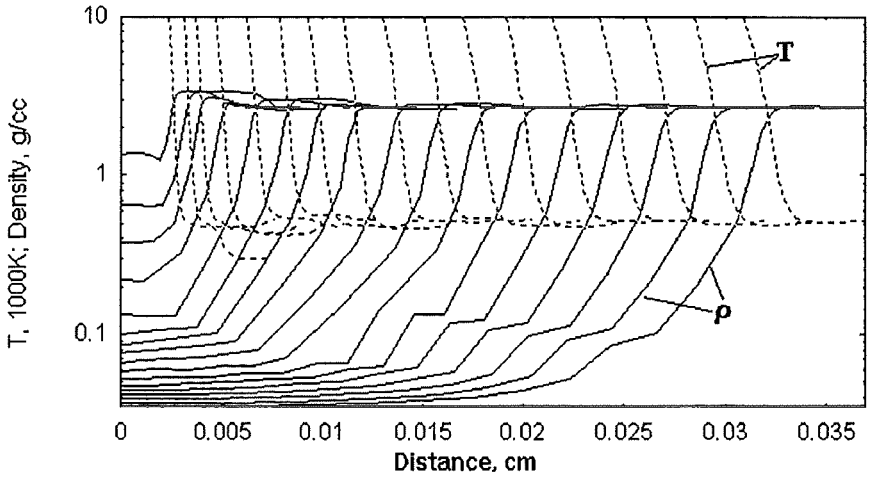

Figure 4.9: Temperature and density evolution in a 75 μm Al foil. The time interval between profiles is 5 ns.

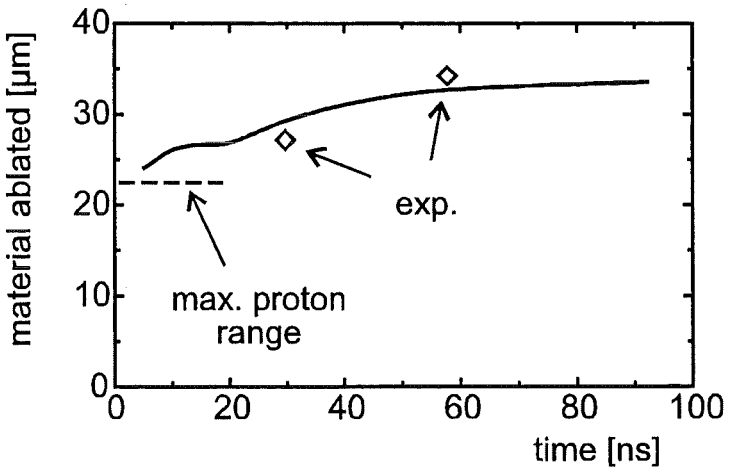

Figure 4.11: Propagation of the ablation front in Al (in micrometers). The maximum proton range is 23 microns.

In order to theoretically investigate the role of thermal conduction on the evolution of the ablation front, simulations have been performed for the impact of a 71 μm thick aluminum flyer on a LiF plate. These computations have shown that the „velocity

plateau" after the impact shows a structure which depends on the place and direction (or phase ϕ) of the pressure wave already generated earlier by the beam-energy deposition. Fig. 4.12 shows two computed velocity signals after the impact at two different phases. In model A (impact at ϕ=0), the rear-surface velocity of the flyer drops to about one half of the initial value but soon increases by about 1 km/sec due to acceleration by the just arriving pressure wave. In model B (impact at ϕ=π) the arrival of the pressure wave at the rear surface is seen as a velocity hump near the end of the plateau. Also, the length of the plateau is somewhat increased in this case.

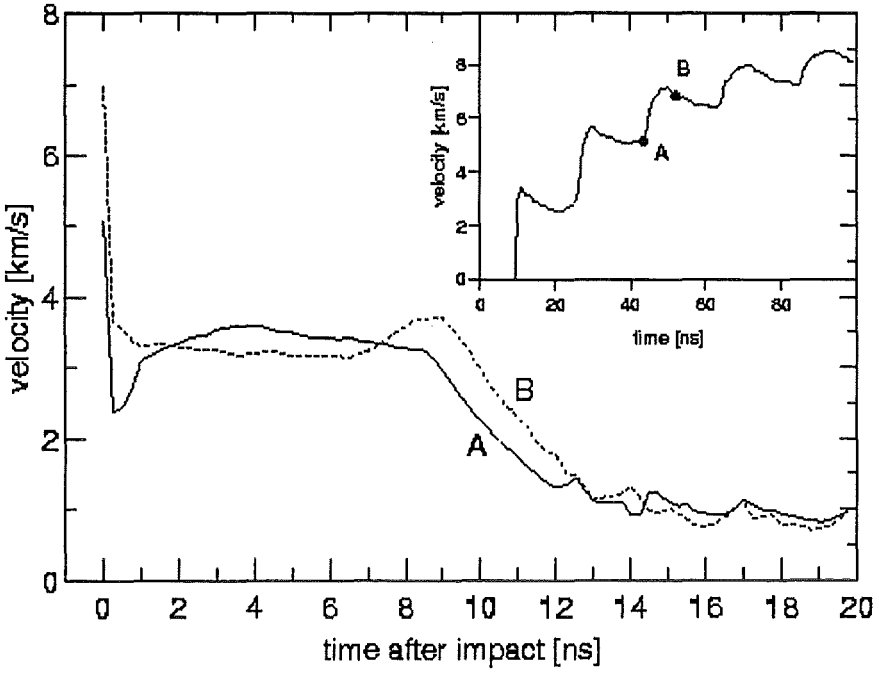

Figure 4.12: Simulated velocity evolution of the LiF-Al interface after the impact at two different phases of the pressure wave (A:ϕ = 0; B: ϕ = π). In the inlet, the moments of impact for the two models are shown within the velocity curve of a free flying target.

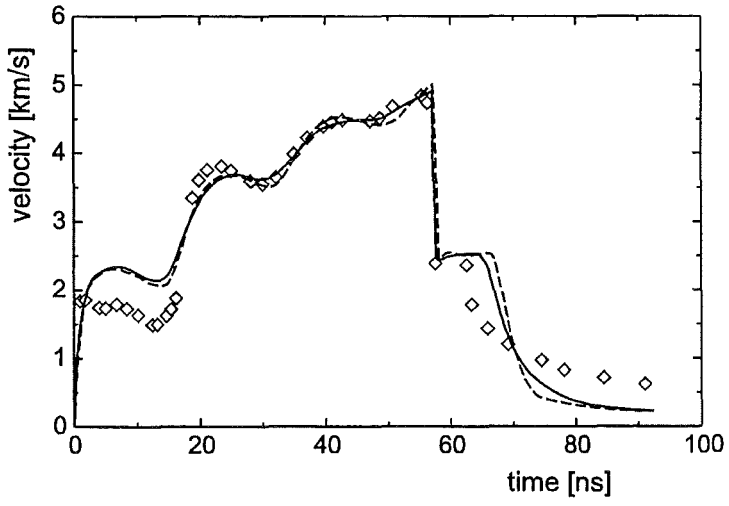

Figure 4.13: Simulated back-surface velocities for an impact of an initially 71 μm Al-flyer on a LiF foil. The impact takes place at t=58 ns. dashed: simulation without thermal conduction and radiation. Transfer straight line: simulation including.

The magnitude of these velocity humps in general depends on the equation of state and on the dissipative mechanism (thermal conduction, radiative transfer) considered in the simulations. Fig. 4.13 presents a comparison of two impact calculations, one without dissipative processes (pure hydrodynamic dashed) and one including dissipative processes (i.e. thermal conduction by electrons and radiative transfer in conduction approximation, straight line). Obviously, transport of energy from the hot plasma to the solid flyer is able to reduce the final thickness of the Al-flyer, which is seen as a shorter velocity plateau after impact as well as a smoothing and shortening of the velocity steps before the impact takes place. Furthermore, the evaporation by additional energy transfer also gives rise to an additional pressure acting on the flyer so that the velocity fail after impact becomes less steep.

4.3 Optimization of the foil launching with ion beam

To reach a high launching velocity, it is important to know the optimal absorber material and ion energy (range of the ions). Changing the kinetic energy of ions at the same power density one can determine the optimal ion energy for a given material.

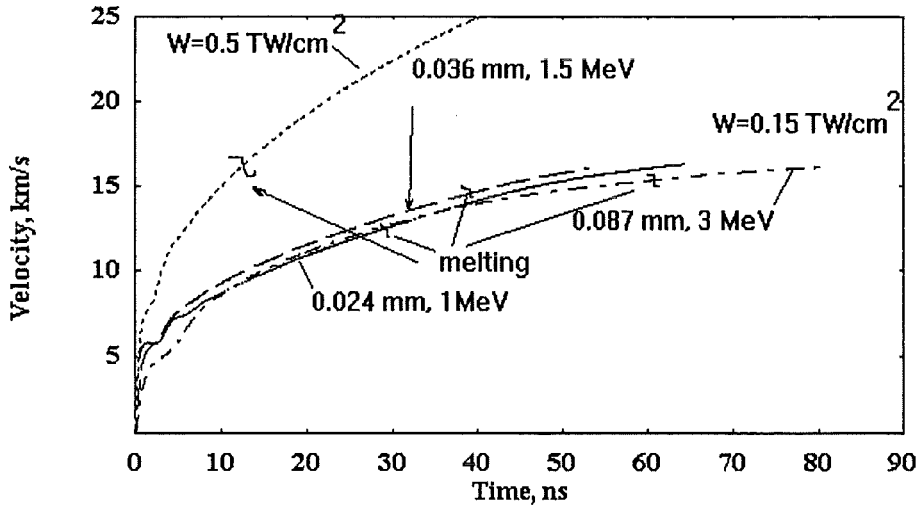

Figure 4.14: Acceleration of aluminum foils at constant power densities (0.1, 0.15, 0.5 TW/cm^2) and different proton energies (1 MeV, 1.5 MeV, 3 MeV). The masses of the solid (accelerated) part are the same (about 10 mm), the thicknesses are 24, 36 and 87 μm correspondingly.

Results for aluminum, the most studied material, which are shown in Fig. 4.14, are in accordance with previous estimations (Vorobiev & Goel 1995). Beams with 1.5 MeV and 1 MeV ions have a higher acceleration efficiency than a 3 MeV beam, because of a better proportion between the absorber and payload masses. Nevertheless, if we account for the melting of material by conduction waves, a 3 MeV beam becomes preferable. Also, the increase of power density from 0.15 to 0.5 TW/cm^2 does not give any advantage because of the high temperatures (both in the first shock and in energy deposition zone) and as a consequence the melting of the solid part of the

foil. The power density of 1 TW/cm^2 is obviously the upper limit for such a launching, because then the pressure in the shock wave is high enough to melt the foil in the release wave. A further enhancement of the foil acceleration is possible only by increasing the beam duration.

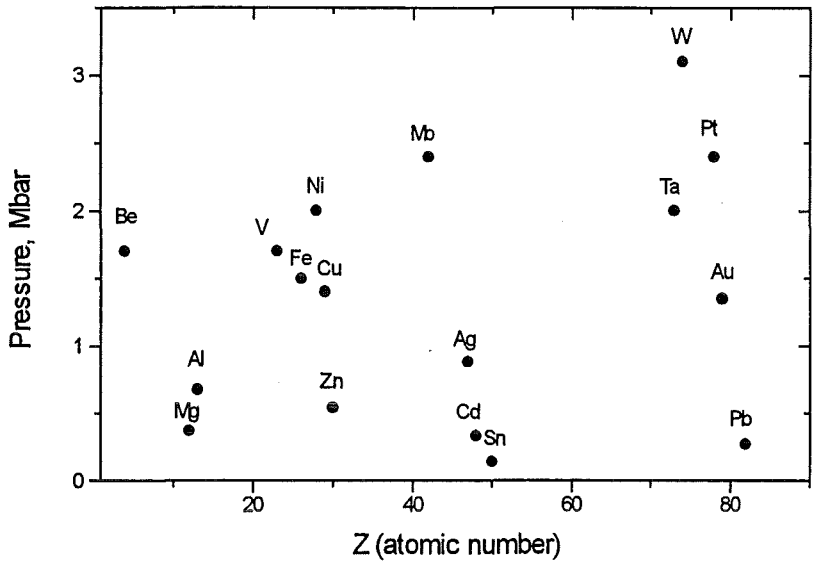

Figure 4.15: Pressure corresponding to the beginning of melting in a release wave against the atomic number.

Another way to overcome this restriction is to use payload material which can withstand higher driving pressures. Figure 4.15 shows the maximum possible driving pressures for different materials. If we assume a constant size of payload (which is thick enough to prevent complete melting in heat conduction waves), the best payload material is characterized by the highest ratio of the maximal driving pressure to its density. According to these criteria we obtain the following list of preference : 1-Be, 2-Al, 3-Mo, 4-Ni. To reach the highest possible velocity at the given beam power density (0.15 TW/cm^2) one should use a Be or Al payload. Potentially Mo and Ni foils as payloads can be preferred at higher beam powers as they will produce higher pressures impacting the target due to a higher shock impedance. This is the case of PBFA-2 protons which have been focused to 5.4 TW/cm^2 and Li to 2.3 TW/cm^2. In the following we study the acceleration of Mo foils with intense ion beams typical for PBFA. The beam energy is deposited in a gold absorber. The thickness of the gold layer is equal to the ion range. In these calculations we use a multiphase EOS (Bushman *et al.* 1992) for metals and the heat conduction approximation for energy transfer. The peak power density is about 1 TW/cm^2. The density, temperature and velocity profiles calculated for a 5 MeV proton beam and for a 10 MeV Li beam are shown in Fig. 4.16-18.

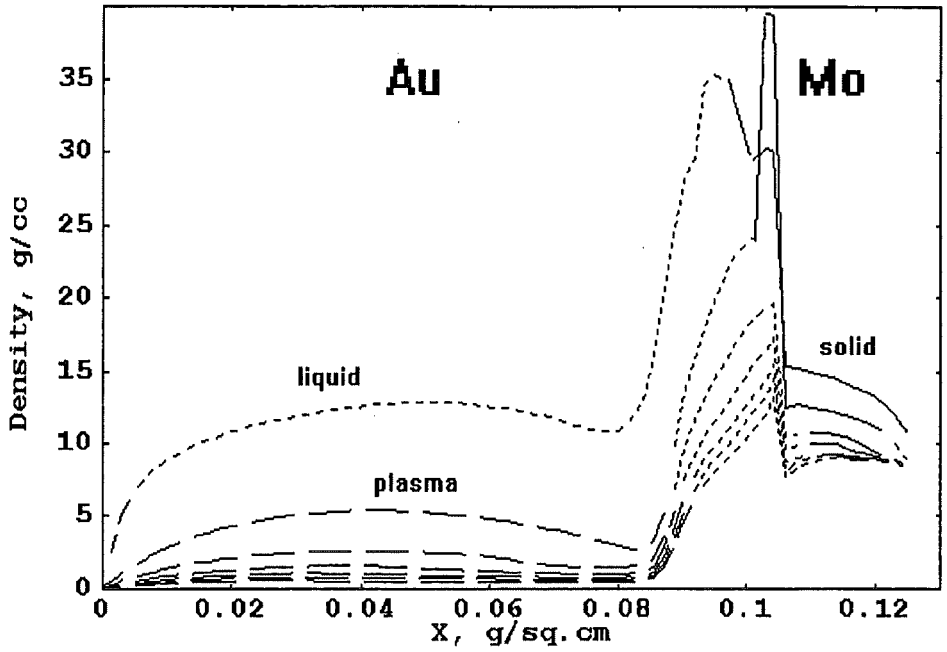

Figure 4.16.a: Density profiles for a composite (54 μm. Au + 20 μm Mo) target irradiated by a PBFA 5 MeV proton beam. The time interval between the curves corresponds to 8 ns. The different matter states are shown with the different line styles: solid state-solid line, liquid state - dotted line, plasma state - dashed line.

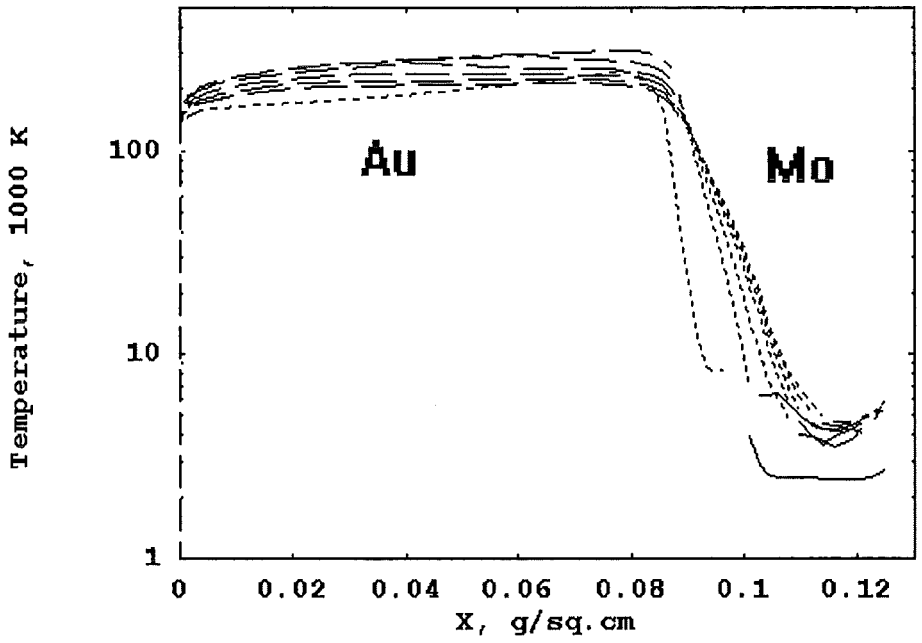

Figure 4.16.b: Temperature profiles for a composite (54 μm Au + 20 μm Mo) target irradiated by a PBFA 5 MeV proton beam. The time interval between the curves corresponds to 8 ns. The different matter states are shown with the different line styles: solid state-solid line, liquid state - dotted line, plasma state - dashed line.

For the 5 MeV proton beam one interesting effect is found: the decrease of the payload thickness from 20 μm to 10 μm leads to smaller driving pressures due to rarefaction waves coming from the free surface. As a result the payload remains in solid state until the heat conduction wave arrives from the energy deposition zone.

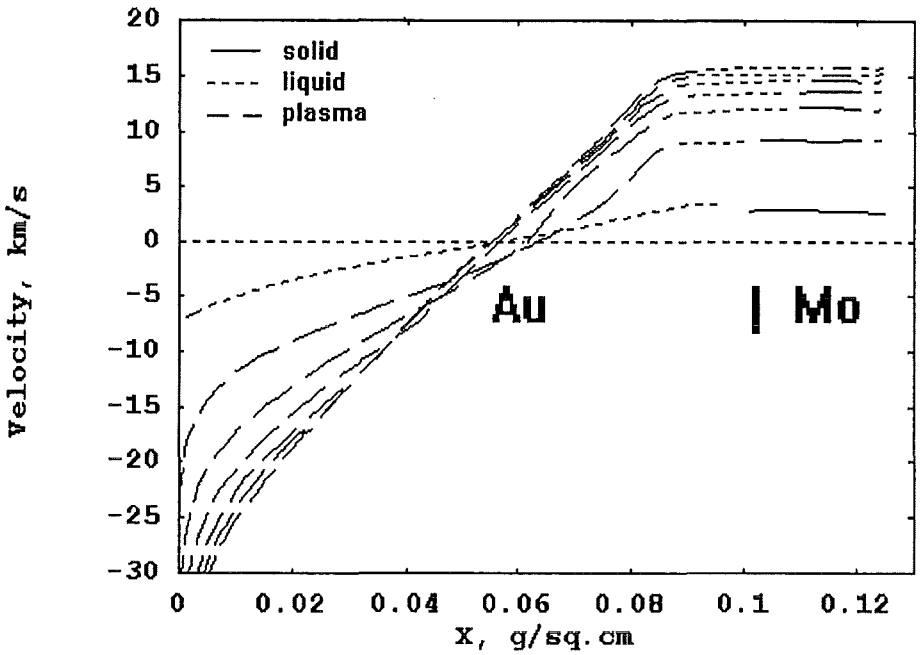

Figure 4.16.c: Velocity profiles for a composite (54 μm Au + 20 μm Mo) target irradiated by a PBFA 5 MeV proton beam. The time interval between the curves correspond to 8 ns.

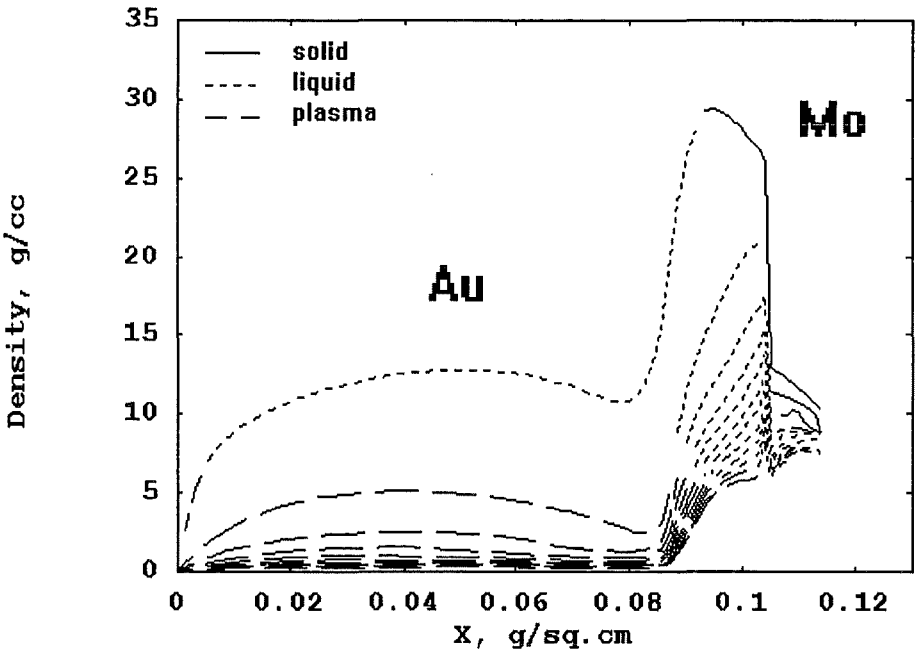

Figure 4.17.a: Density profiles for a composite (54 μm Au + 10 μm Mo) target irradiated by a PBFA 5 MeV proton beam. The time interval between the curves corresponds to 8 ns. The different matter states are shown with the different line styles: solid state-solid line, liquid state - dotted line, plasma state - dashed line.

At the moment when the melting wave reaches the free surface of the target the payload reaches a velocity of 17 km/s. The payload mass in this case is about 4 times higher than that for the case of an aluminum foil considered previously for simulations with the KALIF beam. With high kinetic energy of the ion beam the range becomes large and thick absorbers can be used. The wave transit time through the energy deposition zone can be of the same order as the pulse duration.

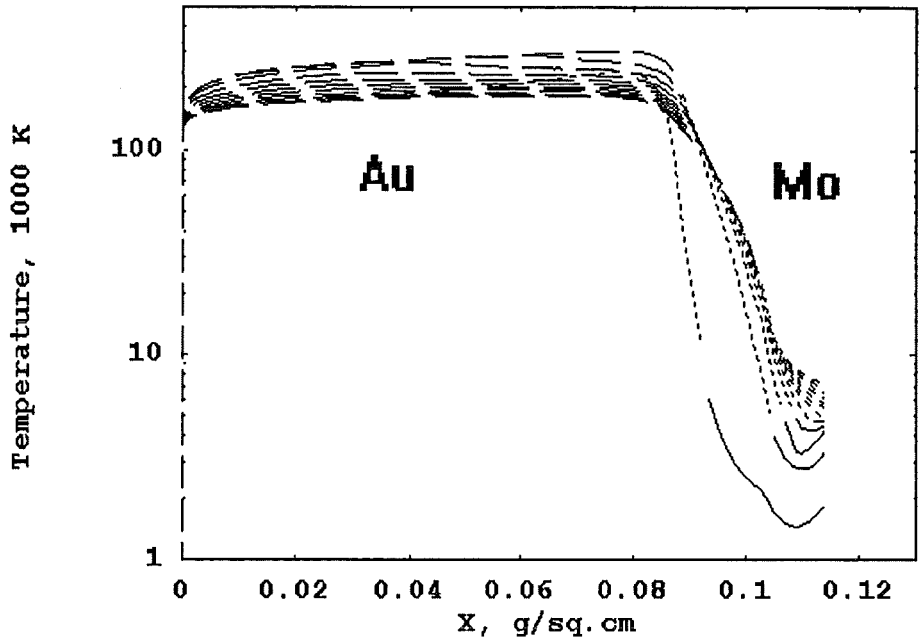

Figure 4.17.b: Temperature profiles for a composite (54 μm. Au + 10 μm Mo) target irradiated by a PBFA 5 MeV proton beam. The time interval between the curves corresponds to 8 ns. The different matter states are shown with the different line styles: solid state-solid line, liquid state - dotted line, plasma state - dashed line.

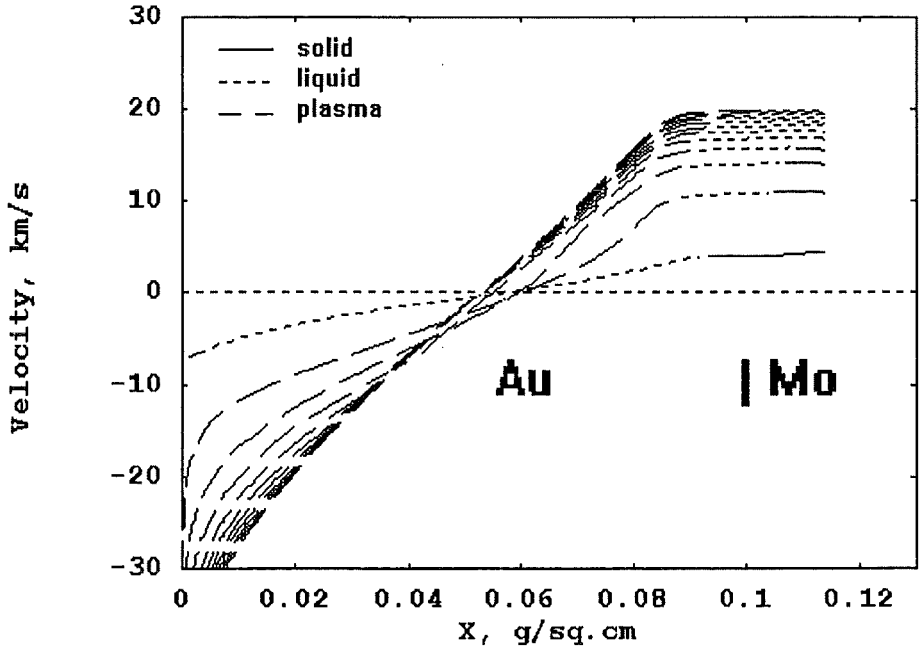

Figure 4.17.c: Velocity profiles for a composite (54 μm. Au + 10 μm Mo) target irradiated by a PBFA 5 MeV proton beam. The time interval between the curves corresponds to 8 ns. The different matter states are shown with the different line styles: solid state-solid line, liquid state - dotted line, plasma state - dashed line.

The pressure profile is significantly nonuniform with a maximum at approximately ¾ M (where M is the absorber size in mass coordinates). The driving pressure at the boundary between the absorber and the payload depends on the thickness of the payload (less the thickness, less the pressure). As a consequence the acceleration of the payload does not depend very much on its thickness.

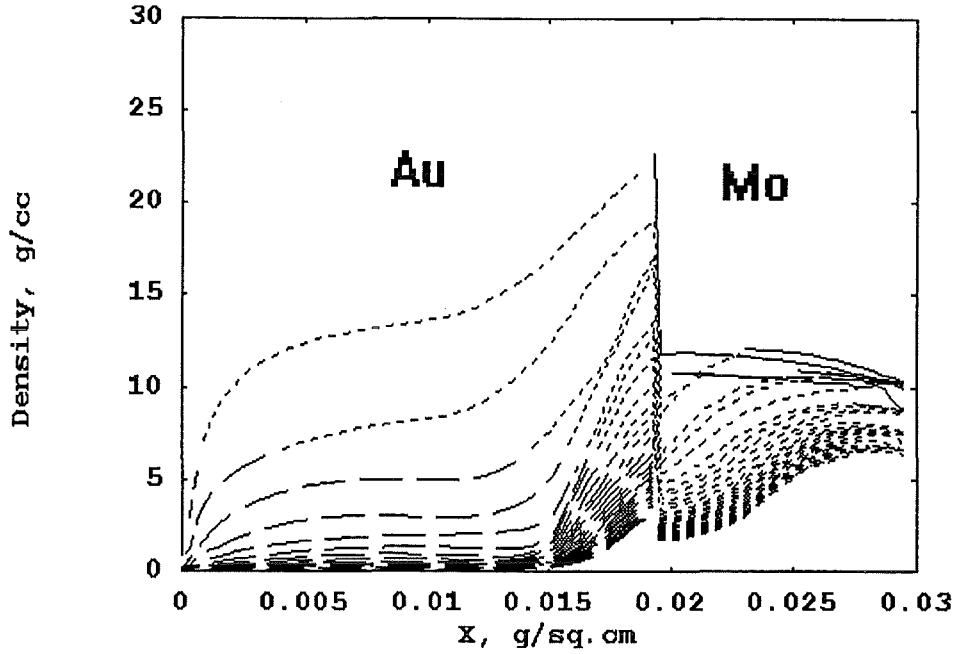

Figure 4.18.a: Density profiles for a composite (10 μm. Au + 10 mμ Mo) target irradiated by a PBFA 10 MeV Li beam. The time interval between the curves corresponds to 2 ns. The different matter states are shown with the different line styles: solid state-solid line, liquid state - dotted line, plasma state - dashed line.

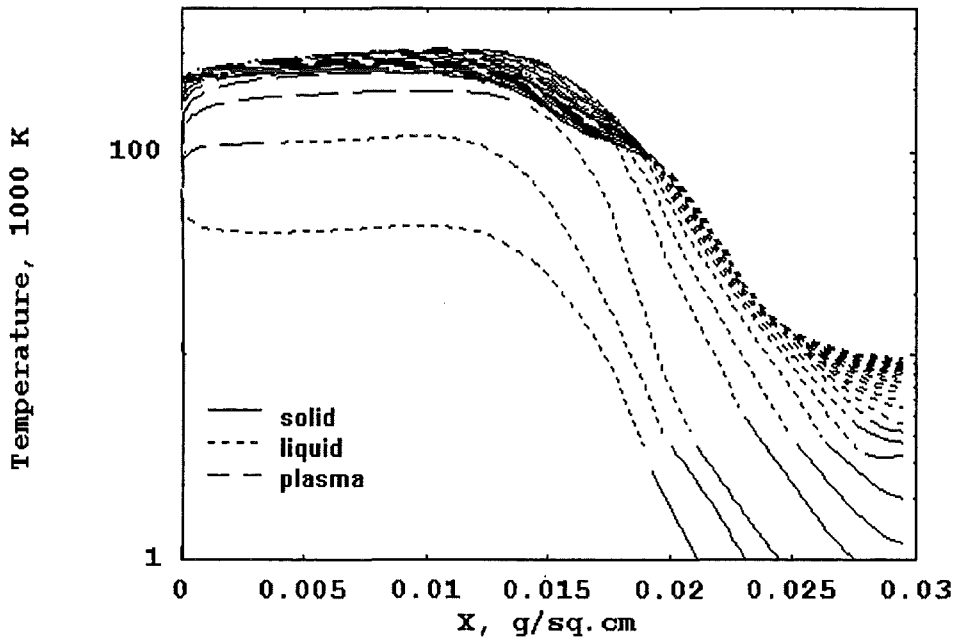

Figure 4.18.b: Temperature profiles for a composite (10 μm. Au + 10 μm Mo) target irradiated by a PBFA 10 MeV Li beam. The time interval between the curves corresponds to 2 ns. The different matter states are shown with the different line styles: solid state-solid line, liquid state - dotted line, plasma state - dashed line.

For thin absorbers (small ranges) the pressure reaches its maximum value very quickly because the energy deposition is compensated by the fast expansion of the material. In this case the value of maximal pressure practically does not depend on the range of the ions and is determined by the power density level and material

properties (e.g. density, Grüneisen coefficient etc.). For the thin absorbers the driving pressure is close to the maximal pressure, so the payload accelerates more effectively, but also the attenuation of the pressure is more rapid.

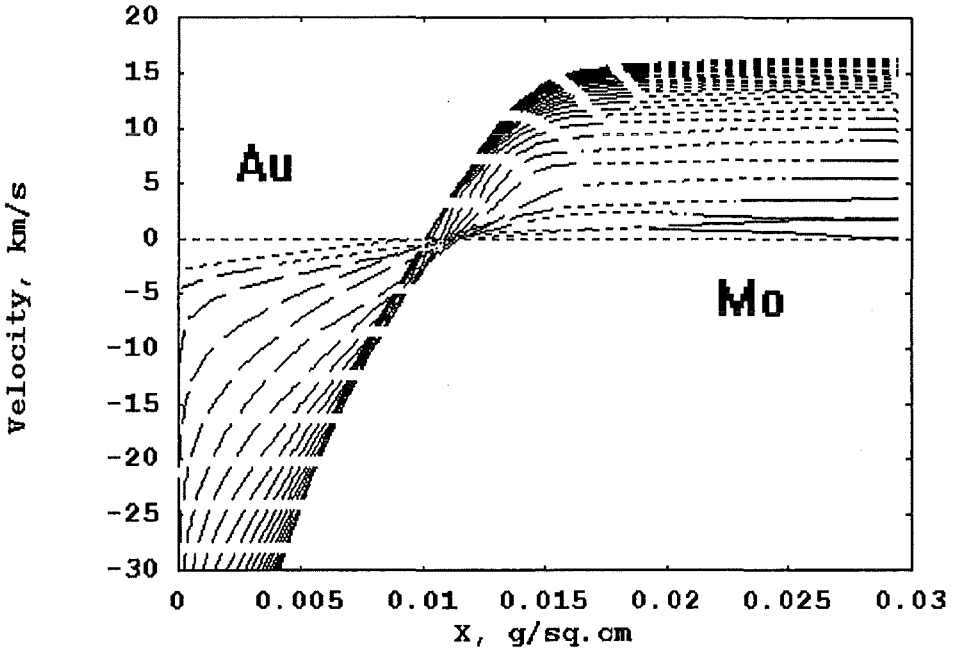

Figure 4.18.c: Velocity profiles for a composite (10 μm. Au + 10 μm Mo) target irradiated by a PBFA 10 MeV Li beam. The time interval between the curves corresponds to 2 ns. The different matter states are shown with the different line styles: solid state-solid line, liquid state - dotted line, plasma state - dashed line.

The results of these calculations lead to the following conclusions:

1) The size of the solid part of the foils should be large enough to prevent melting by heat conduction. That means one should use for the payload a material with high melting temperature and moderate density.

2) To obtain the highest possible acceleration efficiency the absorber mass should be 2-3 times larger than the payload mass.

3) The length of the payload should not be too large, because the first shock wave (which is of a triangular form in this case) will otherwise destroy the payload.

4) Acceleration velocities up to 15 km/s can be reached with aluminum foils using available high power light ion beams with power densities of 0.1-0.5 TW/cm^2. The size of the solid part of the accelerated foils is about 10 μm.

4.4. Empirical equation of state in the plasma region

The plasma generated by the action of the ion beam is mainly in the region of moderate to strong nonideality. The theoretical description of a strongly coupled plasma requires sophisticated tools, and experimental information in this domain is scarce. A successful interpretation of beam-target interaction experiments performed at KALIF can serve as a check of theoretical models involved such as energy deposition and EOS. Computer simulations of beam-target interaction experiments performed at KALIF have been used to get information on these phenomena. The simulation results mainly depend on two factors. Namely on the time dependence of the beam power at the target, and on the EOS of the strongly coupled dense and hot target plasma.

The time evolution of the power density used in the present analysis is that determined using different diagnostic methods (Hoppé *et al.* 1995). The power profile at the position of the target sometimes shows a spike resulting from the time-of-flight correction applied to measured electrical data. An empirical profile (dashed) is displayed in Fig. 4.19.a together with the smoothed profile (average over several shots) used for the simulations (solid). The corresponding proton energy history on target displayed in Fig. 4.19.b also shows the time-of-flight compression effect: 1.3 MeV protons overtake protons started earlier at lower acceleration voltages and reach the target first.

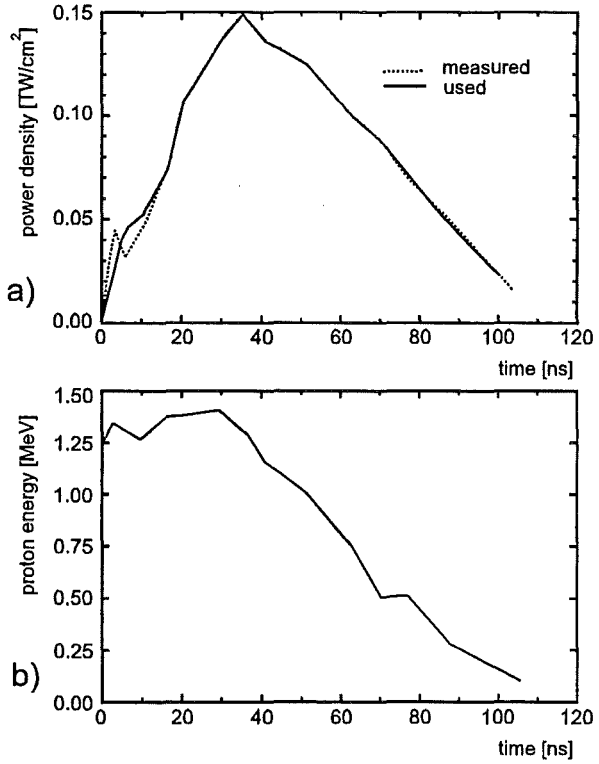

Figure 4.19: Time evolution of proton beam; a) Power density at focus and b) proton energy

The results of calculations using SESAME (1982) and Bushman *et al.* (1992) EOS tables have shown that both EOS give inadequate results for the time interval between 10 and 20 ns, when the density is reduced by an order of magnitude and the temperature increases up to 10 eV. These states of matter correspond to the

region of strongly coupled plasma. Changing power density and beam power evolution within the limits of experimental uncertainties did not improve the situation. We note that the uncertainty in EOS models is large in this region. To rectify this situation we use a semiempirical EOS model which contains several fitting parameters.

For this purpose a semi-empirical EOS in the form of generalized Mie-Grüneisen EOS is developed which describes the experimental data of shock compression of solid samples in the pressure range up to several Mbar. Following the usual procedure, the internal energy of matter is divided into two parts: the cold energy E_c is a function of density only, while the thermal component of the energy E_t is a function both of temperature and density. As our simple EOS model does not contain the temperature we shall use (p,ρ) variables.

$$E(p,\rho) = E_c(\rho) + E_t(p,\rho) \tag{8}$$

For calculations we need functions $p(\rho,E)$ and $c_s(\rho,E)$. To describe Hugoniot data for solid matter we choose for the cold pressure the conventional form (Eliezer *et al.* 1986, Bushman *et al.* 1989):

$$p_c(\rho) = \sum_{i=1}^{5} a_i \delta^{(i/3+1)}, \qquad \delta \geq 1 \tag{9}$$

$$p_c(\rho) = \frac{\rho_0 c_{s0}^2}{n-m}\left(\delta^n - \delta^m\right), \qquad \delta \leq 1 \tag{10}$$

where $\gamma = \rho/\rho_o$ and ρ_0, and c_{s0} are the normal density and sound velocity, respectively. At a given binding energy E_b one of the coefficients in (10), for example M, can be expressed through the other as:

$$M = 1 + \frac{C_{so}^2}{E_b(N-1)} \tag{11}$$

Coefficients a_i are found by solving the system of linear equations that ensure the properties of material under normal conditions and by using the Thomas-Fermi-Dirac model at high compression. The cold component of the total pressure strongly dominates the thermal component in shocked states of solid matter up to several megabars. The thermal pressure is related to the thermal energy through the Grüneisen parameter γ which is represented as a function of energy and density

$$P_t = \gamma(E,p)\, E_t\, \rho \tag{12}$$

The sound velocity can be written as

$$C_s^2 = \left(\frac{\partial p}{\partial \rho}\right)_E + \left(\frac{\partial p}{\partial E}\right)_\rho \left(\frac{\partial E}{\partial p}\right)_s \tag{13}$$

Using the second law of thermodynamics we get

$$C_s^2 = \left(\frac{\partial p}{\partial \rho}\right)_E + \left(\frac{\partial p}{\partial E}\right)_\rho \cdot \frac{p}{\rho^2} \qquad (14)$$

Substituting eq. (12) into eq.(14) we obtain the following formula for sound velocity

$$C_s^2 = C_{cold}^2 + E_t\left(\gamma + \gamma^2 + \left(\frac{\partial \gamma}{\partial \rho}\right)_E + \left(\frac{\partial \gamma}{\partial E}\right)_\rho \frac{p}{\rho}\right), \qquad (15)$$

where $C_{cold} = \left(\frac{\partial P_c}{\partial \rho}\right)$ is the cold component of velocity. We use the following dependence of Güneisen parameter on the internal energy

$$\gamma = \gamma(\rho)_\infty + \frac{\gamma(\rho)_0 - \gamma(\rho)_\infty}{1 + \left(\frac{E}{E_0}\right)^\alpha}, \qquad (16)$$

where E_0 is determined by analysing the shock-wave experiments on porous samples and α is a fitting parameter. According to eq. (16) $\gamma(\rho)_0$ tends to $\gamma(\rho)_\infty$ for hot matter.

To describe asymptotic behaviour of γ in the limit of high compression (Fermi gas) and expansions (ideal gas) we choose both functions γ_0 and γ_∞ to have asymptotic value 2/3 for $\rho \to \infty$ and $\rho \to 0$.

$$\gamma(\rho)_0 = \frac{2}{3} + \left(\gamma_s - \frac{2}{3}\right) \frac{2}{\left(\frac{\rho_0}{\rho} + \frac{\rho}{\rho_o}\right)} \qquad (17)$$

$$\gamma(\rho)_\infty = \frac{2}{3} + \left(\gamma_{\min} - \frac{2}{3}\right)\left(\frac{2}{y + 1/y}\right)^\beta, \quad y = \frac{\rho_0}{\rho}\xi, \qquad (18)$$

where γ_s is the Grüneisen coefficient at normal conditions, ρ_0 is the normal density, γmin is some minimum value of γ in dense of plasma and β and ξ are fitting parameters. Parameter ξ gives the density of plasma where γ_∞ reaches its minimum value.

This density approximately corresponds to the critical point and is about an order of magnitude smaller than the normal density. The parameter β determines the rate of increase of γ from its plasma value to the asymptotic value 2/3 of ideal gas. These parameters together with α are the most important parameters to fit simulation results to the experimental data. Grüneisen parameter as a function of specific energy and density is shown in Fig. 4.20

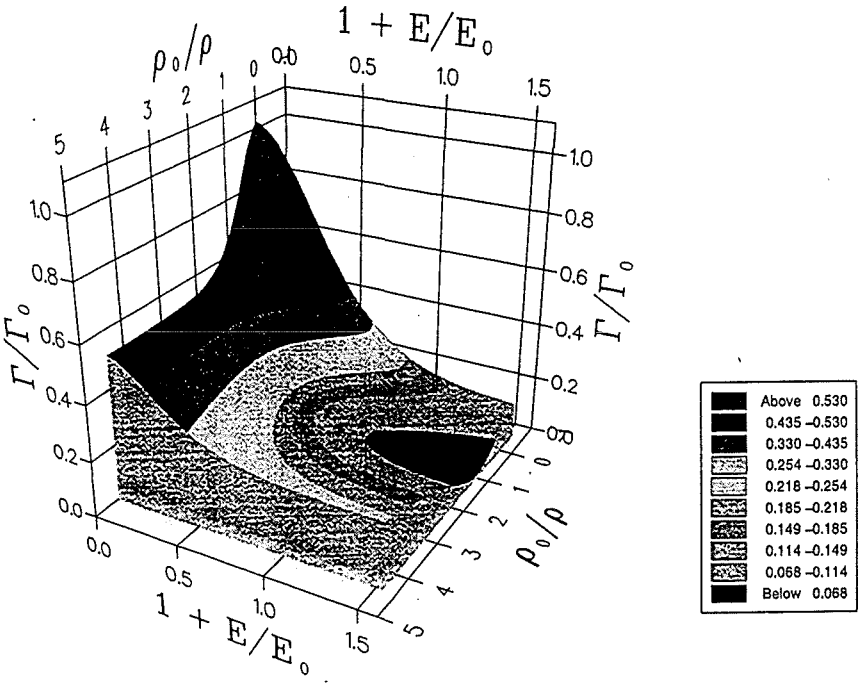

Figure 4.20: Grüneisen parameter as a function of specific energy and density for aluminum.

To describe compression of porous samples the thermal component of pressure in EOS must be correct for densities close to normal density. This simple analytical EOS allows us to describe the available experiments on isentropic expansion of shocked material.

The analytical form of equation of state is convenient for numerical calculations. It saves computational time and assures the continuity of pressure and sound velocity over the entire range of simulation.

Using experimentally measured profiles different experiments have been analysed. In this way we can determine the dependence of $\gamma(\rho,E)$ by matching the coefficients β, α and ξ in formulas (15-16) and by fitting the calculated results to the experiments. Thus determined coefficients as well as the parameters of the cold curve are given in the TABLE 4.1 below.

Table 4.1: Coefficients for EOS

α	β	E_0	γ_{min}	γ_s	ξ	
1.1	0.02	30	0.2	2.1	0.1	
a_1	a_2	a_3	a_4	a_5	N	M
-15009.612	51732.56	-66509.87	37631.99	-7845.07	3.5	1.93633

As it is seen from Fig. 4.20, there exist regions where the Grüneisen parameter decreases with compression (near the minimum and the maximum values). Such behaviour of the Grüneisen parameter may lead to rarefaction shocks and thermodynamic instabilities. To avoid this, restrictions must be imposed on the dependence of Grüneisen coefficient on volume (Segletes 1995). The most strict condition is:

$$\frac{\partial \gamma}{\partial \sigma} \geq -\frac{\gamma}{\sigma} \tag{19}$$

where $\sigma = \rho/\rho_0$. Let us see how this condition is satisfied for the expansion region. Using eqs. 16-18 we can write

$$\frac{\partial \gamma}{\partial \sigma} \geq \frac{\partial \gamma_\infty}{\partial \sigma} \geq \frac{\beta}{\xi}\left(\frac{\partial f}{\partial y}\right)_{\max} (\gamma_{\min} - 2/3),\ 0 \leq y \leq 1 \tag{20}$$

Where

$$f = \frac{2}{y + 1/y}, \tag{21}$$

Then condition (18) can be rewritten as

$$\frac{2\beta}{\xi}(\gamma_{\min} - 2/3) \geq -\frac{\gamma_{\min}}{\xi} \tag{22}$$

or

$$\beta \leq \frac{\gamma_{\min}}{2(2/3 - \gamma_{\min})} \tag{23}$$

It is seen that this condition is satisfied for EOS parameters represented in the TABLE. For compression regime we have the following estimation

$$\frac{\partial \gamma}{\partial \sigma} \geq \left(\frac{\partial f}{\partial y}\right) \min(\gamma_s - 2/3) \leq \frac{\gamma}{\sigma} \tag{24}$$

Condition (18) is rewritten in the form

$$0.25(\gamma_s - 2/3) \leq \frac{\gamma}{\sigma} \tag{25}$$

It can be checked that this condition is valid at least up to compression degrees σ = 3-4 corresponding to 2-3 Mbar pressures in aluminum. Thus we have shown that the EOS developed is thermodynamically stable in the region of our concern.

Results of numerical simulations using the analytical EOS with parameters presented in Table 4.1 are shown in Fig. 4.21 together with the experimental data for foils of different thickness launched by the ion beam. The EOS describes all experiments with aluminum foils of different thickness.

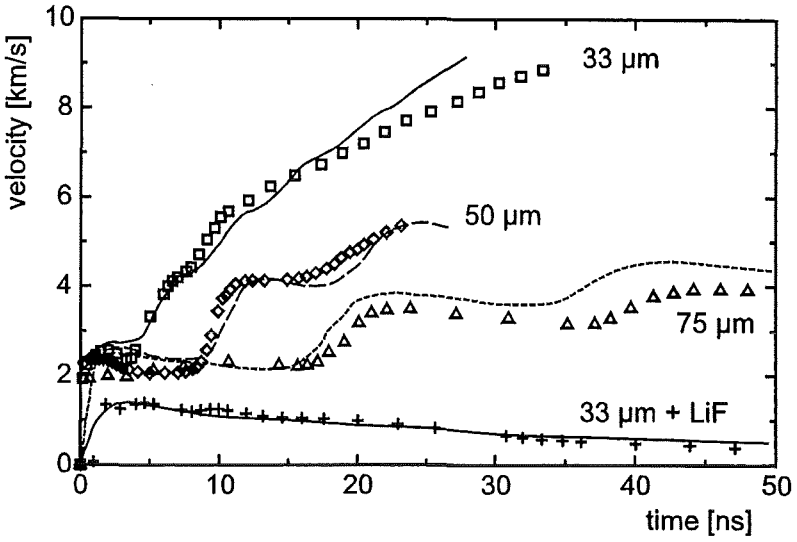

Fig. 4.21: Velocity profiles for aluminum foil of different thickness calculated using the analytical EOS (lines) compared with experimental results (symbols).

4.5 Comparison of simulation results with different EOS models

In this section we show that the state of the accelerated foils is sensitive to the equation of state data and use data based on more profound models. We combine EOS models designed for shock wave modeling describing melting, vaporization and experimental data on compression and unloading of porous matter with those developed for strongly ionized material based on the model of chemical equilibrium. Numerical simulations performed with the measured shape of voltage and power profile (Hoppé *et al.* 1995) showed, that with a reasonable variation of peak power density, between 0.1-0.2 TW/cm^2 we were not able to describe the experiment using the Bushman EOS. The main discrepancy appears when the material is ionized (that corresponds to the time interval between 10-20 ns).

In the present work, to improve the description we have combined the Bushman EOS with the model of chemical equilibrium (Gryaznov *et al.* 1980) using normalized ionization degree as a switching parameter. This approach has been used in (Grabovski *et al.* 1996) to describe the shock wave generation by intense pulses of soft x-rays. In (Gryaznov *et al.* 1980) the chemical Z model (Ebeling *et al.* 1991) of gases has been extended to the region of strongly coupled multicomponent plasma. In a strongly coupled plasma short range forces play an important role. The repulsive forces accounting for the effect of overlapping electrons are taken into account. In addition to the repulsive mechanism bond energies responsible for the existence of condensed states are also introduced into the chemical model. Results of simulations with this unified EOS table are shown in Fig.4.23. It is seen that accurate accounting for ionization and for short range forces allows to describe experiments much better. We compare this unified EOS with the results of analytical model (Goel & Vorobiev 1996) and investigate the region of discrepancies.

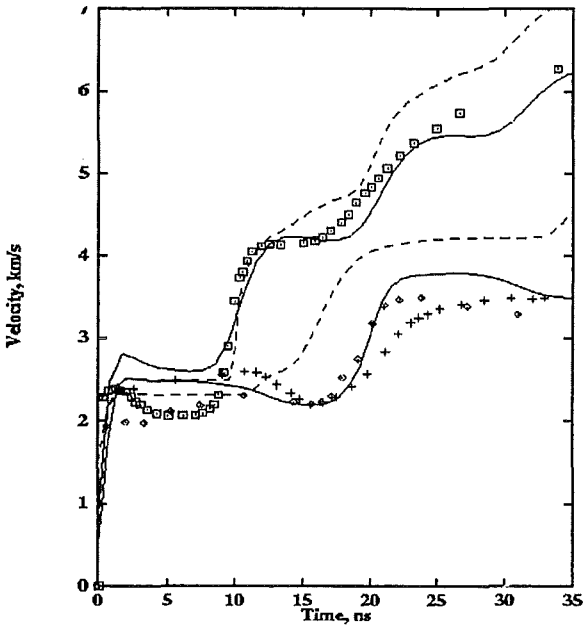

Figure 4.22: Velocity profiles for 75 μm, and 50 μm mm Al foils calculated using the Analytic EOS (solid lines) and SESAME EOS (dashed lines) compared with experimental data (symbols).

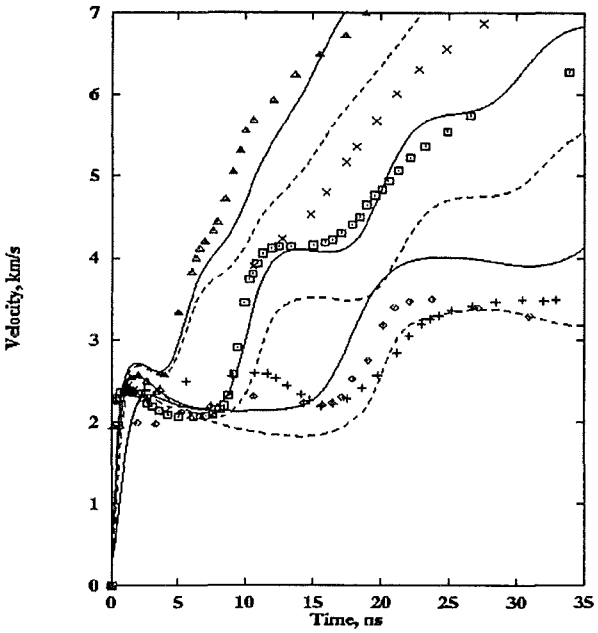

Figure 4.23: Velocity profiles for 0.075, 0.05,0.033 mm Al foils calculated using unified tabulated EOS (solid lines) and the Bushman EOS (dashed lines) compared with experimental data (symbols).

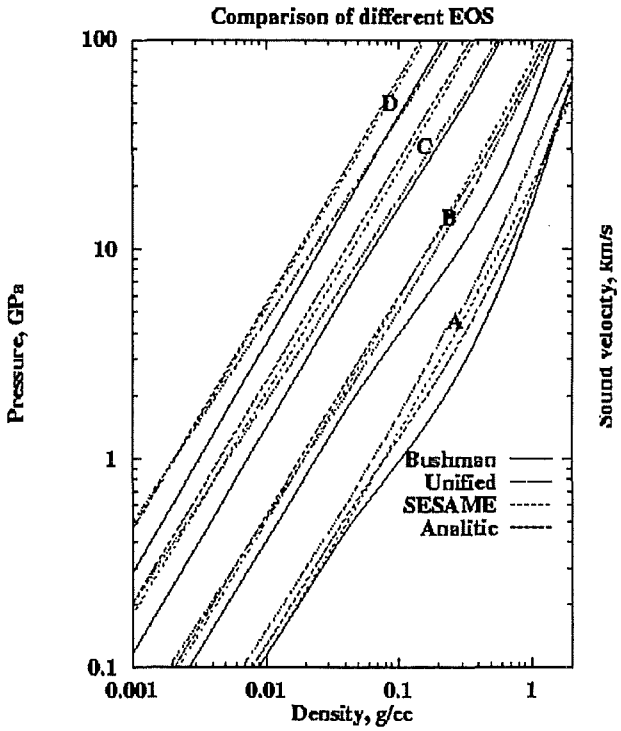

Figure 4.24: Pressure as a function of density at constant internal energy (A-50 kJ/g, B-200 kJ/g, C-800 kJ/g and D-2MJ/g) calculated using different EOS models.

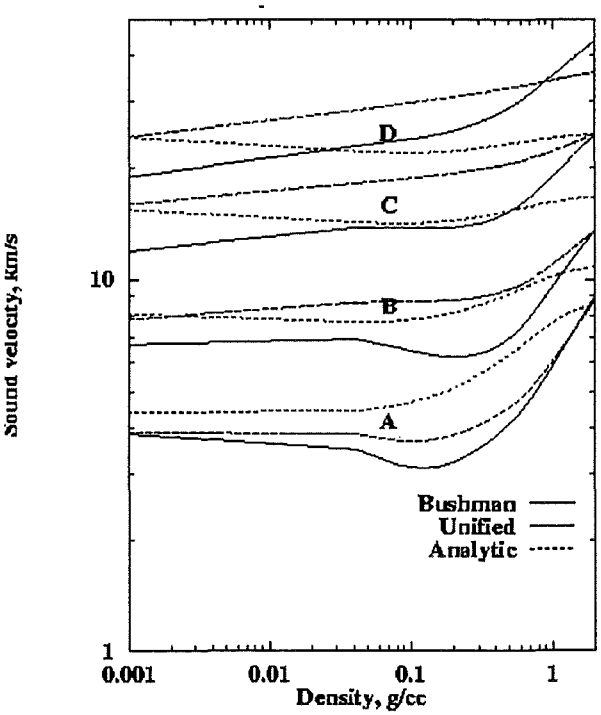

Fig. 4.25: Sound velocity as a function of density at constant internal energy (A-50 kJ/g, B-200 kJ/g, C-800 kJ/g and D-2MJ/g) calculated using different EOS models.

In Figs. 4.22-25 different EOS models used in the simulation are compared. At high energy densities (curve **D** in Fig. 2.23) all EOS except of the Bushman EOS give very close values for pressure in the low density region. Analytic EOS occupies an intermediate place between the Bushman model and the other models. The main reason why the Bushman EOS does not describe the experiment (at 10-20 ns of time interval) seems to be the underestimation of the plasma pressure at moderate energy densities (see curve **B**). This is no surprise as in the original Bushman model partial ionization is not taken into account. The agreement of results calculated with SESAME EOS with experiments is also not satisfactory. The other models, on the contrary, overestimate the pressure at high energy densities. Results of simulation with the Bushman EOS (Fig.4.23) show not only insufficient amplitude of the second velocity step (because the pressure calculated is not high enough) but also a slower increase in the second velocity step. This can be partially explained by underestimation of the sound velocity (see Fig. 4.24 curves **A, B**) calculated with this EOS. Results obtained with corrected (unified) EOS (see Fig. 4.23) describe experiments better also due to higher sound velocity in comparison with original Bushman EOS.

On the basis of the analysis of foil acceleration experiments we have compared different equations of state. We have shown that simulation results strongly depend on the used equation of state. In addition to the analytical equation of state in generalized Mie-Grüneisen form (Goel & Vorobiev 1996) that describes experiments well, we have also generated a tabulated unified EOS. This tabulation combines the advantage of condensed matter equation of state, that describes the shock wave experimental data, with chemical equilibrium model accounting for interparticle interactions in strongly coupled dense plasma. The main difference in the analytical equation of state that describes experiments well and other equations of state is in the region of temperatures 5-10 eV and densities 1.-0.1 g/cm^3 The implication of this deviation on the parameters of the chemical model is to be investigated.

5. Summary and Conclusions

In this report we have summarised shock wave physics experiments performed so far with the Light Ion Facility KALIF and their theoretical analysis. We have shown that many useful information can be extracted from these experiments in the state of matter that is, otherwise not accessible in the laboratory. These are, e.g. the equation of state of matter in the region of strongly coupled plasma, spall strength measurement at strain rates of the order of 10^7 - 10^8/s and across grain boundaries, and the shock melting threshold of metals. Some of the experimental techniques and theoretical tools developed for this purpose are unique in their nature.

In chapter one we have shown the regions of phase diagram accessible to investigations at KALIF. Though this diagram has been presented for aluminum, qualitatively it is valid for all other materials as well. The zone directly heated by the beam - energy deposition zone - receives about 5 MJ/g of energy in a few 10's of ns. This causes a strong shock wave to travel into the adjacent material. By suitably designing the target and the diagnostic method velocities up to 12.5 km/s of flyer plates could be recorded with the ORVIS system. The ORVIS laser-Doppler-velocimeter was set-up to measure velocities with a temporal resolution of 200 ps. Later, this velocimeter was extended to a 1-dimensional line imaging VISAR. The acceleration of the flyer plate is not monotonic and shows several steps caused by the shock wave reverberation inside the flyer. To understand these jumps an analytical theory based on acoustic approximation was developed. To avoid reverberations the aluminum foil was glued to a LiF-crystal which has approximately the same Hugoniot as aluminum. Thus ablation pressure could be directly measured inside the target. A detailed numerical analysis of these processes with specially developed hydrodynamic codes has shown that important equation of state information can be extracted from these experiments. Parameters of a newly developed Mie-Grüneisen type of equation of state have been determined and presented in this report (Table 4.1). Analysis of colliding foil experiments provides information on the importance of thermal conduction and radiation transport in plasma and in flyer.

Spall strength for single crystal and polycrystalline samples of some materials was measured at high strain rates. It was found that linear extrapolation of spall strength measured at low strain rates is not valid at strain rates in excess of 10^6/s. The curve gets twisted towards higher strengths. Spall strength of single crystals exceeds that of polycrystals by a factor of 2 to 3. Precise measurement of shock melting of some materials was performed. Results are presented in Table 2.1

Most of the numerical analysis has been performed with 1 dimensional hydrodynamic code. Some verifying 2 dimensional calculations have revealed that 2 dimensional effects are of minor importance in present experiments and 1 dimensional calculations are adequate for most applications at KALIF. The 2d calculations have, however, shown that in experiments with the 1d line imaging VISAR, the radial distribution of back surface velocities replicates the spatial profile power density profile of the KALIF beam. Since the beam profile is normally measured in a separate experiment and assumed to be the same in all other experiments the VISAR measurement can be used as an additional tool for beam diagnostics.

The numerical simulation results depend on the theoretical and numerical models used and on the beam parameters. The numerical scheme used in one dimensional calculations is well tested and gives stable results. Test calculations with 2 dimensional codes have proved that the problems treated here can be well simulated with 1d codes. The most important physical models involved are the beam energy deposition model and the equation of state for the material. The former process has been studied for some time and we find our model for energy deposition to be adequate to calculate the energy coupling of protons in cold matter and plasma. This is also confirmed by measuring the wave reverberation time in the experiments described earlier as well as by doing experiments in which target thickness was reduced to subrange level. Equation of state in the region of strongly coupled plasma is not well known. We have developed an equation of state for aluminum, the material on which most experiments were performed, that reproduce KALIF experiments as well as shock wave data on cold matter. The influence of radiation transport and conductivity, though of minor importance for most of the study presented in this report, is somewhat uncertain and is presently under investigation.

The accuracy of simulation results, of course, depends on the beam parameters that are fed into the codes as input. The irregular nature of pulse power technology and the fact that due to the small space available in the diode and target does not allow an on-line diagnostic of required input parameters concurrent with the shock wave experiments, accounts for the uncertainties in the beam parameters. The spatial beam profile, which is a flat top Gaussian does not play a role in 1D simulations. The temporal evolution of beam power and proton energy used for the numerical analysis of shock wave experiments is an average over a number of shots especially dedicated to this purpose. The peak power for the so called B_θ-diode, with which most experiments were performed, is 0.15 ± 0.05 TW/cm^2. This gives an indication in the uncertainty in the results. Our simulation results with variation of input parameters suggest that the uncertainty in the beam parameter may be somewhat less.

We have to continue our effort to reduce the uncertainty in the obtained results. In shock wave experiments the pressure in the dense and hot ablation plasma adjacent to the flyer plate is given by the rear surface velocity of the target. A K_α-satellite spectroscopy of the ablation plasma, on which work is in progress, will give information on its temperature. Thus two important quantities necessary for equation of state can be measured. Further if the ablation plasma can be imaged on a steak camera one can get some information on the density of ablating plasma.

On the theoretical side we should continue our efforts to quantify the dissipation effects like thermal conductivity and radiation transport. The latter process requires beside a good numerical algorithm also the knowledge of opacity coefficients in plasma region down to the solid material. These coefficients specially in low temperature range are not well known. We have to find out the sensitivity of the results to this lack of knowledge. We need further to improve our 2D codes to include dissipative effects, apart from the numerical problems this also puts large demands on computer memory and time.

Acknowledgment:

The authors are indebted to Academician Prof. Dr. Vladimir E. Fortov, director of the High Energy Density Research Center Moscow, and to Prof. Dr. Günther Keßler, Director of the Institut für Neutronenphysik und Reaktortechnik for their engagement in launching and supporting our cooperation, and for their continuous interest in our work.

Our collaboration was supported by the Bilateral Scientific-Technical Cooperation Agreement grants WTZ X222.61 and RUS-545-97, by INTAS grant 94-3189, and by the NATO Science Programme linkage grant LG 930 326.

The experimentalists would like to thank R. Bohrmann, L. Buth, R. Huber and especially O. Stoltz for their technical support, and K. Leber and Th. Petri for operating KALIF.

6. References

ADDESSIO F.L. *et al.* 1986, Los Alamos National Laboratory Report No.LA-10613-MS

ALME H.A., RHOADES C.E. 1995, A computational study of projectile melt in impact with typical whipple shields, *Int. J. Impact Engng.***17**,1

ALTSHULER, L.V. *et al. 1981 J. Appl. Math. Tech. Phys. (USSR)* ***2****, 3.*

ANDRIOT P., CHAPRON P., LAMBERT V., OLIVE F. 1984, Influence of Melting on Shocked Free Surface Behavior Using Doppler Laser Interferometry and X-Ray Densitometry. In *Shock Waves in Condensed Matter - 1983*, Eds.: Asay J.R., Graham B.A., Straub G.K.. Elsevier Science Publishers B.V. pp.277-280

ASAY J.R., MIX L.P., PERRY F.C. 1976, Ejection of Material from Shocked Surface. *Appl. Phys. Lett.* **29**, pp. 284-287.

BACHMANN, H. *et al.* 1988. In *Proc. 7th Int. Conf. on High-Power Particle Beams - Karlsruhe 1988,* Vol. I, 827.

BAKANOVA, A.A. *et al.* 1983, Prikladnaja Matematika i Technicheskaja Phisika (in Russian) **2**,76

BARKER L.M. & HOLLENBACH R.E. 1972, *J. Appl. Phys.* **43**, 4669.

BAUMUNG, K. *et al.* 1992, In *Proc. 9th International Conference on High-Power Particle Beams*, Washington DC, Vol. I.,68.

BAUMUNG, K. *et al.* 1993, Light-ion Beam-Target Interaction Experiments on KALIF, Nuovo Cimento **106** A 1771.

BAUMUNG, K. *et al.* 1994 *J. Appl. Phys.* **75**, 7633.

BAUMUNG, K. *et al.* 1995a, In *Report FZKA 5590,* Forschungszentrum Karlsruhe, p. 88.

BAUMUNG, K. *et al.* 1995b *Int. J. Impact Engng* **17**, 38(1995).

BAUMUNG K, *et al.* 1996, *Laser and Particle Beams,* **14**, pp.181-209.

BELYAKOV, L.V. *et al.*1966, On Melting of Lead in Shock Wave. *Academy of Sciences of USSR - Doklady* **170**, p. 540.

BLOOMQUIST, D.D. & SHEFFIELD S.A. 1983, *J. Appl. Phys.* **54**, 1717.

BLUHM, H. *et al.* 1985, In *5th IEEE Pulsed Power Conf.*, Arlington, Virginia, 114.

BLUHM, H. *et al.* 1988, In *Proc. 7th Int. Conf. on High-Power Particle Beams - Karlsruhe 1988*, Vol. I, 516.

BLUHM, H. *et al.* 1992a, In *Proc. 9th Int. Conf. on High-Power Particle Beams - Washington 1992,* Vol. I, 51.

BLUHM, H. *et al.* 1992b, In Proc. of the IEEE, **80**, 995.

BLUHM, H. *et al.* 1994, In *Proc. 10th Int. Conf. on High-Power Particle Beams* - San Diego, CA, Vol. I, 77.

BUSHMAN, A.V., FORTOV, V.E., LOMONOSOV, I.V. 1989, Proc. Enrico Fermi School 1989, Elsevier Pub. p. 249.

BUSHMAN, A.V. *et al.* 1992, *Intense Dynamic Loading of Condensed Matter.* (Taylor & Francis, Washington DC, London)

CHAPRON P., ELIAS P., and LAURENT B. 1988, Experimental Determination of the Pressure Inducing Melting in Release for Shock-Loaded Metallic Samples. In *Shock Waves in Condensed Matter - 1987*, Eds.: Schmidt S.C., and Holmes N.C., Elsevier Science Publishers B.V. pp. 171-173.

CURRAN, D. R. *et al.* 1987 *Phys. Reports,* **147**, 253.

DAVISON, L. & GRAHAM R.A. 1979 *Phys. Reports,* **55**, 255.
EBELING, W. *et al.* 1991,*Thermophysical Properties of Hot Dense Plasmas*, Teubner-Texte zur Physik, Bd. 25, (Teubner, Stuttgart-Leipzig) .
ELIEZER, S *et al.* 1986, *An introduction to equation of state* (Cambridge University Press, Cambridge).
ELIEZER, S., GILATH, I. 1990 *J. Appl. Phys.* **67** , 715.
FORTOV V.E., GOEL B., MUNZ C.-D., NI A.L., SHUTOV A.V., VOROBIEV O.YU., 1996, *Nucl. Engng.* **123**,169-189.
GLUSHAK, B.L. et al. 1989 JETP **96**, 1301.
GODUNOV, S.K 1976, Numerical solution of multidimensional problems of gas dynamics, (in Russian) Nauka, Moscow
GODUNOV, S.K. 1959 *Mat. Sbornik* **47**, 271.
GOEL, B., BLUHM, H. 1988 *J. de Physique* **49**, C7-169.
GOEL, B., 1990,. In *Proc. 8th Int. Conf. on High-Power Particle Beams - Novosibirsk* VOL.2, p.715.
GOEL, B., VORIBIEV, O.YU., NI, A.L. 1992, Generation of Ultra High Pressure with Light Ion Beams, Proc. Ninth International conference on High-Power Particle Beams, (ed. Mosher D., Cooperstein G.), May 25-30,1992, Washington DC, USA , Vol. II. p.957.
GOEL B., VOROBIEV O.YU. 1996, Equation of State Information from Beam-Target Interaction Experiments at KALIF, vol.14 Laser and Particle Beams, p. 637
GRABOVSKI, E.V., SMIRNOV V.P. *et al.* 1996, JETP **82** (3).
GRAY III, G.T. 1990 *Shock Compression of Condensed Matter - 1989*, (Elsevier. Sc. Pub. B.V.) 407.
GRYAZNOV, V.K, *et al.* 1980, Thermophysical Properties of Working Media of Gas Phase Nuclear Reactor (Atomizdat, Moscow, 1980) in Russian.
HEMSING, W.F. *et al.* 1990, In *Ultrahigh- and High-Speed Photography, Videography, Photonics, and Velocimetry,* Proc. SPIE **1346**, 133.
HENIS, Z., and ELIEZER, S. 1993, Melting Phenomenon in Laser-Induced Shock Waves. *Phys. Rev.* **E48**, 2094.
HOPPÉ, P. *et al.* 1995 In *Report FZKA 5590,* Forschungszentrum Karlsruhe, 51.
KANEL, G.I., *et al* 1993, Spall Strength of Molybdenum Single Crystals, *J. Appl. Phys.* **74**, pp. 7162-7165.
KANEL, G.I. *et al.* 1994a, In *High-Pressure Science and Technology*, AIP Press Conf. Proc. **309**, Woodburry, NY, Part 2, 1043.
KANEL G.I. *et al.* 1994b, Spallation near the Ultimate Strength of Solids. In *High-Pressure Science and Technology - 1993*, Eds.: Schmidt S.C., Shaner J.W., SAMARA, G.A., and Ross, M. AIP Press, NY, 1123-1126.
KANEL, G.I., UTKIN, A.V. 1996a, Estimation of the Spall Fracture Kinetics from the Free-Surface Velocity Profiles. In *Shock Compression of Condensed Matter - 1995*, Eds.: SCHMIDT S.C. and TAO W.C., AIP Conf. Proceedings **370**, pp. 487-490.
KANEL, G.I., RAZOREVOV, S.V., and UTKIN, A.V. 1996b, Spallation in Solids Under Shock-Wave Loading: Analysis of Dynamic Flow, Methodology of Measurements, and Constitutive Factors. In *High Pressure Shock Compression of Solids - II. Dynamic Fracture and Fragmentation.* Springer Verlag, eds.: Davison L., Shahinpoor M., and Grady D., Springer Verlag, 1-24.
KANEL, G.I. *et al.* 1996c Spall Fracture Properties of Aluminum and Magnesium at High Temperatures. *J. Appl. Phys.* **79**, pp. 8310-8317.

KAROW, H.U. *et al. 1990,* In *Proc. 8th Int. Conf. on High-Power Particle Beams - Novosibirsk,* Vol.1, p. 445.
KESSLER, G. *et al.* 1994 In *High-Pressure Science and Technology*, AIP Press Conf. Proc. **309**, Woodburry, NY,1887.
KING, P.J, COTGROVE, D.F., SLATE P.M.B. 1968. Infra-Red Method of Estimating the Residual Temperature of Shocked Metal Plates. In *Behavior of Dense Media under High Dynamic Pressure*, BERGER J., ed., Gordon and Breech, 513-520.
KISELEV, A.N. AND FALKOV, A.A. 1982 *Fiz. Goreniya i Vzryva (USSR)*, **18**, 105.
KOLGAN, V.P 1972 , *Scientific Notes of CAGI* (in Russian) **3**, 68.
KOPTCHENOV ,V.I.,KRAIKO A.V 1983, *Zh. Vych.Matem.i Matem Fiz.* (in Russian) **23**, 848.
KORMER, S.B. *et al.* 1962, JETP 42, 686.
KUTSAR, A.R. *et al.* 1973, *Acad. of Sciences USSR - Doklady (USSR)*, **213**, 81.
KUTSAR, A.R. *et al.* 1982, *Letters to ZETF,* **35**(3), 91.
LAQUA H. *et al.*1995. *J. Appl. Phys.* **77**, 5545.
LION M.S. 1993, An Extended Lagrangian Method, AIAA, p.92.
MAC FARLANE, J.J., WANG, P., 1988, Fusion Power Associate Report, Michigan.
MARSH, S.P. 1980 *LASL shock Hugoniot data* (Univ. of California Press, Berkeley) p.441.
MAZHUKIN, V, SMUROV, I., FLAMANT G. 1994 *Journ. Comp. Phys.* 112.
MCQUEEN, R.G. and MARSH, S.P. 1960. Equation of State for Nineteen Metallic Elements from Shock-Wave Measurements to Two Megabars. *J. Appl. Phys.* **31**, 1253-1269.
MCQUEEN, R.G. *et al.* 1970, The Equation of State of Solids from Shock Wave Studies, Chapter VII In *High-Velocity Impact Phenomena,* Kinslow R., ed., Academic Press, 293-417, (see also Appendix C, D, E, pp. 518-520, 521-529, 530-568).
MEYERS, M.A. 1979 *Met. Trans.* **10A**, 1723.
NEMAT-NASSER, S *et al.* 1992 *Shock Compression of Condensed Matter- 1991*, (North Holland, Amsterdam) 181.
NG, A. and PIRIZ A.R. 1989 *Phys. Rev.*, **A40**, 114.
PIRIZ, A.R. 1988 Plasma Phys. Contr. Fusion, 30, 793.
POLYSHCHUK, A.YA. *et al.* 1991 *Sov. J. Plasma Phys.* **17**, 523.
PRONINA, L.N. and ARISTOVA, I.M. 1990 *High Temp.-High Press.* **22**, 9.
RAIKES S.A. AND AHRENS T.J. 1979. Post-Shock Temperatures in Minerals.
RAZORENOV, S.V. *et al.* 1990 *Acad. of Sciences USSR, Doklady ,* **315**(3),609 (in Russian).
RAZORENOV S.V. *et al.* 1995, Response of high-purity titanium to high-pressure impulsive loading. *High Pressure Research* **13**, pp. 367-376.
SCHIMASSEK, W. *et al.* 1991, *Rev. Sci. Instr.* **62**, 168.
SEGLETES, S.B. 1995 The Effect of Thermodynamic Constraints Upon the Mie-Gruneisen Equations of State, Computational Mechanics'95
SESAME Library, Lawrence Livermore National Laboratory, Report UCID-118574-82-2 (1982).
SIKKA, S.K. *et al.* 1982, *Prog. Mater. Sci.* **27**, 245.

TAYLOR, J.W. 1963 Residual temperature in shocked copper, *J. Appl. Phys.* **34**, pp. 2727-2731.
TSAKIRIS, G.D., and EIDMANN, K. 1987, *JQSRT* **38**, 353.

VAN LEER, B. 1978 *J. Compt. Phys.* **32**, 101.

VON HOLLEW. C. and TRIMBLE J.J. 1976,Temperature Measurement of Shocked Copper Plates and Shaped Charge Jets by Two-Color IR Radiometry, *J. Appl. Phys.* **47,** 2391-2394.

VOROBIEV O.YU., GOEL B. 1995a, *Proc. 10th Int. Conf. on High Power Particle Beams*, BEAM's 94, vol.II, 825—828.

VOROBIEV O.YU., LOMOV, I.N., SHUTOV, A.V., KONDAUROV, V.I., NI, A.L., and FORTOV, V.E. 1995b , *Int. J. Impact Engng.* **17**, 891-902.

VOROBIEV, O.YU., FORTOV, V.E., GOEL, B. 1996, Numerical simulation of shock wave generation with KALIF, *in Proc. of 20th ISSW Conference*, Pasadena 1995, USA.

WERDIGER, M. *et al.* 1996 Asymptotic Measurements of Free Surface Instabilities in Laser-Induced Shock Waves, *Laser Part. Beams* **14**, pp.133-147.

ZELDOVICH, YA.B., RAIZER, Yu.P. 1967 *Physics of Shock Waves*, Academic Press.

ZIEGLER, J.F., ed.1980, *Handbook of Range Distributions for Energetic Ions in all Elements*, Pergamon Press, Vol. **6** of *The Stopping and Ranges of Ions in Matter.*